August 2014

Mineralogy and Geochemistry of Pleistocene Volcanics at Embagai Caldera and Natron Basin, Tanzania: Potential Constraints on the Stratigraphy of Olduvai Gorge

Steven Michael Greenwood
University of Wisconsin-Milwaukee

Recommended Citation

Greenwood, Steven Michael, "Mineralogy and Geochemistry of Pleistocene Volcanics at Embagai Caldera and Natron Basin, Tanzania: Potential Constraints on the Stratigraphy of Olduvai Gorge" (2014). *Theses and Dissertations*. 497.
https://dc.uwm.edu/etd/497

MINERALOGY AND GEOCHEMISTRY OF PLEISTOCENE VOLCANICS AT EMBAGAI CALDERA AND NATRON BASIN, TANZANIA: POTENTIAL CONSTRAINTS ON THE STRATIGRAPHY OF OLDUVAI GORGE

by

Steven M. Greenwood

A Thesis Submitted in
Partial Fulfillment of the
Requirements for the Degree of

Master of Science
in Geosciences

at
The University of Wisconsin-Milwaukee
August 2014

ABSTRACT

MINERALOGY AND GEOCHEMISTRY OF PLEISTOCENE VOLCANICS AT EMBAGAI CALDERA AND NATRON BASIN, TANZANIA: POTENTIAL CONSTRAINTS ON THE STRATIGRAPHY OF OLDUVAI GORGE

by

Steven Greenwood

The University of Wisconsin-Milwaukee, 2014
Under the Supervision of Professor Lindsay J. McHenry

Olduvai Gorge is a paleoanthropologically significant site on the shoulder of the East African Rift Valley of north-central Tanzania, hosting Pleistocene-aged hominid fossils and stone tools. Several volcanoes in the adjacent Ngorongoro Volcanic Highlands (NVH) have erupted volcanic material into Olduvai and other nearby sedimentary basins.

Embagai (Elanairobi) is a Pleistocene caldera within the NVH. It is a potential source volcano for Olduvai tuffs, particularly for Bed II and younger deposits, as it is consistent in overall composition (nephelinite and trachybasalt) and general age. Nephelinitic and phonolitic lava and tuff samples were collected from the caldera floor and the western, eastern, and northeastern sides of the caldera. Common primary minerals included nepheline, clinopyroxenes, titanomagnetite, and andradite garnets exclusive to alkaline volcanic settings. Secondary alteration significantly affected the quality of the geochemical and mineralogical results, with analcime, phillipsite, and calcite as the dominant secondary minerals. Unaffected samples plot as nephelinites. The compositions of phenocrysts of augite, feldspar, and titanomagnetite sampled from both Embagai and the Olduvai beds were compared. High-Mg augite compositions from the northern rim and western flank of Embagai are most similar to those of Olduvai Bed II. Feldspars are rare and distinctively K-rich in Embagai samples, which are dominated by nepheline compared to Olduvai tuffs. Overall, the mineral compositions and assemblage of Embagai appear to be a better match for a younger Olduvai Bed III tuff.

The Pleistocene Peninj Group, exposed to the north of the NVH along the western margin of Lake Natron, is also paleoanthropologically important. It is comprised of the Humbu and Moinik Formations, which contain clastic sediments along with tephras and lavas likely associated with local eruptions from nearby volcanoes. The Main Tuff within the Humbu Formation is interlaid with the Wa Mbugu Basalt to the south of Peninj. This study compares the geochemistry and paleomagnetism of both well-constrained and unknown samples of the Wa Mbugu and other basaltic lavas in the vicinity to constrain the various units in this highly faulted and fragmented region. Samples were variably altered, with zeolites dominating the alteration assemblage. Geochemical results indicate that bulk major and minor elements alone are not enough to distinguish between some lavas of different stratigraphic positions but similar compositions, and would require further study using trace elements, phenocryst compositions, or other means. An oriented sample of the Wa Mbugu appears to indicate transitional polarity as opposed to the normal polarity commonly found with this unit. A second oriented lava sample had reversed polarity, however is not compositionally similar to the nearby Hajaro lava (reversed). This second lava may represent a previously undocumented flow.

With further study of both Embagai and the Natron basin lavas focusing on phenocryst mineralogy in unaltered samples, additional correlations could lead to a higher resolution inter-basin stratigraphic framework for the NVH and for the surrounding paleontologically and archaeologically important sedimentary basins.

TABLE OF CONTENTS

LIST OF FIGURES

Figure Descriptions Page

LIST OF TABLES

LIST OF ABBREVIATIONS

Abbreviation	Description
AF	Alternating field, for demagnetization
BPT	Birdprint Tuff
BTS	Brown Tuffaceous Siltstone
EPMA	Electron Probe Micro-analysis, or electron microprobe
ICDD	International Center for Diffraction Data
LOI	Loss on ignition
MAD	Maximum angular deviation
NVH	Ngorongoro Volcanic Highlands, also known as the Crater Highlands
PPL	Plane-polarized light
TAS	Total Alkali-Silica, a diagram by Le Bas et al. (1986) for igneous rock classification
T_C	Curie temperature
XPL	Cross-polarized light
XRD	X-Ray Diffraction
XRF	X-Ray Fluorescence

ACKNOWLEDGMENTS

Firstly I would like to thank my thesis committee advisors Dr. Lindsay J. McHenry, Dr. Barry I. Cameron, and Dr. Julie Bowles for their tremendous assistance and role as mentors during my time at the University of Wisconsin-Milwaukee (UWM) as a Masters candidate.

I am appreciative of visiting scholar Dr. Anatoly Zaitsev for his assistance with interpretation of silica-undersaturated mineralogy, UWM professor Dr. Tom Hooyer for access to the UWM Geosciences Kappabridge, and Dr. Tristan Kloss for additional lab methods. In addition, Ph.D. candidate Teri Gerard, Masters candidate George "Kit" Carson, Kiel Finn, Gabrielle Walters, and Michael J. Defenbaugh were all instrumental in the process of creating this thesis, either through lab assistance, recommendations or techniques.

I thank all remaining staff, faculty, and students at the Department of Geosciences, University of Wisconsin-Milwaukee for their knowledge, assistance, and support over the last few years.

I wish to thank John Fournelle at the Department of Geoscience, University of Wisconsin-Madison for allowing us access to and offering troubleshooting assistance on the Cameca SX51 electron microprobe.

I am grateful to The Geological Society of America (GSA) and the Wisconsin Geological Society (WGS) for their research funding that allowed for travel to Tanzania in August 2012.

Much appreciation is given to the Tanzania Department of Antiquities and the Tanzania Commission for Science and Technology (COSTECH) for granting research permits, and to the Ngorongoro Conservation Area Authority for the allowance of sample collecting at Embagai and adjacent areas in the Ngorongoro Volcanic Highlands (NVH).

Thanks are given to both the Olduvai Geochronology and Archaeology Project (OGAP) and Olduvai Landscape Paleoanthropology Project (OLAPP) for allowing us to work seamlessly along them at Leakey Camp in Olduvai Gorge, Tanzania.

I thank all hired help and staff at Leakey Camp for keeping us all fed and free of stray scorpions. Special thanks is given to Richard who can pilot a Land Rover over just about anything and to our Maasai scouts Ndengere, Leina, and Paulo who helped us safely navigate the trails of Embagai and surrounding mountains.

I finally thank my family for their love and support, particularly my father Dan who has long been supportive of my efforts in the field of geology, my friends for making sure I stayed on top of my projects and achieved my goals, and my colleagues for inspiring me to reach for even higher goals.

1. INTRODUCTION

The East African Rift Valley (Gregory Rift) has long been studied for both its geological and paleoanthropological importance (e.g. Reck, 1914a). Potential ancestors of modern humans resided in Northern Tanzania (~3°S) during a time of extensive volcanic eruptions originating from the rift-related Ngorongoro Volcanic Highlands (NVH), also known as the Crater Highlands (**Figure 1**). Many of these eruptions have deposited ash and lavas into adjacent sedimentary basins, including Olduvai Gorge, Natron (preserved at Peninj), Laetoli, and Manyara (Hay, 1976; Dawson, 2008). As these locations have been exquisitely preserved and subsequently exposed by rift-related erosion, tectonics, and volcanism, several of these basins have been key to unveiling and understanding hominid evolution in Sub-Saharan Africa (e.g. Klein, 1999). The older volcanoes of the NVH have been well characterized and compared both compositionally and temporally to sites of paleontological and paleoanthropological interest including Laetoli and Olduvai (Mollel, 2002, 2007; Mollel et al., 2008, 2009, 2011; McHenry et al., 2008).

Olduvai Gorge preserves a record of tephra covering much of the last 2 million years of NVH activity, including rhyolites and trachytes from adjacent Ngorongoro and Olmoti volcanoes in Bed I, through Bed II nephelinites and recent carbonatites. Bed II and III tephra tend to be less continuous, exhibit higher levels of contamination, and are often finer grained than those of Bed I, and are thus more difficult to correlate and date. These tephra are consistent with a more distant nephelinitic source. The documented presence of nephelinites at Embagai, Loolmalasin, and Olsirwa volcanoes in the NVH

(Hay, 1976; Mollel, 2007; Dawson, 2008) make these potential volcanic sources for the Olduvai Bed II and younger tuffs.

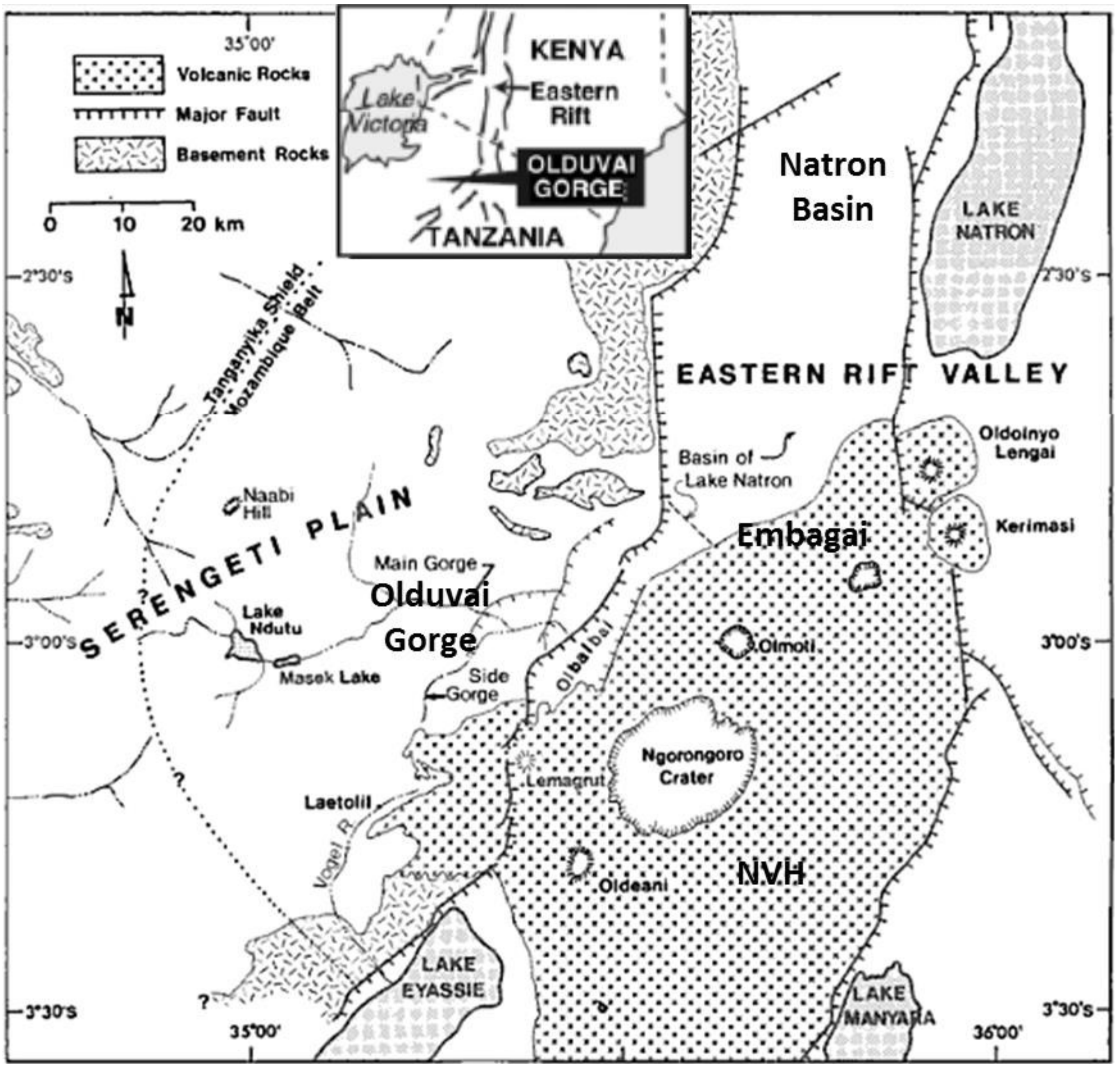

Figure 1. Map of region surrounding Olduvai Gorge. Olduvai tephra likely originated from the Ngorongoro Volcanic Highlands (NVH) to the east. The region sits at southern end of larger Gregory Rift (Eastern Rift Valley). Map after Hay (1976) and McHenry (2012a). Embagai sits within the NVH between Olmoti and Kerimasi volcanoes. The Natron basin lies to the north of the NVH. See Figure 2 for detail of Olduvai Gorge.

This work characterizes the mineralogy and geochemistry of the less studied younger volcanic center Embagai (Elanairobi). It is located between the volcanoes of Olmoti (dated to ~1.8 Ma: McHenry et al., 2008) and Kerimasi (not dated radiometrically but bracketed between 1.1 and 0.4 Ma based on its relation to episodes of faulting: Hay, 1976). Prior studies of Embagai (e.g. Manega, 1993; Mollel, 2007) have not provided the level of mineralogical or geochronological detail needed to test whether it is a likely source for Olduvai Bed II or younger tuffs; better characterization of its mineralogy and geochemistry is necessary to test this.

The Natron basin in far northern Tanzania is stratigraphically complex due to extensive faulting and weathering, particularly in the Type Section (Maritanane) of the Pleistocene Peninj Group (Luque et al., 2009). Fossiliferous sediments at Peninj accumulated in and around an ancient lake that was surrounded by a broad shallow basin (Isaac, 1967). Extensive faulting and alteration has led to some confusion when attempting to identify conformable geologic units, but several thick lavas can act as markers throughout this assortment of tephras and sediments. If correctly identified and dated, these basalts can help constrain the stratigraphy of these anthropologically and paleontologically important beds (Leakey and Leakey, 1964; McHenry et al., 2011).

Of particular interest is the Main Tuff within the Humbu Formation, which contains the Wa Mbugu (Wambugu) basalt to the south of Peninj. The Humbu Main Tuff is a major marker bed within the Humbu Formation and is notable for the discovery of an australopithecine mandible below its base (Leakey and Leakey, 1964). This mandible can be tied to the Acheulian stone industry, characterized by a series of hand axes or 'bifaces' found in the Humbu Formation above the Wa Mbugu. The industry in Northern Tanzania is bracketed by the dates of both the Wa Mbugu basalt and the Intra-Moinik basalt above, within the Moinik Formation (Isaac and Curtis, 1974). The Intra-Moinik was dated by Isaac and Curtis (1974) at 1.33 and 1.38 Ma and was measured as having reversed polarity (Thouveny and Taieb, 1986). The Wa Mbugu basalt has been dated from as early as 1.91 Ma to as late as 0.96 Ma, with a conservative median at 1.5 Ma (Luque et. al., 2009), and has a documented normal paleomagnetic polarity previously attributed to the Olduvai N1 (Thouveny and Taieb, 1986), Jaramillo (Isaac and Curtis, 1974) or Cobb Mountain (Deino et al., 2006) normal polarity events. This wide range of potential ages makes it difficult to ascertain the age of the mandible, which could be the youngest example of *Paranthropus boisei* if the younger dates are accepted.

This project complements ongoing research on the overall volcanic history of the NVH. This characterization helps to reconstruct a more complete volcanic history of the highlands and the paleontologically-rich basins (Olduvai, Natron, and Manyara) that surround them. Correlations between source volcanoes and tephra deposits and better constraints on the ages of these tuffs can help to construct a regional tephrostratigraphic framework.

1.1 Objectives

The objectives of this research project include:

1. Characterize the mineralogy and geochemistry of Embagai caldera.

2. Determine if Embagai is a likely source for Olduvai Bed II or younger tuffs. To test this, I acquired geochemical and mineralogical data for tuffs and lavas from Embagai and compared phenocrysts (e.g. pyroxenes, feldspars) from Embagai with those from Olduvai Bed II and III tuffs. Based on phenocryst compositions and bulk geochemical data, I will assess whether Embagai is a likely source volcano for these units, or whether a different source is required.

3. Characterize the geochemistry of various basaltic lavas from the Natron basin to help correlate units in this highly faulted area. Elemental data from basalt samples of known origin (Wa Mbugu, Hajaro, and Sambu) are used to identify geochemical signatures for each, and are then compared to western Natron basin basalts of less certain origin. I will address whether the Wa Mbugu Basalt can be distinguished from other basalts in the western Natron basin.

4. Obtain paleomagnetic data from the Wa Mbugu Basalt and similar lavas. This new data is compared to previously published data for the region.

1.2 Significance of project

A better understanding of the petrology and geochemistry of Embagai can help reconstruct the evolution of the rift-related volcanism in the NVH, which is important for the interpretation of this unique volcanic system in East Africa. Identifying and characterizing lavas of differing compositions from multiple locations on a volcano can help establish the volcano's eruptive history.

Correlating volcanoes in the NVH with tephra at Olduvai can help reconstruct the eruptive history and magmatic evolution of these NVH volcanic centers. In addition, correlating between individual volcanoes and Olduvai tuffs could allow radiometric dates from the source to be applied to the distal and more altered and contaminated tuffs. Confirming the position of major lava units in the Natron basin also helps constrain the overall stratigraphy of the region, and helps refine the ages of these paleoanthropologically important beds.

2. GEOLOGIC BACKGROUND

2.1 Olduvai Gorge

The beds of Olduvai Gorge have been of great interest in the last century due to their paleontological, anthropological, and archaeological content (e.g. Reck, 1914a, 1914b). Mary Leakey's 1959 discovery of the famous "*Zinjanthropus*" skull, now attributed to *Paranthropus boisei,* made Olduvai world renowned in paleoanthropology, expanding our knowledge of early hominins and promoting the study of additional sites throughout east Africa (e.g. Klein, 2009).

Olduvai is a ~20 km wide Pleistocene basin on the western margin of the East African Rift that has been incised by a gorge (**Figure 2**). The Olduvai river flows eastward from the Serengeti Plain and empties into the Olbalbal depression. The gorge has two primary branches, the Main Gorge which originates from Lakes Ndutu and Masek to the west, and the Side Gorge which meets up with the Main Gorge at the "Junction." There is an ~100 m vertically exposed section of sediments and tephra within the gorge, with the igneous material likely originating from the adjacent Ngorongoro Volcanic Highlands (NVH) by either pyroclastic, fluvial, eolian, or mass movement processes. Remnants of an expanding and contracting Pleistocene saline paleolake (paleolake Olduvai) are seen throughout Beds I and II (Hay, 1976; Hay and Kyser, 2001; Ashley et al., 2010).

The stratigraphic record of Olduvai consists of a series of numbered and named beds, from oldest to youngest: Beds I-IV, Masek, Ndutu, and Naisuisiu (Hay, 1976; **Figure 3**), with the base of the sedimentary record dated to around 2.0 Ma (Naabi Ignimbrite, Deino, 2012). Hay (1976) provides an extensive sedimentological description of the beds. He subdivided the Olduvai succession and identified marker tuffs that allow for correlation between and relative dating of archaeological sites, and worked to determine the paleoenvironments of hominid activities. Bed I tuffs are widespread and have distinct mineralogical characteristics (Hay, 1976; McHenry, 2005, 2012a; McHenry et al., 2008, 2013). Olmoti volcano is the most likely source for most upper Bed I trachytic marker tuffs, based on age, texture, mineral assemblage, and mineral composition, and Ngorongoro caldera is a likely source for the lower Bed I rhyolites (McHenry et al., 2008).

For Bed II, the stratigraphic framework is more difficult to constrain because of the lack of continuous marker tuffs and changes in thickness and lithology in these units. Bed II is the most laterally variable of the Olduvai Beds (Hay, 1976). Bed II is particularly important archaeologically as it records the cultural change from the Oldowan to the Acheulean stone tool technology (Hay, 1976; de la Torre et al., 2012). It is important paleontologically as it records a transition between humid-adapted and arid-adapted taxa, along with the disappearance of *Homo habilis* and the appearance of *Homo erectus* (Leakey and Hay, 1982). It is important to know how and when these lithic cultures developed and thrived, and how they relate to the appearance of certain hominid species (de la Torre et al., 2012). However, Bed II tuffs are notoriously difficult to characterize, correlate, and date (McHenry et al., 2007; McHenry, 2012b), and their volcanic source is uncertain. Bed II will thus be the primary focus for this portion of the project. Bed III will also be briefly investigated as its marker tuffs are thought to fall within the age range of the study volcano, though it has not been studied as thoroughly as Beds I and II.

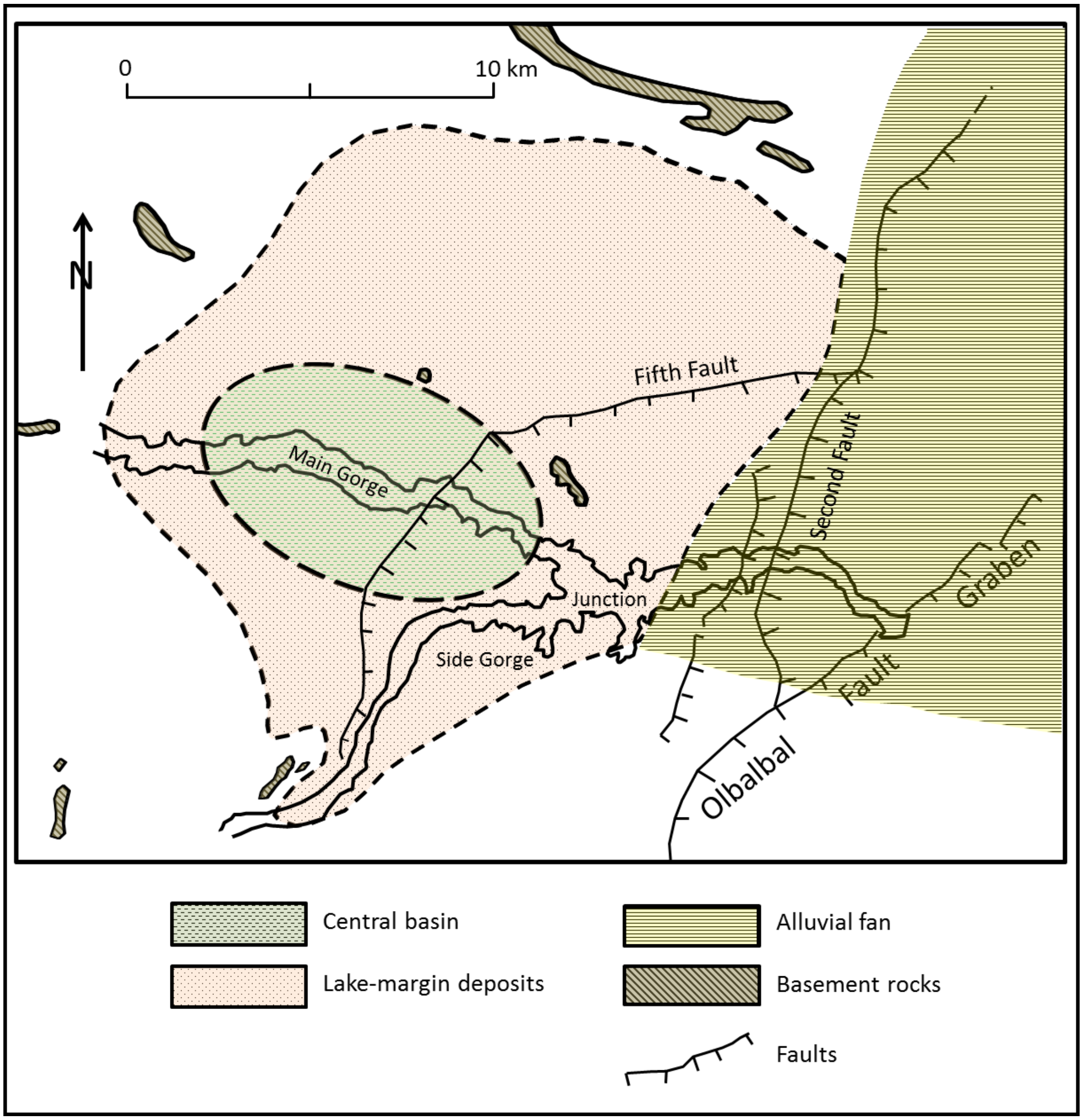

Figure 2. Map of Olduvai Gorge with inferred paleogeography. Modified after Hay and Kyser, 2001. Main branch of gorge, side gorge, and junction labeled. The NVH is located to west of the gorge.

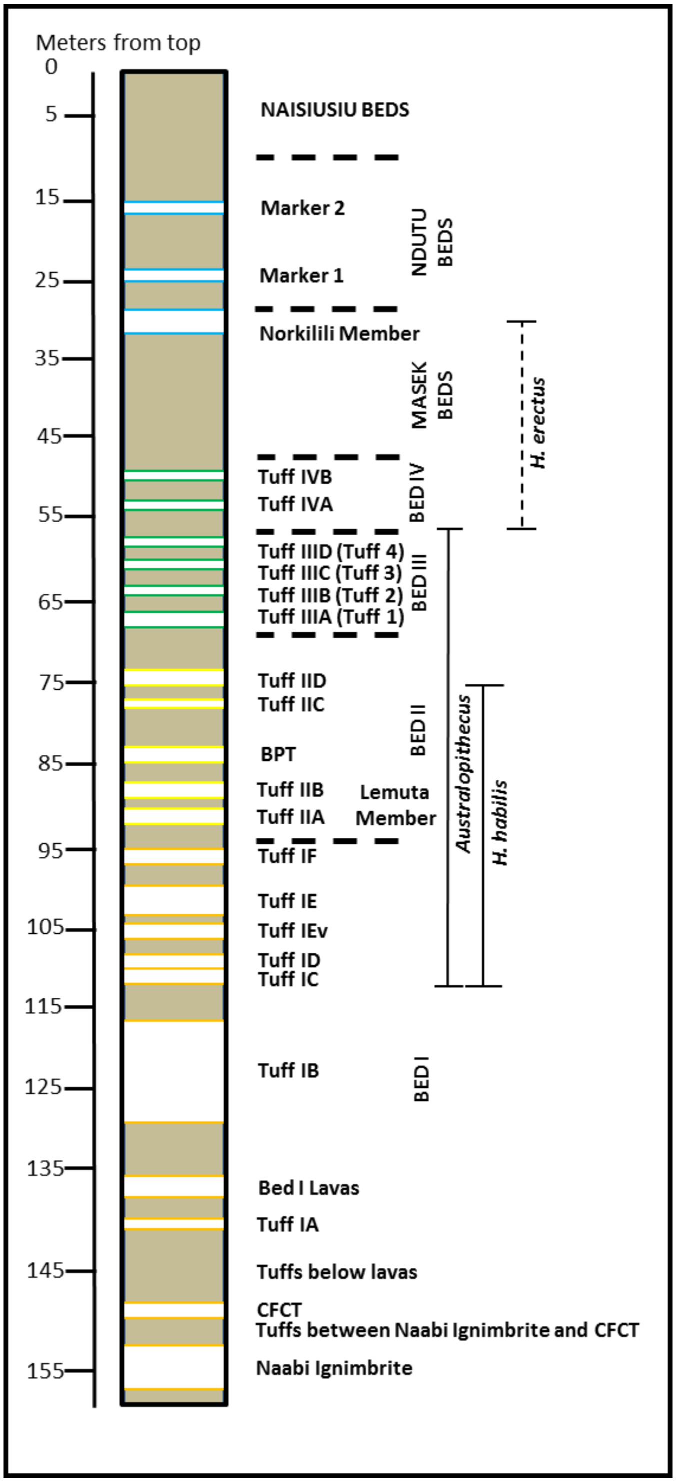

Figure 3. Composite stratigraphic section of Olduvai Gorge with tuffs and major units identified. Beds denoted by color (Bed I: orange, Bed II: yellow, Beds III and IV: green, Masek, Ndutu, and Naisiusiu Beds: blue). Modified from Manega, 1993. Hominin data from Hay, 1976.

2.1.1 Olduvai Bed II

Olduvai Bed II consists of the sediments between Tuff IF and Bed III (**Figure 4**). From base to top, Bed II can be divided into lowermost Bed II (largely similar to Bed I, dominated by a saline-alkaline lake and lake margin), the Lemuta Member (Eolian Tuff member, which includes Tuff IIA, the boundary between Lower and Middle Bed II), followed by a series of augitic sandstones and tuffs (including Tuffs IIB, the Birdprint Tuff, and Tuffs IIC and IID), interlayered with claystones and sandstones. As Bed II was being deposited, the local environment changed. At the base of Bed II lake and lake margin deposits dominate the record, and then a major disconformity associated with the Lemuta Member marks an environmental change that led to a decrease in the size of the Olduvai paleolake. This shrinkage coincides with a climatic shift from more humid to more arid conditions (Hay, 1976).

The tuffs of Bed II are typically reworked and discontinuous. They can vary in content of tephra and in some cases are thus not even properly "tuffs." Tuff IIA, for example, is locally a siliceous earthy claystone that contains about 10 percent mafic nephelinitic tephra (Hay, 1976). It is everywhere reworked and commonly contaminated. Where preserved, it is primarily mafic nephelinite with rock fragments, vitroclasts (with microphenocrysts of augite and minor nepheline, melilite, ilmenite, and perovskite), and augite crystals (Hay, 1976).

Tuff IIB is only locally preserved in the "junction" and side gorge at Olduvai. It is mostly an orange-brown contaminated tuffaceous sandstone and siltstone, with widespread conglomerates. At one site, relatively pure mafic nephelinite tuff with biotite forms the lower two meters of Tuff IIB (Hay, 1976).

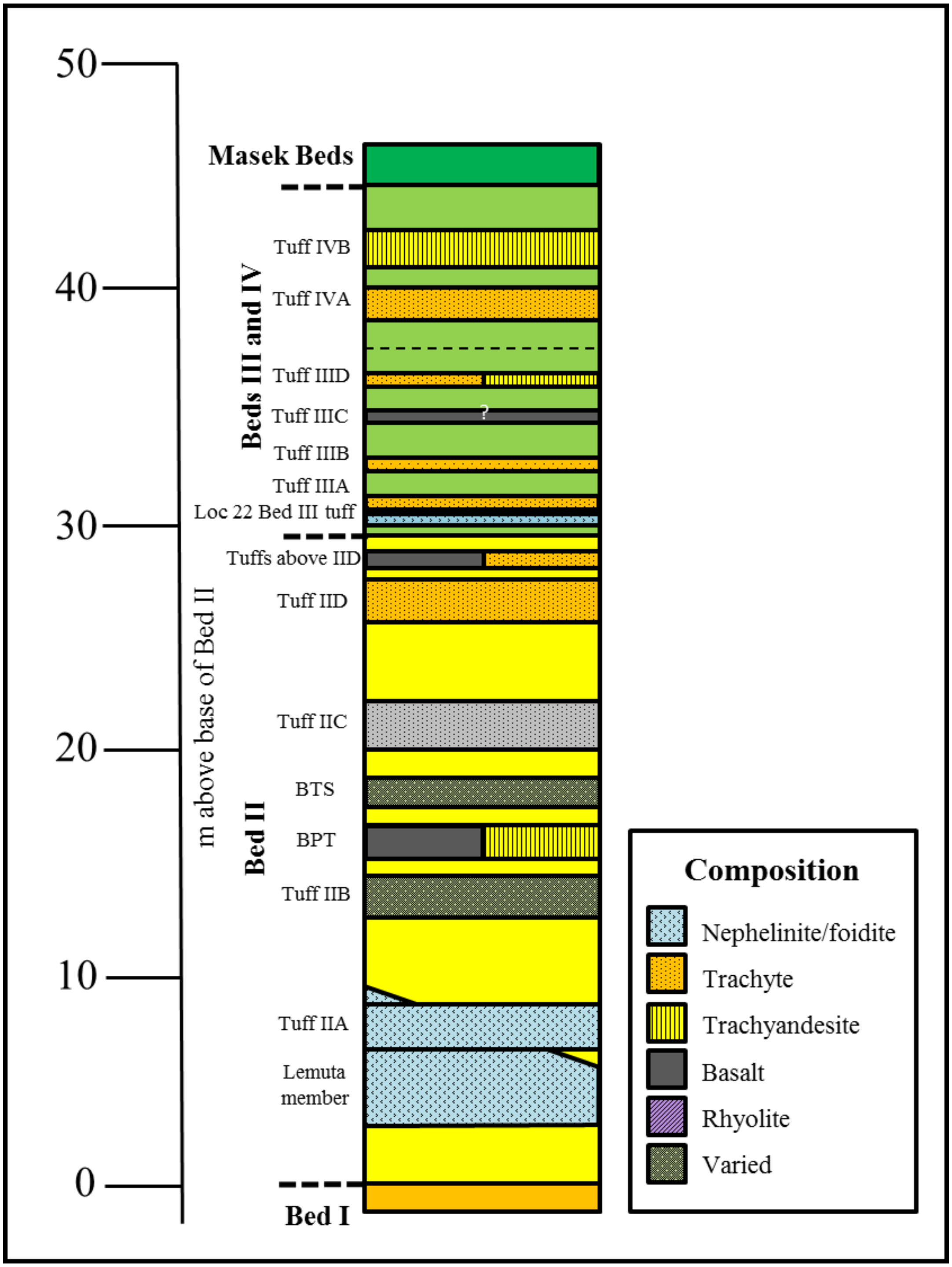

Figure 4. Stratigraphic column of Olduvai Beds II, III, and IV showing general compositions of volcanic tuffs and lavas. Bed II background is in yellow, and Beds III and IV are in light green. The composition of each tuff or lava is shown in the diagram and in the legend. Multiple compositions (where specified) are represented by two colors/patterns. Compositional data is from Hay (1976). BPT = Birdprint Tuff. BTS = Brown Tuffaceous Siltstone.

The Birdprint Tuff (BPT) is a thin, fine- to medium-grained tuff found mostly in the junction and side gorge (Hay, 1976). Its high-Ca plagioclase help distinguish it from other Bed II tuffs (McHenry et al., 2011).

Tuff IIC is an inconsistently preserved mafic vitric tuff and tuffaceous sandstone that is highly contaminated in most exposures. A tephrite composition is suggested by few crystals of plagioclase and nepheline in its vitroclasts (Hay, 1976).

Tuff IID is a vitric trachytic tuff with a distinctive composition and lithology. Phenocrysts of anorthoclase, hornblende, augite, and rare nepheline suggest phonolitic-trachytic composition. Rock fragments are dominantly trachyte and phonolite (Hay, 1976). Its hornblende and augite phenocrysts are distinctively high in Ti and Mg, which could help establish region-wide correlations (McHenry, et al., 2011).

Minor trachytic and basaltic tuffs occur locally in Bed II above Tuff IID (Hay, 1976).

Overall, Bed II and younger Olduvai tuffs are less continuous, finer grained, more reworked, and more contaminated than those of Bed I. With the exception of Tuff IID, none of the tuffs show evidence of surge or other near-source depositional features (McHenry, 2012b). In addition, there is a shift in the mineral assemblage from Ngorongoro rhyolites (Lower Bed I) and Olmoti trachytes (Upper Bed I) to an unidentified, likely more distal nephelinitic source (Bed II and more recent: McHenry 2012a, 2012b). Recent efforts to characterize Bed II tuffs have shown that their augite compositions are more Mg-rich than those of Bed I tuffs and previously studied NVH volcanoes (McHenry et al., 2008, 2011; Mollel et al., 2009, 2011).

2.1.2 Olduvai Bed III

Another possibility is that Embagai may have geochemical similarities with tuffs in Olduvai Bed III, which disconformably overlies Bed II. The majority of Bed III is reddish-brown volcanic detritus, which helps distinguish it from adjacent Beds II and IV in much of the gorge. Bed III is discontinuous, unlike Beds I and II, and is exposed over a much smaller area. Bed III tuffs are discontinuous; four vitric tuffs were identified within Bed III in the eastern part of the gorge (Hay, 1976).

Tuff 1 (Tuff IIIA) is found near the base of Bed III, and is the most widely recognized Bed III tuff. It is a fine- to medium-grained gray to reddish-brown vitric trachytic tuff with pumice and sodic plagioclase, and is best exposed in the eastern gorge. Tuff 2 (Tuff IIIB) is a biotite-bearing gray to reddish-brown fine-grained vitric trachyte tuff, Tuff 3 (Tuff IIIC) is course-grained orange-brown vitric tuff containing augite, olivine, and palagonitized mafic scoria particles. Tuff 4 (Tuff IIID) is yellow to pink fine-grained vitric tuff of trachyte or trachyandesite composition, with both plagioclase and anorthoclase with rare hornblende and augite. Two tuffs found in Bed III/Bed IV exposures to the north of Olduvai contain nepheline (Hay, 1976).

2.1.3 Dating the Olduvai Beds

Several Bed I marker tuffs have been dated using the $^{40}\text{Ar}/^{39}\text{Ar}$ method, and they range in age from 2.038 ± 0.005 to 1.803 ± 0.002 Ma (**Figure 5**, Naabi Ignimbrite to Tuff IF: Deino, 2012). The remaining beds have not been dated with such precision. Previous potassium-argon dating in Bed II proved to be unsatisfactory, either due to tuff reworking, contamination, or excess argon (Hay, 1976). Dates for Tuff IIA have included 1.71 Ma (Curtis and Hay, 1972) and a range of other ages ranging from 1.66 ± 0.1 to 1.74

± 0.03 Ma (Manega, 1993), however it has not yet been possible to confirm this age, or even narrow down the range (McHenry et al., 2007; de la Torre et al., 2012).

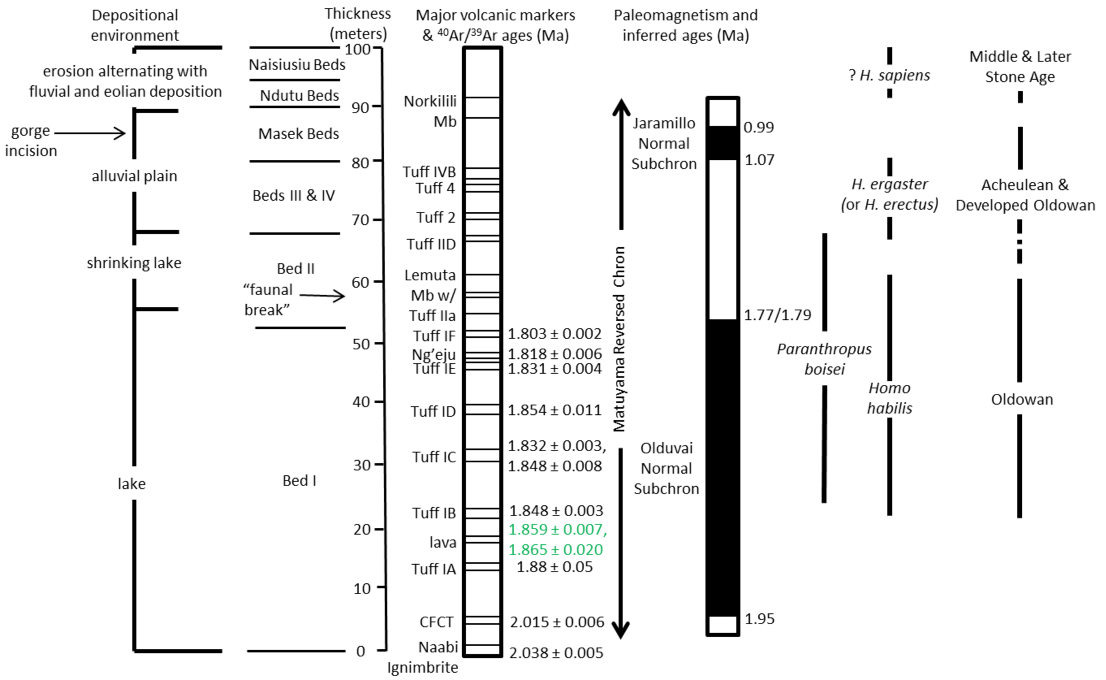

Figure 5. Schematic stratigraphy of Olduvai Gorge, showing principal beds and their depositional environment (Hay, 1976), paleomagnetism (Tamrat et al., 1995), main volcanic stratigraphic markers, their ^{40}Ar/^{39}Ar ages (Deino, 2012, except for lavas (green) by Walter, 1992), and the local stratigraphic extent of hominin taxa and artifact industries (Leakey and Hay, 1982). Modified after Klein (2009).

The Olduvai normal event was first identified for a basalt in Bed I by Grommé and Hay (1963) and dated at 1.8 Ma (Evernden and Curtis, quoted by Hay, 1963). The top of the Olduvai normal event has been identified in the lower part of the Lemuta Member in Bed II (Hay, 1976). At present, the top of Bed II is only constrained by its presumptive correlation to a major regional tectonic event, dated elsewhere at between 1.25 and 1.2 Ma (MacIntyre et al., 1974). The correlation is uncertain but should be tested with additional geochronological techniques (McHenry et al., 2007). The ages of Beds III and IV are only constrained by sedimentation rates or magnetic stratigraphy, with the Brunhes-Matuyama (0.78 Ma) provisionally identified in lower Bed IV above Tuff IVB (Hay, 1976). Application of Berggren et al. (1995) dates for the end of the Olduvai event (previously 1.67 Ma, now 1.77 Ma) and the Brunhes-Matuyama transition (previously 0.73 Ma, now 0.78 Ma) would result in older ages for Bed II (i.e. 1.28 Ma for the Bed II/III transition and 1.35 Ma for Tuff IID: McHenry et al., 2007).

However, Tamrat et al. (1995) proposed that the reverse to normal polarity transition recorded in Bed IV (N2) is the Jaramillo normal event instead. If this is the case, then the Bed II/III contact would be 1.34 Ma and Tuff IID would be 1.4 Ma, based on potentially unreliable sedimentation rates (McHenry et al., 2007). It should be noted that Tamrat et al. (1995) stated in regards to Hay's (1976) "weak chronological argument" that "Paradoxically, the magnetostratigraphy of this well-known site remained badly resolved, mainly because Bed III and Bed IV yielded unreliable paleomagnetic results and were considered as completely remagnetized".

2.2 Ngorongoro Volcanic Highlands (NVH) and surrounding areas

The Ngorongoro Volcanic Highlands (NVH), also known as the Crater Highlands, is a northeast-southwest trending elevated volcanic terrain that runs 90 km alongside the Salei Plain to the east of Olduvai Gorge (Dawson, 2008) (**Figure 1**, after Hay, 1976 and McHenry, 2012a; **Figure 6**, adapted from Luque et al., 2009). The NVH is the product of rifting along the eastern branch (or Gregory Rift) of the East African Rift System (EARS), adjacent to the boundary of the Tanzanian Craton and the Mozambique Belt (Dawson, 1992). Thick soil and vegetation on the eastern and southern sides of the Highlands make locating exposures difficult, thus making it difficult to establish the relative stratigraphy and age of the individual volcanic centers.

The NVH is dominated by the large caldera of **Ngorongoro** (olivine basalt, trachybasalt, trachyte; average K-Ar age of 2.40 Ma from plagioclase, 2.45 ± 0.15 from trachyte: Grommé et al., 1970; average K-Ar age of 1.94 Ma from ignimbrite: Manega, 1993; $^{40}Ar/^{39}Ar$ ages of 2.25 ± 0.02 to 2.01 ± 0.02 Ma: Mollel et al., 2008) in the southwest and several peaks and calderas to the northeast. Notable volcanic centers include **Ol Doinyo Lengai**, an active natrocarbonatite volcano with its first eruptive activity at c. 22 Ka, and located on the northeast flank of the NVH (Dawson, 1962, 1964, 2008), **Olmoti**, a Pleistocene caldera ($^{40}Ar/^{39}Ar$ ages of 2.01 ± 0.03 Ma to1.80 ± 0.01 Ma: Mollel et al., 2009) considered a source of Upper Bed I tuffs (McHenry et al., 2008; Mollel et al., 2009), and **Embagai**, a Pleistocene caldera with a large saline lake and one of the focuses of this study (see Section 2.21 for more detail).

Other volcanoes within the NVH include:

- **Kerimasi** – composition: nephelinite and phonolite, carbonatite at summit (Dawson, 2008); eruption age: bracketed between 1.1 and 0.4 Ma based on its relation to episodes of faulting (Hay, 1976).
- **Loolmalasin and Olsirwa** – composition: basanite, basalt, trachyte, with mugearite boulders found in streams (Paslick, et al., 1995); eruption age: Pliocene (Dawson, 2008), preliminary $^{40}Ar/^{39}Ar$ ages of ~1.4 to 1.3 Ma (Mollel and Swisher, 2012).
- **Oldeani** – composition: olivine basalt, basalt, ankaramite, trachybasalt, trachyte (exposed some 15-30 km south of its summit, Orridge, 1965); Eruption age: Pliocene (Dawson, 2008), $^{40}Ar/^{39}Ar$ age from 1.61 ± 0.01 to 1.52 ± 0.02 Ma (Mollel et al, 2011).

- **Lemagrut (Lemagarut)** – composition: olivine basalt, nephelinite, rare jacupirangite (Pickering, 1964); eruption age: Pliocene (Dawson, 2008), ^{40}Ar/^{39}Ar age from 2.40 ± 0.01 to 2.22 ± 0.10 Ma (Mollel et al., 2011).
- **Sadiman** – composition: nephelinite, phonolite, melilitite, carbonatite; Eruption age: Pliocene (Dawson, 2008), ^{40}Ar/^{39}Ar dates of 4.63 ± 0.05 to 4.02 ± 0.02 Ma (Mollel et al., 2011). A possible source for the phonolitic and melilititic ashes of the > 4.3 – 3.5 Ma Laetolil Beds (Hay, 1978; Dawson, 2008; Mollel et al., 2011).
- **Loguwinywo** – composition: basalt, nephelinite and nepheline-phyric phonolite; A previously unnamed mountain rising 300 m above the top of the rift escarpment on the eroded and incised eastern flank of Loolmalasin, between the peak of Loolmalasin and the village Kapenjiro (Dawson, 2008), in an area that locals call Loguwinywo (Greenwood personal communication, 2012).

To the east and north of the Manyara-Natron fault escarpment and the NVH lie more Neogene volcanic centers that could act as potential sources, including: **Burko** (composition: nephelinite; eruption age: Pleistocene: average K-Ar age of 0.97 Ma (Evans et al., 1971)); **Gelai (**composition: alkali basalt-trachyte; eruption age: Pliocene (Dawson, 2008); **Ketumbeine (**composition: alkali olivine basalt and trachyte; eruption age: Pliocene (Dawson, 2008); nephelinite from small late parasitic cone named Lolgurdolgonja (Guest, 1953));. **Engelosin, Mosonik,** and **Essimingor** are also nearby, but are too old or possess compositions that are significantly different from Olduvai Bed II and above tuffs (Evans et al., 1971; Isaac and Curtis, 1974; Hay, 1976; Manega, 1993; Dawson, 2008; Mana et al., 2012).

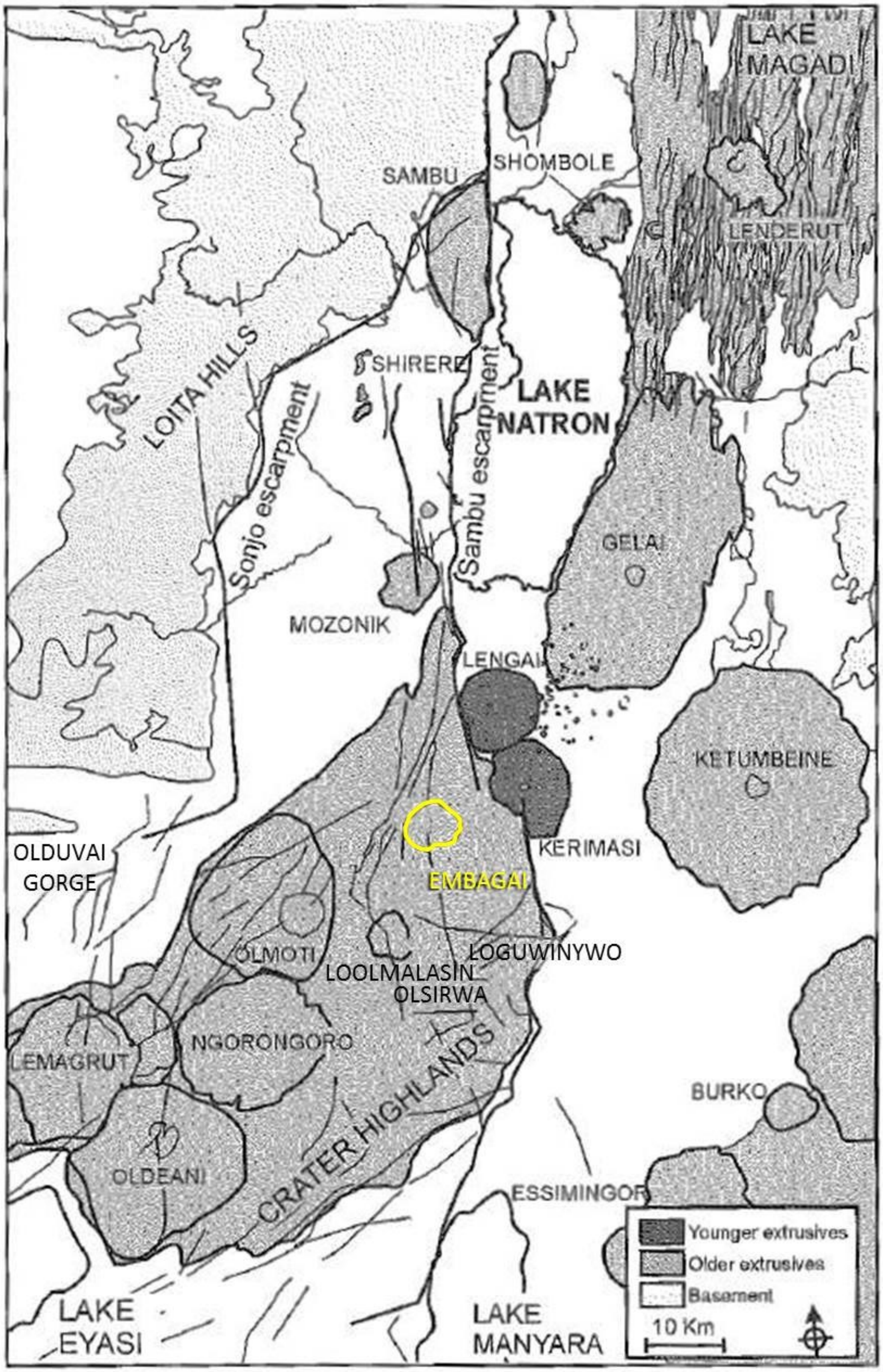

Figure 6. Detailed map of Ngorongoro Volcanic Highlands, with major volcanoes identified in relation to adjacent Olduvai Gorge and Lake Natron Basin. Embagai is highlighted in yellow. Modified after Luque et al., 2009.

2.2.1 Embagai caldera (Elanairobi)

Embagai (Empakai) is an open caldera that sits within the Elanairobi volcano in the NVH, between Olmoti and Ol Doinyo Lengai (**Figure 6**). The Jaeger summit of the Elanairobi complex rises to 3235 m. Its caldera measures 6.8 (north-south) x 7.8 km (east-west), with the entire mountain 30 km across. Within the eastern part of the caldera lies Lake Embagai, a saline lake 3.5 km across and standing at 2209 m (Dawson, 2008).

The lower parts of Embagai's caldera walls have flows of trachybasalt, whereas the upper parts are nephelinite and aegirine phonolite. Limburgite (vesicular basanite high in augite and olivine but low in feldspar) flows occur at the base of the caldera walls. Small parasitic cones on the caldera floor contributed trachybasalt tuffs to the caldera floor and walls. Tuffs crop out on the western and northeastern outer slopes, and over the Jaeger summit. Finally, on the lower northern slopes, trachybasalt tuffs overlie flows of basanite, nephelinite, and olivine basalt at the gorge of Engare Sero (**Figure 7**: Guest et al., 1961; Dawson, 2008).

Its composition has been more recently described as nephelinite and phonolite (foidite) (Mollel, 2007; Mollel et al., 2009). Petrographic analysis on four samples (Mollel, 2007) revealed that its lavas are phaneritic, porphyritic, and coarse to fine-grained in texture. The nephelinites are Fe-rich, with FeO content ranging from 2.7-4.8 wt% (Mollel, 2007). Mollel's (2007) Embagai samples included nepheline, augite, andradite garnet, sphene (titanite), melilite, apatite, titanomagnetite, and rare amphibole.

Using trace element geochemistry, Mollel (2007) highlighted High Field Strength Element (HFSE) ratios (e.g. Zr/Nb, Hf/Nb, La/Nb) that varied between different volcanic centers in the NVH. He determined that Embagai shares geochemical similarities with nearby Engelosin and Satiman volcanoes, including high concentrations of Large Ion Lithophile Elements (LILE). His geochemical findings suggested derivation by relatively low degree partial melting of parent rock and that fractionation was among the processes that produced the Embagai lavas. Mollel's (2007) Sr and Nd isotopic study concluded that all of the NVH lavas experienced varying degrees of crustal contamination.

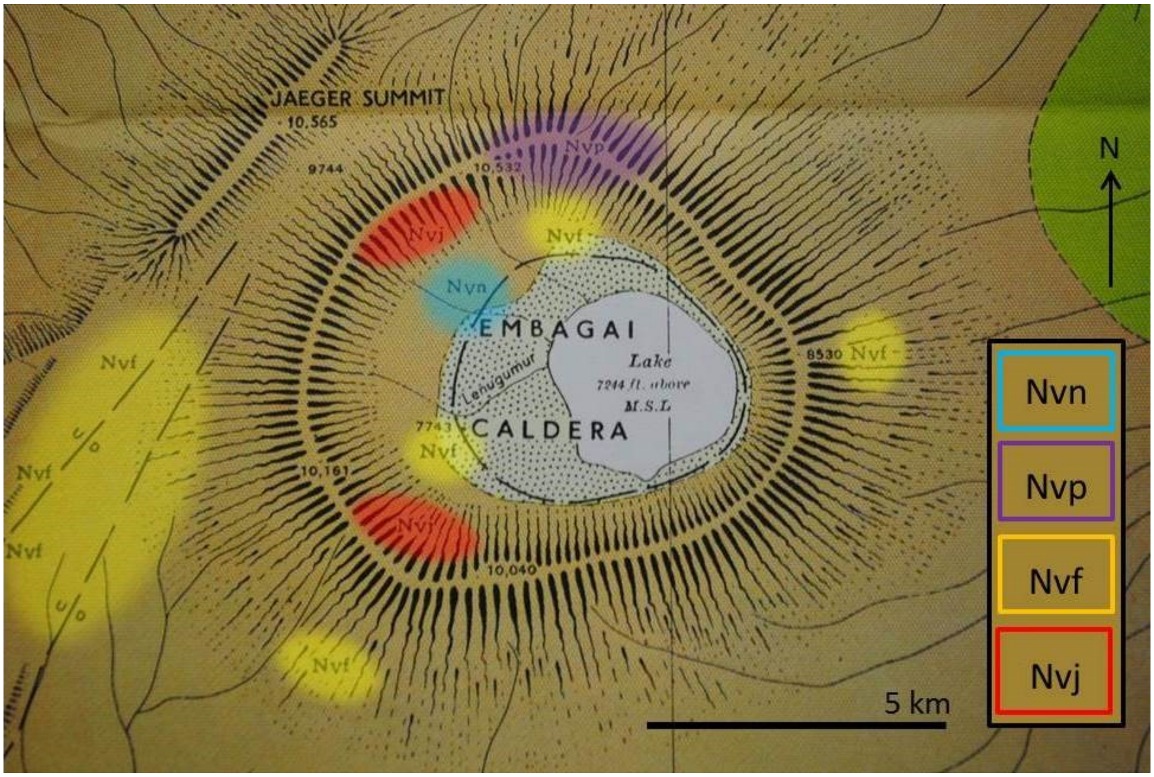

Figure 7. Geologic map of Embagai with units distinguished by color. Nvn (blue): nephelinite. Nvp (purple): phonolite. Nvf (yellow): mica-augite tuffs. Nvj (red): red scoria and tuffs (or agglomerate). Elevations are in feet. Base image from Guest et al., 1961.

Embagai has been radiometrically dated in two separate studies, summarized in Mollel and Swisher (2012). Manega (1993) dated three samples from the nepheline-bearing lavas exposed along the caldera rim using the K-Ar method. These three samples yielded dates of 0.5 ± 0.14, 1.05 ± 0.02, and 1.52 ± 0.03 Ma, suggesting activity of

Embagai for about one million years. However, the young age of the first sample (0.5 ± 0.14 Ma) is considered to be of poor precision because of its low radiogenic yield of 4.2%. Manega (1993) also performed single crystal laser fusion on one Embagai tephra sample (same sample as the 1.52 Ma age), resulting in an age of c. 0.6 Ma. Mollel (2007) dated four samples from Embagai using the $^{40}Ar/^{39}Ar$ method, yielding ages from 0.81 ± 0.02 Ma to 1.16 ± 0.04 Ma. This partially overlaps the previous age range reported by Manega (1993). Mollel also noted that the dates may have been affected by low temperature alteration of the samples, perhaps related to the loss of potassium from the rock.

2.3 Natron basin/Peninj region

The Natron basin (**Figure 8**) forms part of a long chain of tectonic basins that make up the Gregory Rift, the southern part of the eastern branch of the Great Rift Valley (Luque et al., 2009). It is located in a complex zone a few kilometers north of the Northern Tanzania Divergence Zone (Dawson 1964; Dawson and Powell, 1969), which gave rise to intense volcanism in the NVH area and the splitting of the eastern branch of the Rift Valley in three structural directions (Luque et al., 2009).

The Peninj Group (**Figure 9**) is the primary Pleistocene sedimentary series exposed on the western margin of the Natron basin, and is now exposed mostly along the Moinik Ramp between Oldoinyo Sambu and Mozonik volcano. The most complete exposure of the Peninj Group is accessible at the Type Section (Maritinane) along the Peninj River (Isaac, 1967; Luque et al., 2009). The Natron basin and Peninj are in part famous for the discovery of an *Australopithecus boisei* (now *Paranthropus boisei,* Wood and Constantino, 2007) mandible at the base of the Main Tuff in the Peninj Type Section

(Leakey and Leakey, 1964). Oldowan and Acheulean stone tools are also found in Peninj sediments.

Isaac (1965, 1967) first described the stratigraphy of the Natron basin, and subdivided the Peninj Group into the Humbu and Moinik Formations. Lavas at Peninj include the Sambu (derived from Oldoinyo Sambu) and the younger Hajaro basalts, both of which underlie the Peninj Group sediments, along with younger lavas in the Humbu and Moinik Formations (Luque et al., 2009). Paslick et al. (1995) analyzed flows of basanites, nephelinites, and picro-basalts at the south end of Lake Natron, but were unsure whether they originated from Sambu or Elanairobi (Embagai). Hay first determined the magnetic polarity of lavas west of Lake Natron using a portable fluxgate magnetometer (from Isaac, 1967). Isaac and A. Mussett subsequently collected a series of oriented samples that were studied by T. Reilly. The results were unpublished but were referenced by Isaac (1967). The underlying Sambu lavas recorded normal polarity, and Hajaro lavas between the Sambu lavas and the Humbu Formation recorded consistent reversed polarity (Isaac, 1967). Isaac (1967) concluded that based on stratigraphy, paleomagnetism, paleontology, and archaeology, the Peninj Group was Middle Pleistocene, with the Humbu Formation possibly contemporary with the upper part of Olduvai Bed II. Luque et al. (2009) provide a detailed description of the geology of the Natron basin and Peninj area, building on previous work by Isaac (1965, 1967).

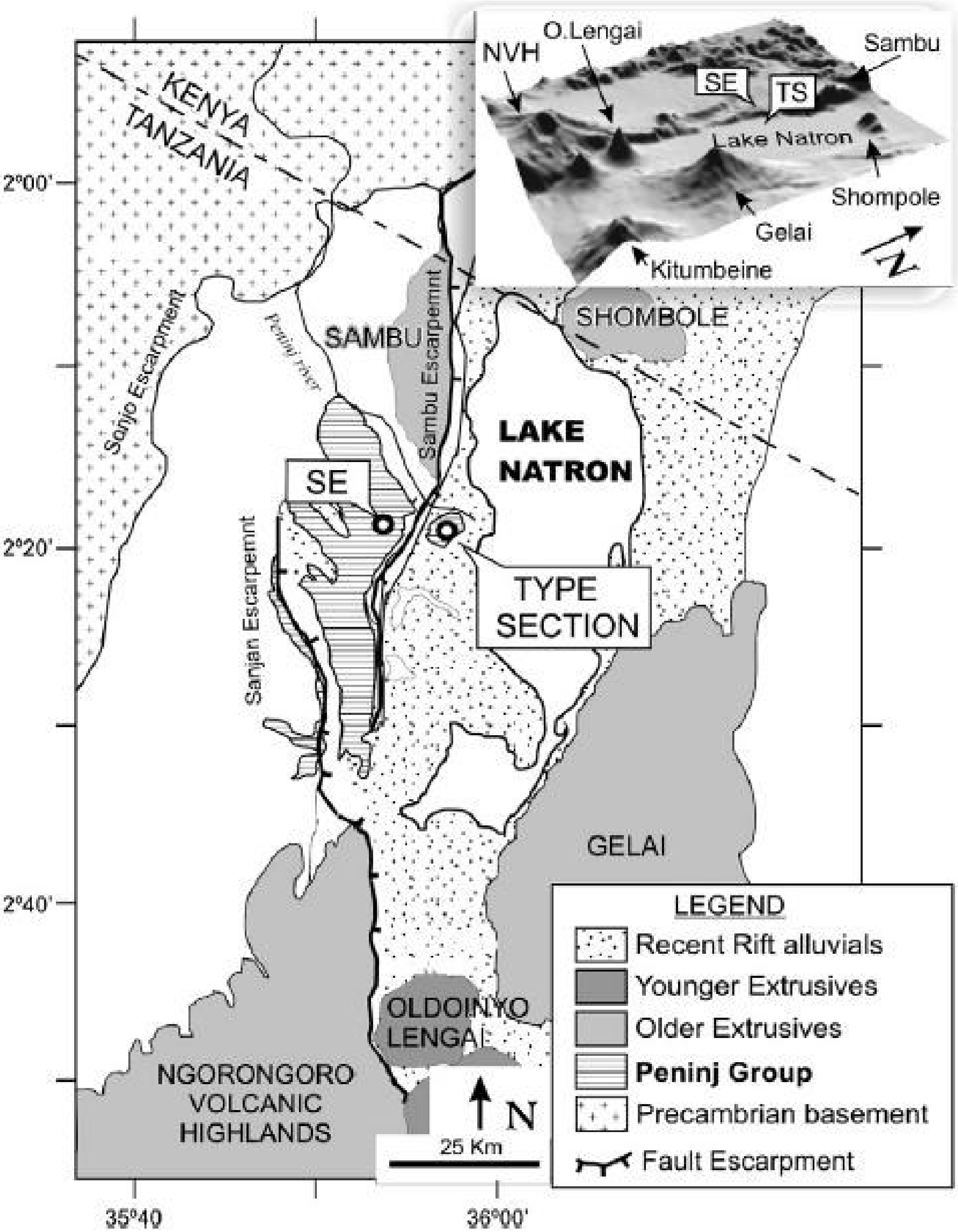

Figure 8. Map of the Natron basin, showing the extent of the Peninj Group and the locations of the Maritanane Type Section (TS), Sambu Escarpment, and Sanjan Escarpment. Figure after Luque et al., 2009.

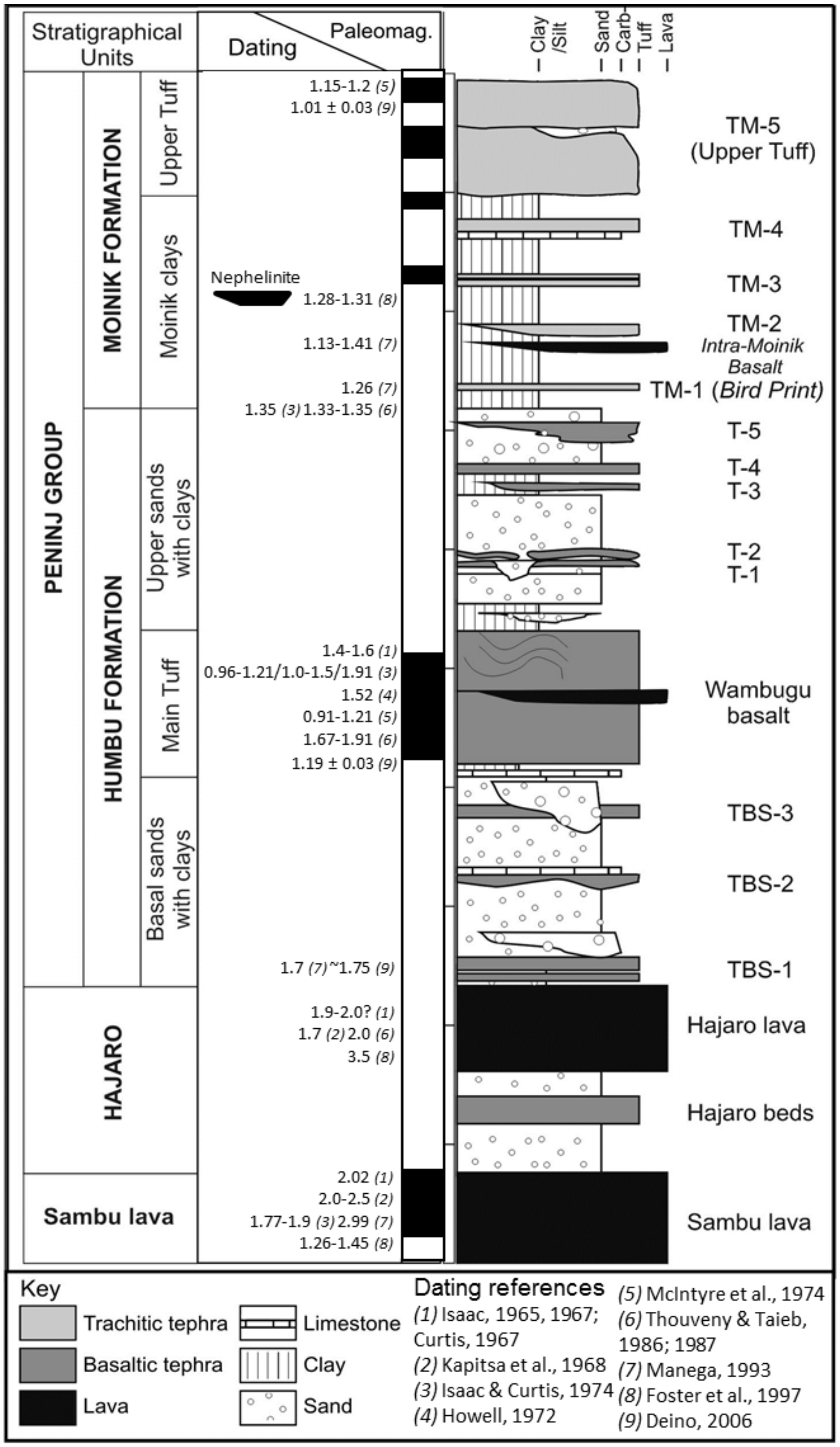

Figure 9. Composite stratigraphic column of the Natron basin. Modified after McHenry et al., 2011, after Luque et al., 2009 and Isaac, 1965, 1967. Dating references included in figure. Paleomagnetics from Thouveny and Taieb, 1986; 1987; Tamrat, 1995. Black is normal, white is reversed.

The Main Tuff of the Humbu Formation acts as a stratigraphic marker. Along the southern Moinik Ramp along Lake Natron south of the Peninj Group Type Section, the Main Tuff contains a lava called the Wa Mbugu basalt. In the Type Section, the Wa Mbugu is absent from the Main Tuff (Luque, 2009). The Wa Mbugu basalt has been dated from as early as 1.91 Ma and as late as 0.96 Ma, with a conservative median at 1.5 Ma (Luque et al., 2009). This is consistent with a previous K-Ar range of 1.4-1.6 Ma on an “olivine basalt” within the Humbu Formation as determined by Isaac (1965, 1967) and Curtis (1967). At that time, the Wa Mbugu was measured as normal polarity by Hay using a portable fluxgate magnetometer (from Isaac, 1967). Normal polarity was confirmed by paleomagnetic sampling and analyses (Isaac and Curtis, 1974; Thouveny and Taieb, 1986, 1987). It has been debated whether the Wa Mbugu fell within the Olduvai normal event (Isaac and Curtis, 1974; 1.67 to 1.87 Ma, Thouveny and Taieb, 1986, 1987) or the Jaramillo normal event (1.053 ± 0.006 to 0.986 ± 0.005 Ma, Singer et al., 1999). If the younger Wa Mbugu dates are accepted, then the Jaramillo could be considered, thus making the hominin mandible and industry for that area much younger than originally thought. The brief Cobb Mountain normal event (1.12 ± 0.02 Ma; Mankinen et al., 1978; 1.190 - 1.215 Ma, Channell et al., 2002) has also been considered (Deino, 2006; Luque et al., 2009). It should be noted that the introduction of potassium during zeolitization could have affected the accuracy of the early K-Ar age dates, with the most heavily altered samples providing the anomalously young ages (Hay, in Isaac and Curtis, 1974). However, Deino’s (2006) single-crystal $^{40}Ar/^{39}Ar$ dates are also young, and should have been less affected by zeolitic alteration.

3. METHODS

3.1 Field methods

Lava and tuff samples were collected from Embagai caldera in 2012 (12EM01-15, shortened hereafter as EM01-15, **Figure 10a**) in areas previously sampled by Mollel (2007, **Figure 10b**) and in areas not previously studied, to acquire a more complete record of variation in composition for the volcanic center. The caldera floor (**Figure 12**), western flank (**Figure 13**), eastern rim (**Figure 14**), and northern rim (**Figures 15** and **16**), and were chosen as sites for collection. Less than 1 kg was collected for each sample, where possible from fresh exposures. One additional Embagai sample (LM13-T32, shortened hereafter as 13-T32) was collected in 2013 by McHenry on a fresh exposure of the eastern rim.

Samples from the Natron basin were previously collected by McHenry between 2007 and 2012 (**Figure 11**). In this thesis, samples of the Wa Mbugu, Sambu, and Hajaro Basalts are compared geochemically to unknown samples collected throughout the area, including the presumed source of the Wa Mbugu. This thesis also includes a paleomagnetic study of two basalt samples, one identified as Wa Mbugu and a second postulated to be either Wa Mbugu or Hajaro, to determine if they have normal (thus potentially attributable to the Olduvai, Jaramillo, or Cobb Mountain events) or reversed (Matuyama chron) polarity, constraining the age of these units.

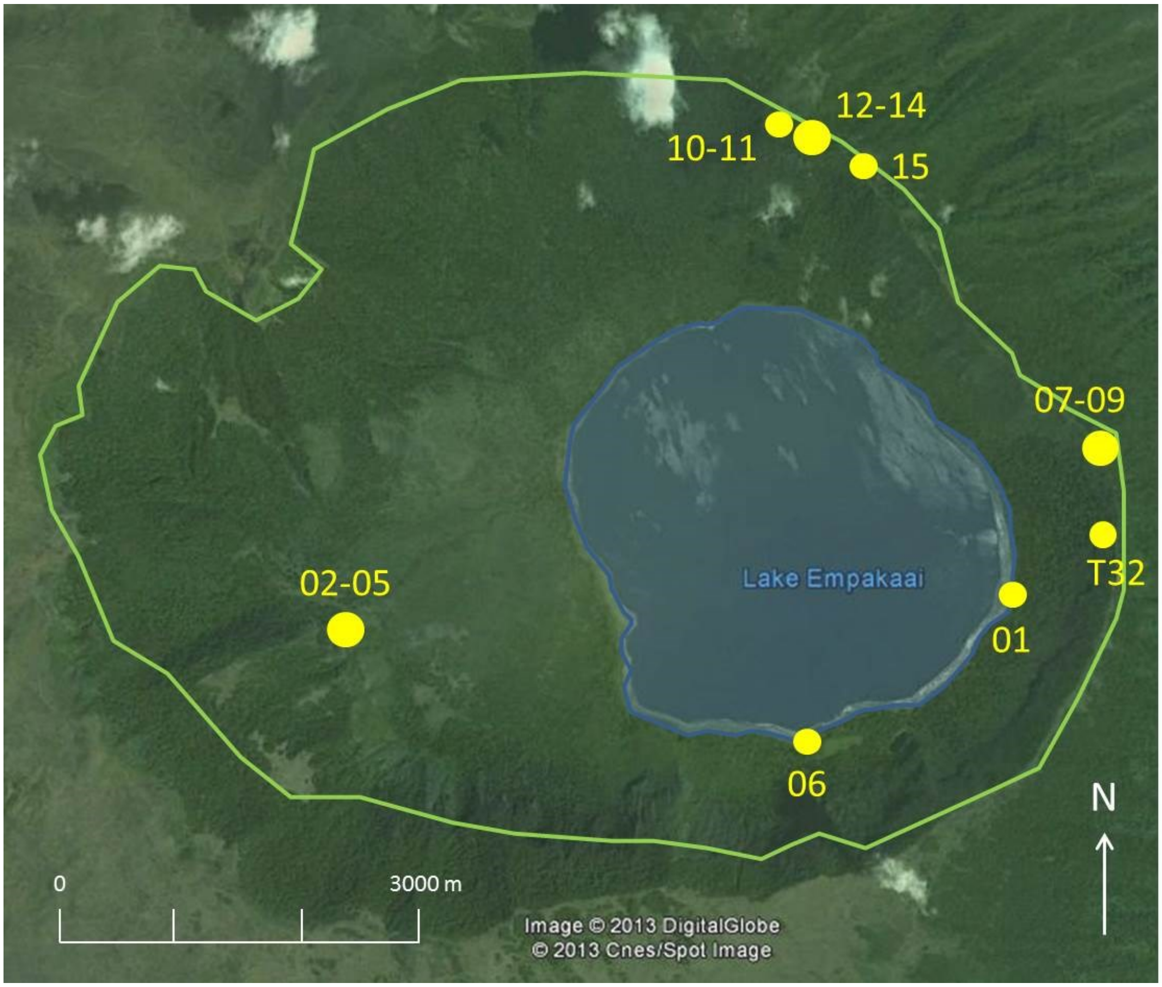

Figure 10a. Google Earth map of Embagai with locations of sites. Sample locations cluster in four main areas: western flank (EM02-05), eastern rim (EM07-09 and 13-T32), northern rim (EM10-15), and caldera floor (EM01 and EM06).

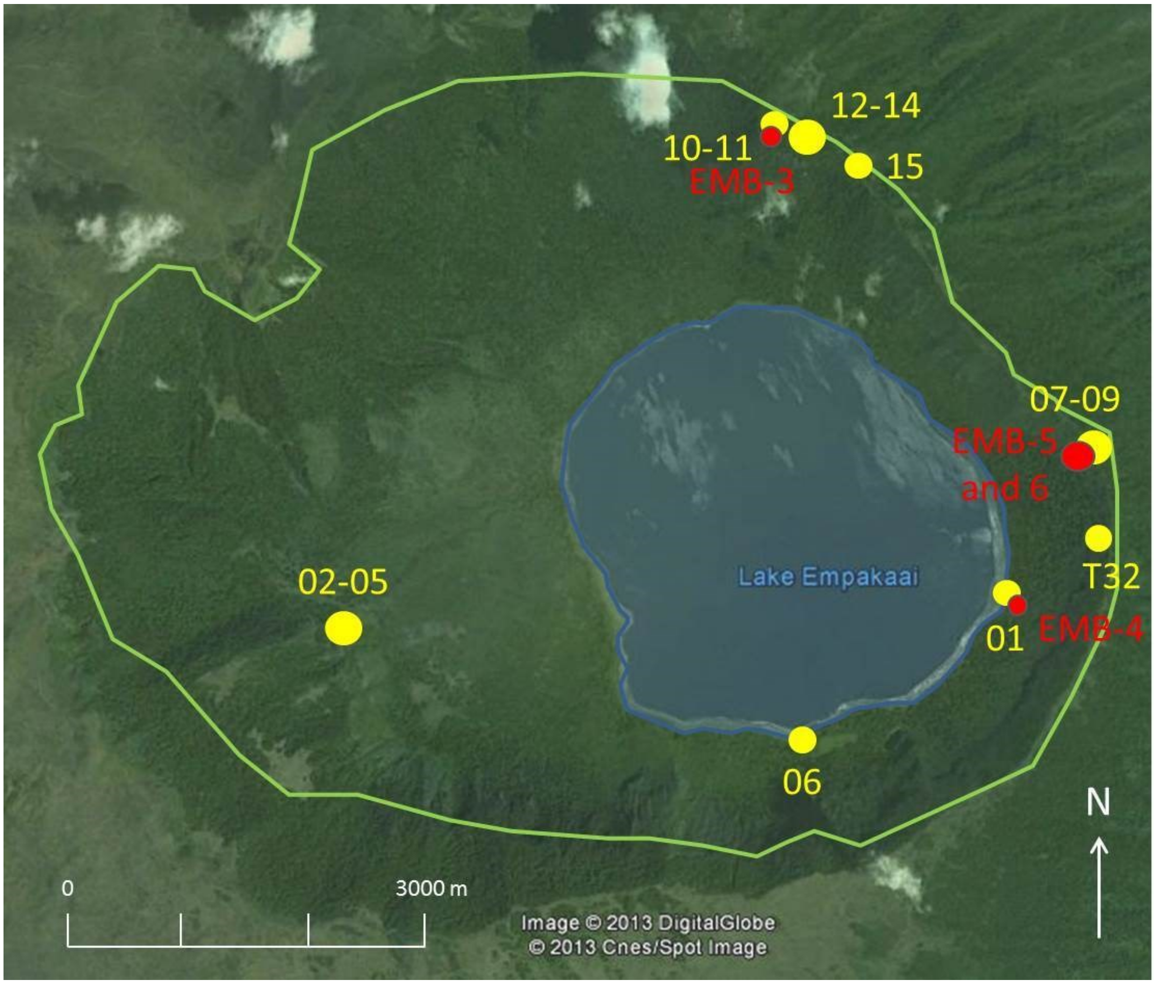

Figure 10b. Google Earth map with Mollel's (2007) samples added (EMB-X). Note general overlap in collection area in eastern rim, northern rim, and eastern caldera floor.

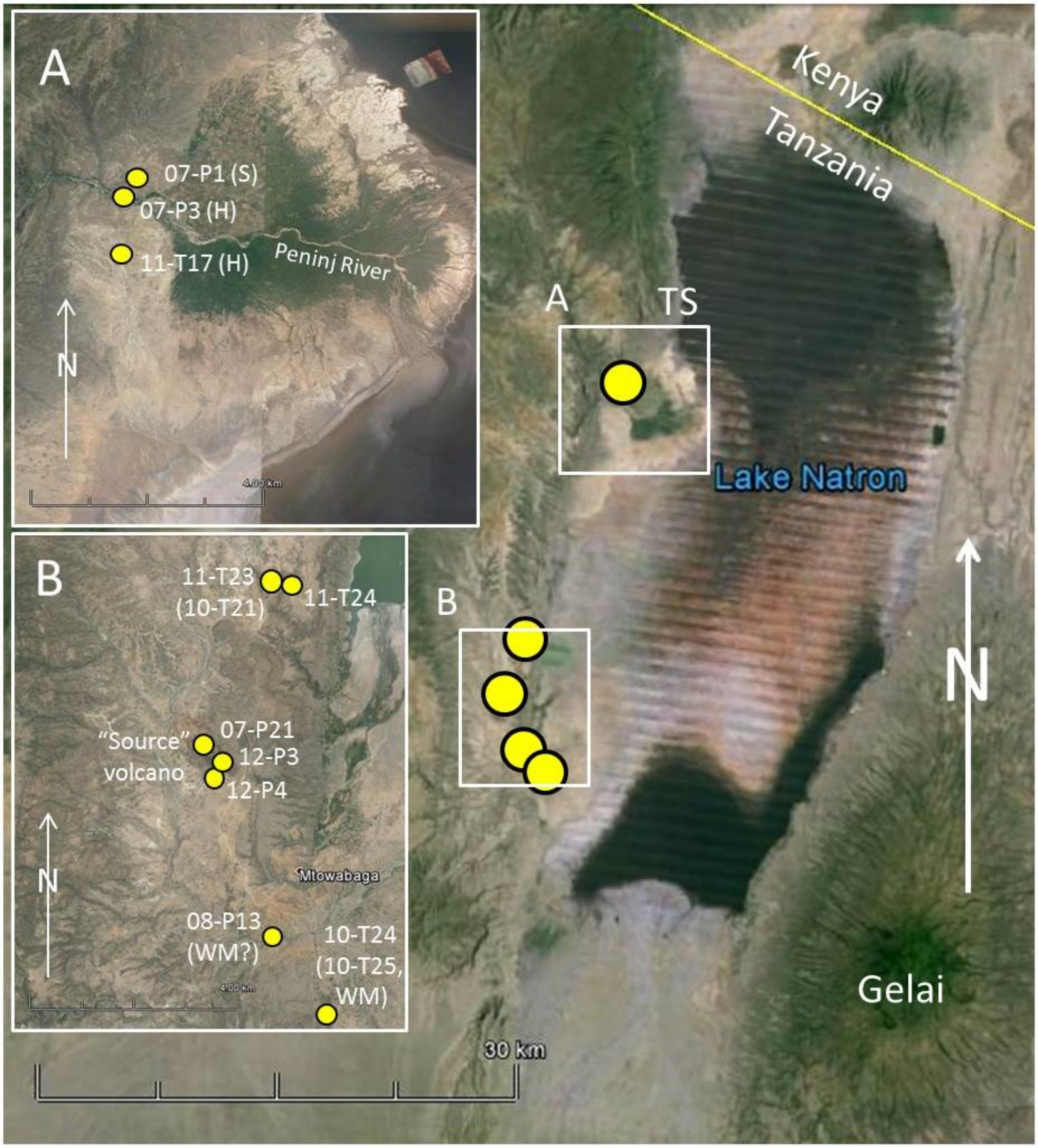

Figure 11. Google Earth map of the western Natron basin with locations of collection sites. Inset scales are 4 km long. Inset A details the Peninj Type Section (TS). Inset B details the Mtowabaga area and the area surrounding the hypothesized "Humbu source" volcano. 10-T21 and 10-T25 are oriented samples. Letters in parentheses refer to: S = Sambu, H = Hajaro, WM = Wa Mbugu.

3.1.1 Field details of Embagai

Samples at Embagai were designated as EM followed by a number in order of collection. They are summarized in **Table 1.** Samples will be discussed here by location of collection.

EM01 and EM06 represent the caldera floor parasitic cones that outcrop adjacent to Lake Embagai (**Figure 12**). These samples contain a dark gray matrix with euhedral hexagonal crystals of nepheline averaging 0.5-1 cm as observed in hand sample, and show some evidence of alteration.

EM02-EM05 were collected at a previously unvisited location on a lower slope of the western rim (**Figure 13**). Heavy vegetation limited sampling to cattle trails. In the field, EM02 appeared light to dark gray and fine grained, and possessed a conchoidal fracture. EM03 was similar but also had secondary zeolite-filled vesicles.

EM07-EM09 were primarily agglomeritic samples collected on the eastern rim of Embagai, along the main footpath to the caldera floor (**Figure 14**). EM07 possesses euhedral rectangular pyroxenes with a black vitreous luster, measuring about 1 mm across. EM08 contains dark blue phenocrysts in a dark matrix. Adjacent EM09 is a very fissile white tuff with phenocrysts. LM13-T32 (shortened hereafter as 13-T32), collected by McHenry in 2013, was found on a fresh exposure along the eastern rim wall, south of the remaining eastern rim samples. It possesses 1-5mm euhedral grains, without much evidence for alteration. Near this sample was a carbonate cave that exhibited flowstone.

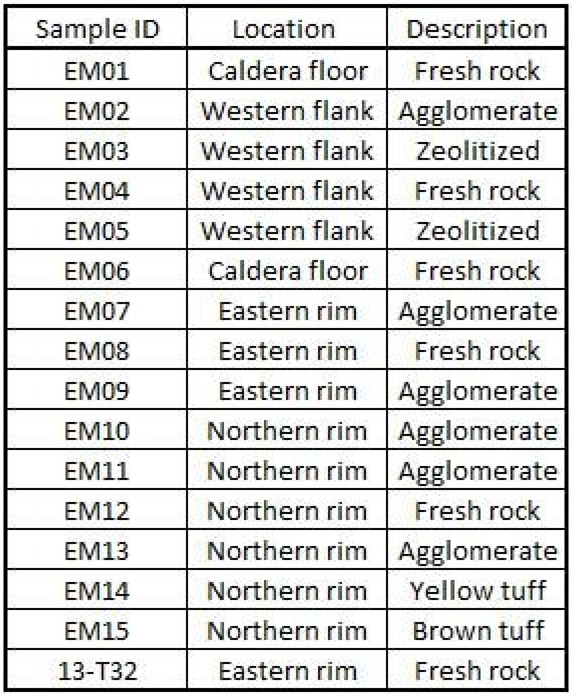

Sample ID	Location	Description
EM01	Caldera floor	Fresh rock
EM02	Western flank	Agglomerate
EM03	Western flank	Zeolitized
EM04	Western flank	Fresh rock
EM05	Western flank	Zeolitized
EM06	Caldera floor	Fresh rock
EM07	Eastern rim	Agglomerate
EM08	Eastern rim	Fresh rock
EM09	Eastern rim	Agglomerate
EM10	Northern rim	Agglomerate
EM11	Northern rim	Agglomerate
EM12	Northern rim	Fresh rock
EM13	Northern rim	Agglomerate
EM14	Northern rim	Yellow tuff
EM15	Northern rim	Brown tuff
13-T32	Eastern rim	Fresh rock

Table 1. Embagai samples by collection location and type.

EM10-EM14 are more crystalline samples collected on the northeastern rim, along an overgrown path leading to a communications tower (**Figures 15** and **16**); EM15 was collected at the junction of this path and the caldera rim road. EM15 is a brown-orange tuff with 1 cm biotite plates observed in hand sample. Both EM10 and EM11 were collected at the westernmost extent of collection on the northern rim. They are a mixture of agglomerate and crystalline rock, with nepheline phenocrysts present in the crystalline portion. EM12 is gray crystalline rock with fine grained phenocrysts measuring ~1mm. EM13 is a fine grained gray to white agglomerate with biotite sheets. EM14 is a very fine grained and fissile gray-yellow tuff with yellow lapilli. The outcrop at EM14 is dipping about 25° towards the northeast.

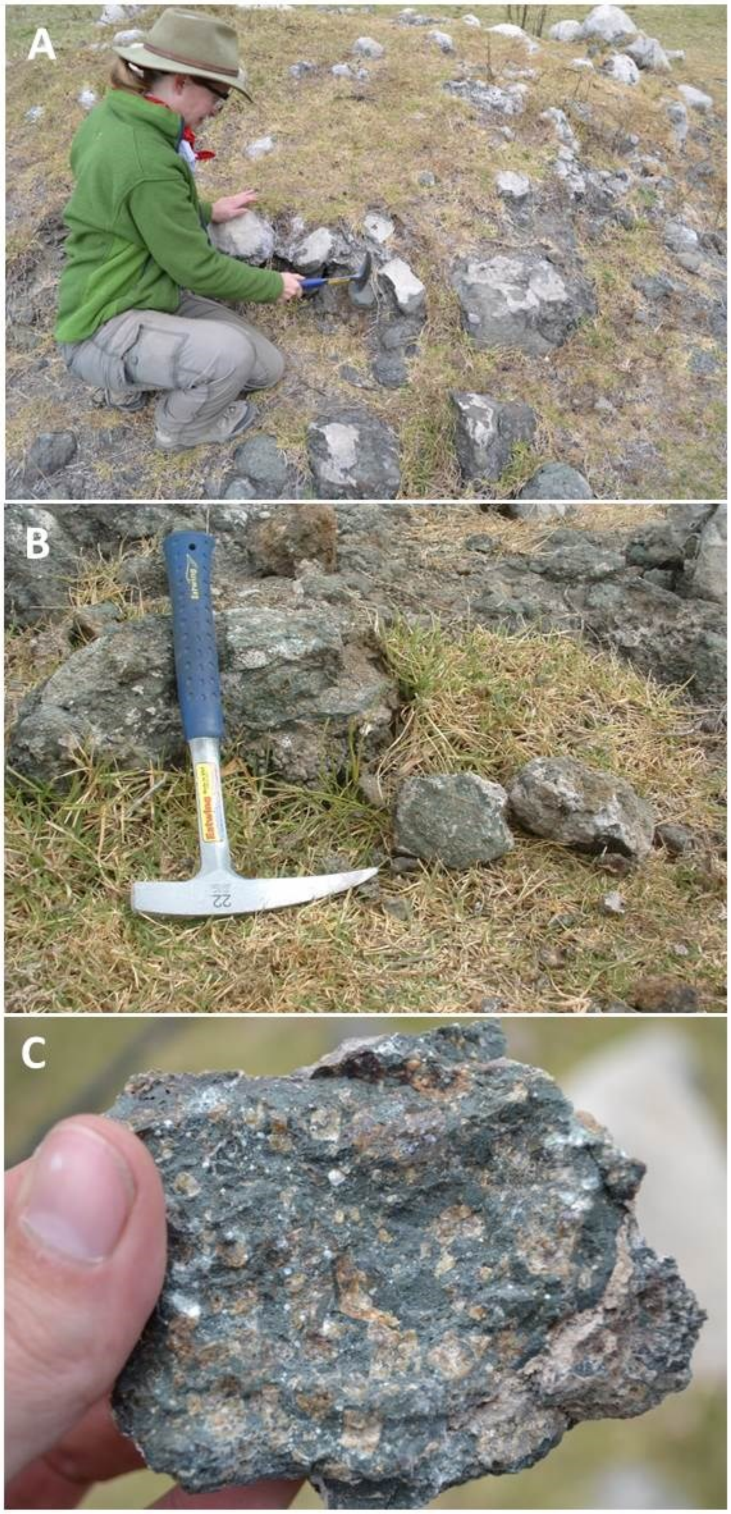

Figure 12. Field photographs of the caldera floor and parasitic cones of Embagai. **(A)** McHenry samples one of the parasitic cones on the caldera floor. **(B)** EM01 exposed as a parasitic cone adjacent to Lake Embagai. Rock hammer for scale. **(C)** Detail on EM06 hand sample shows euhedral nepheline mineralogy. Thumb for scale.

Figure 13. Field photographs of the western flank of Embagai. **(D)** EM02 as exposed on a cattle trail. Camera lens for scale. **(E)** EM03 as exposed on same trail. **(F)** EM04 farther down the trail displays conchoidal fracture. Rock hammer for scale.

Figure 14. Field photographs of the eastern rim of Embagai. **(G)** Detail on EM07 hand sample. Note the euhedral pyroxenes. Thumb for scale. **(H)** EM08 as exposed along primary access path to the caldera floor. Adjacent EM09 (not pictured) is a tuff, indicating emplacement by an explosive eruption. **(I)** 13-T32 as collected in field. Rock hammer for scale. **(J)** View of cave at 13-T32 location on eastern rim of Embagai. Window inset is equal in size to (K). **(K)** McHenry and field assistant Brendan Fenerty for scale. **(L)** Interior of cave exhibits flowstone features, consistent with carbonate.

Figure 15. Field photographs of the northern rim of Embagai. **(M)** EM10 in overgrowth. Jacob's staff is 1.6 m tall. **(N)** EM11 with rock hammer for scale. Euhedral nepheline was observed in the field. **(O)** View of overgrown vehicle trail along rim, demonstrating lack of fresh exposures. Maasai guide for scale. **(P)** Outcrop exposed below EM11. Greenwood for scale.

Figure 16. Field photographs of the northern rim of Embagai. **(Q)** EM12 with Jacob's staff for scale. Staff is 1.6 m tall. **(R)** Detail on EM12. **(S)** EM13 showing agglomerate texture. **(T)** EM14 containing fine-grained yellow lapilli. Lapilli tuff is exposed at about 25° angle to the northeast. **(U)** EM15 as tuff exposed on Embagai Rim Road at entrance to jeep trail. **(V)** Detail of EM15 shows biotite plates ~1 cm in diameter.

3.1.2 Field details of the western Natron basin

Samples in this series are numbered according to year collected and order of collection. All samples were collected by McHenry.

The base of the "definitive" Wa Mbugu basalt was sampled in 2010, at the base of the escarpment along the Engare Sero-Peninj road. There, the massive lava flow is constrained within the distinctively thick and orange Main Humbu Tuff (**Figure 17A**). Samples 10-T24 and 10-T25 were collected from the base of the flow (**Figure 17B**). 10-T25 is an oriented sample collected for paleomagnetic analysis. The top was horizontal, and its orientation was determined using a Brunton compass. 10-T24 is a geochemical split of 10-T25.

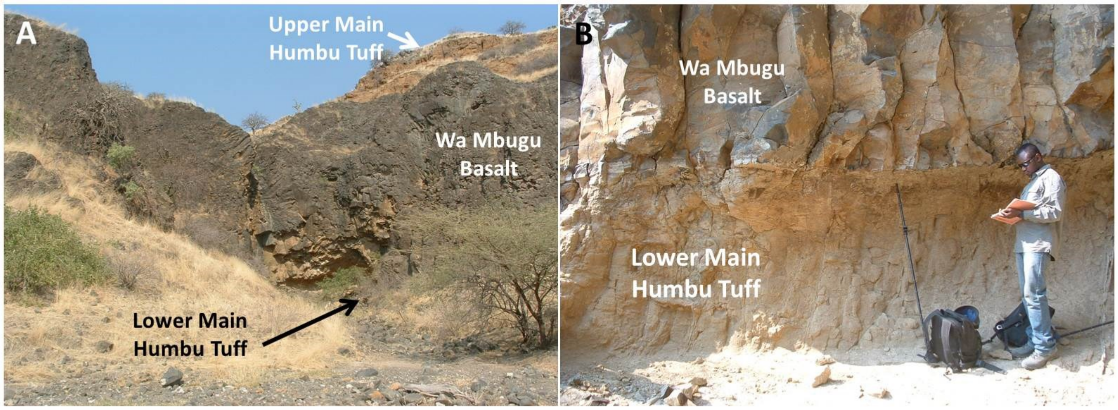

Figure 17. Field photographs of the Wa Mbugu basalt in the western Natron basin. **(A)** The Wa Mbugu lava south of the Peninj type section, constrained within the orange Main Humbu Tuff. **(B)** Close-up of Wa Mbugu sample 10-T24 sampling site. Field assistant Simon Gerald and Jacob's staff for scale. Jacob's staff is 1.6 m tall.

Sample 08-P13 likely represents the top of the Wa Mbugu (**Figure 18D**). It was collected a short hike from the Sale-Engare Sero escarpment road, from the top of a massive lava flow that made up the floor of its drainage. Up the Moinik ramp, along the

Sale-Engare Sero road, two basalts of uncertain stratigraphic position were collected from the top of a lava flow exposed in a stream bed. Sample 10-T21 and 11-T23 represent the same lava flow near the base of the section (**Figure 15, C, and E**). This lava underlies the Main Humbu Tuff, which is well developed at this site. Based on relative stratigraphic position and appearance it could reasonably be interpreted as either the Hajaro lava (in which case the lower part of the Humbu Formation is abbreviated) or the Wa Mbugu (in which case the lower part of the Main Humbu Tuff, which typically underlies the Wa Mbugu, is locally absent). An oriented sample (10-T21) was collected at the top of this lava. Its top was horizontal, and its orientation was measured using a Brunton compass.

The second lava (sample 11-T24, **Figure 18F**) caps the overall section, which includes both the thick Main Humbu Tuff and an overlying thick section of green lacustrine sediments (with interlayered minor tuffs) that resembles the Moinik Formation. This lava could reasonably represent the Intra-Moinik Tuff. The lavas represented by samples 11-T23 and 11-T24 are separated by tens of meters of continuous section.

Samples 07-P21, 12-P3, and 12-P4 were collected atop and directly adjacent to the presumed source of the Wa Mbugu lava, an unnamed, small, eroded volcano near the top of the escarpment (**Figure 20aI, J,** Isaac, 1967). This volcano has exposures of coarse, steeply-dipping orange volcaniclastic materials, along with stacked (and heavily vegetated) lava flows. 07-T21 was collected at the summit (**Figure 20aI**), 12-P3 on the upper slopes (**Figure 20bM, N**), and 12-P4 from a flow emerging from the base of the cone (**Figure 20aK, L**).

Figure 18. Field photographs of unidentified lavas in the western Natron basin. **(C)** 10-T21 (on ground), an oriented sample and possible Wa Mbugu basalt. Upper Main Humbu Tuff along wall in background. Scientist and Maasai scout for scale. **(D)** 08-P13, possible top of Wa Mbugu. Maasai scout for scale. **(E)** 11-T23, a duplicate of 10-T21 and likely Wa Mbugu. Rock hammer for scale. **(F)** 11-T24, a unit above 11-T23 and the Main Humbu Tuff, possibly representing the Intra-Moinik basalt. Field guide and rock hammer for scale.

Figure 19. Field photographs of identified lavas in the western Natron basin. **(G)** Sambu lava (07-P1) as outcrop at the Peninj Type Section. Backpack for scale. **(H)** Hajaro lava (07-P3) as outcrop. Backpack and rock hammer for scale.

Sample 07-P3 represents the Hajaro lava (**Figure 19H**) and was collected at the Peninj Type section (Maritanane). Exposures in the area are poor and this sample was significantly altered, with zeolite-filled vesicles. The site was re-visited in 2011 to collect a cleaner sample: 11-T17 still has zeolites, but contains better-preserved phenocrysts and is less rotten. Sample 07-P1 represents the Sambu lava at the Peninj Type Section. The Sambu lava is massive here; it was sampled 125 cm from its base, above a notably vesiculated layer.

Figure 20a. Field photographs of lavas near a source volcano in the western Natron basin. **(I)** View of the hypothesized source volcano of the Wa Mbugu lava and the Main Humbu tuffs. **(J)** 07-P21 as exposed at the summit of the volcano in (I). Field notebook for scale. **(K)** 12-P4 as exposed at the foot of the source volcano. **(L)** A wider view of 12-P4 showing surface coverage. Backpack for scale.

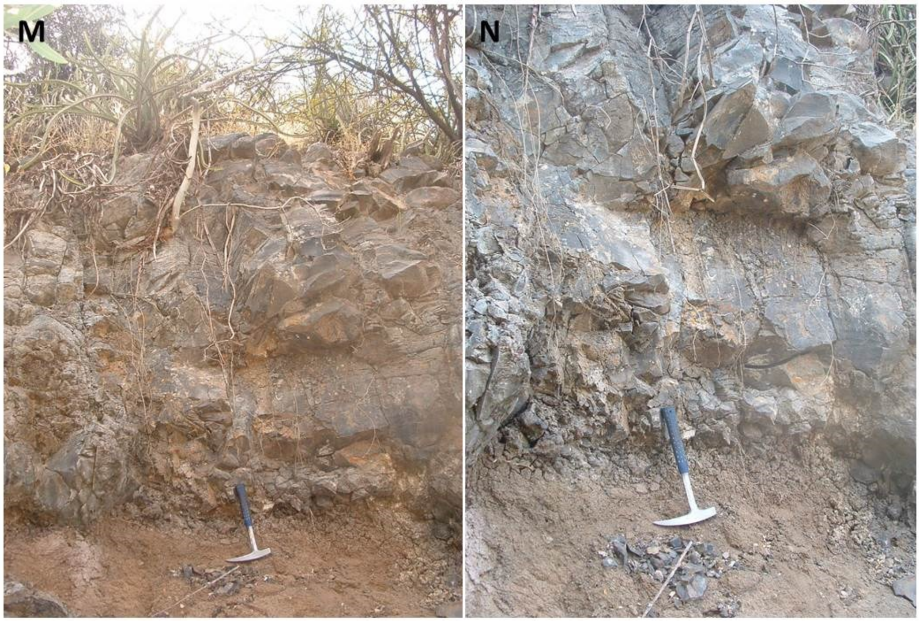

Figure 20b. Field photographs of 12-P3 near the theorized Humbu source volcano. **(M)** 12-P3 as exposed on upper slopes of the source volcano. Rock hammer for scale. **(N)** Detail on the 12-P3 outcrop.

3.2 Laboratory methods

3.2.1 X-ray Fluorescence (XRF)

To determine the bulk geochemical composition for rocks from both areas, samples were prepared for X-ray Fluorescence (XRF) analysis. Lava samples were broken down using a sledgehammer, whereas tuffaceous samples were crushed in mortar and pestle. About 10g of unweathered sample was further crushed in a Jawcrusher and finely powdered in a tungsten carbide shatterbox for four minutes to reach a silt-sized fraction. Powdered samples were coned and quartered to ensure a representative sample. Each sample was dried overnight in an oven at 105°C.

Loss on ignition (LOI) was performed on a precisely weighed subsample (~1g) of each sample to determine the amount of water and other volatiles lost during the fusion process. This involved placing a known weight of sample into a crucible, weighing it on a balance, placing the crucible and sample into a Thermolyne muffle furnace for fifteen minutes at 1050°C, cooling it in a desiccator, and finally weighing the material and crucible after ignition. The calculated LOI value is used for XRF corrections and to assess the degree of alteration.

For fusion, 1.000 g of each sample was weighed using an analytical balance, combined with 10.000 g of a 50:50 ratio of lithium metaborate/tetraborate flux with an integrated LiBr nonwetting agent and ~1 g of an ammonium nitrate oxidizer, and fused into a glass bead using a pre-programed routine on a Claisse M4 Fluxer with a maximum temperature of ~1050°C. These beads were then analyzed using a Bruker S4 Pioneer Wavelength Dispersive XRF spectrometer. A calibration curve made up of eleven USGS igneous and sedimentary rock standards was used, previously created using the same methods as the unknowns (McHenry, 2009). Major elements (SiO_2, TiO_2, Fe_2O_3, MgO, MnO, Na_2O, CaO, K_2O, and P_2O_5) were analyzed along with some minor and trace elements (Y, Nb, V, Zn, Ni, Cr, Sr, and Ba). Only those values that met or exceeded twice the calculated Lower Limit of Detection (LLD) with analytical errors of less than 12% (for trace elements) are reported. Microsoft Excel was used for data manipulation, and IgPet 2010 was used for data plotting.

3.2.2 X-ray Diffraction (XRD)

To determine the degree of alteration, samples from Embagai were analyzed for LOI and prepared for X-ray Diffraction (XRD) following the methods of McHenry (2009). A split of the samples powdered for XRF analysis (methods as above) was ground to a finer grain size using a McCrone micronizing mill. These samples were air dried and mounted as random powders for XRD. Samples were analyzed using a Bruker D8 Focus XRD (CuKα tube, 1 s per 0.02° 2θ, over the range 2-60 2θ, Sol-X energy dispersive detector) with the XRD Commander program, and results analyzed using Bruker's EVA program. Diffraction patterns were matched against the International Center for Diffraction Data (ICDD) Powder Diffraction File (PDF 2) for phase identification.

3.2.3 Electron Probe Microanalysis (EPMA)

Polished petrographic thin sections of nine Embagai samples (EM01, 02, 03, 05, 06, 08, 11, 12, and 13) were prepared at Spectrum Petrographics and analyzed using a petrographic microscope. Images were taken using a microscope-mounted camera and captured with MagnaFire.

For analysis of phenocryst compositions, four (EM02, 03, 06, and 11) of the nine polished thin sections were selected for electron probe microanalysis (EPMA). These were supplemented by grain mounts of target minerals (e.g. feldspar, augite, titanomagnetite, perovskite) for samples EM04, 07, 09, 10, 14, and 15. Grain mounts were prepared following the methods of McHenry (2005), which involved gently crushing a sample to a sand-sized fraction, sieving into meshes of 40+ (greater than 0.42 mm), 40-60 (0.42 – 0.25 mm), and <60 (<0.25 mm). The 40-60 component was placed in a Teflon beaker and soaked for ~1 minute with 4% HF in a sonic bath. If the sample continued to effervesce after one minute of HF treatment, the sample was decanted, rinsed three times with deionized (DI) water, and treated with 10% HCl or HNO_3 until the effervescence stopped, then rinsed in DI water three more times. This process was repeated until there was no sign of effervescence. Samples were then poured into a ceramic drying dish and dried under a heat lamp. The HF-treated fraction was then hand-picked for grain mounts under a microscope. The mounts themselves were flat cylinders of plastic that were drilled with 10-15 holes. Each drill hole held one sample's phenocrysts, including augite, feldspar, hornblende, micas, titanomagnetite/ilmenite (oxides), and perovskite. Phenocrysts were mounted to a taped surface and covered in epoxy. After the epoxy set, the mounts were polished and photographed for reference.

Thin sections and grain mounts were carbon coated to prevent charging of the samples and analyzed using a Cameca SX51 electron microprobe at the University of Wisconsin-Madison following the methods of McHenry et al. (2008). Energy dispersive spectrometry (EDS) was used to identify minerals and determine what elements needed to be measured using wavelength dispersive spectrometry (WDS). Elements measured include SiO_2, TiO_2, Fe_2O_3, Al_2O_3, MnO, MgO, CaO, Na_2O, and K_2O. High-quality results were obtained for: 79 augites (pyroxenes), 8 feldspars, 47 nephelines ($(Na,K)AlSiO_4$), 37 oxides (titanomagnetites or ilmenites), 9 biotites, 15 titanian andradite garnets (melanite or schorlomite: $(Ca_3(Ti,Fe^{3+})_2((Si,Fe^{3+})O_4)_3)$, 9 perovskites ($CaTiO_3$), and 9 sphenes ($CaTiSiO_5$, titanite). Individual phenocryst compositions for Embagai are reported in **Appendices A-G**.

Augite, biotite, andradite, perovskite, and sphene phenocrysts were measured at 20 nA, 15 kV, and a 5 micron beam. Feldspar and nepheline phenocrysts were analyzed at 10 nA, 15 kV, and a 5 micron beam. Oxides were analyzed at 20 nA, 15 kV, and a focused beam (though oxides from Bed III were analyzed at 10 mA, 15 kV, and a focused beam). Data from this thesis and comparisons was plotted using the RockWare IgPet program.

3.2.4 Paleomagnetic methods

Samples 10-T21 (Hajaro or Wa Mbugu) and 10-T25 (definitive Wa Mbugu) were each drilled to create two 1” inch cores. Each core was cut in half to allow for duplicate measurements. Cores were reoriented using a Pomeroy orienting device with sun compass. Orientation measurements are given in **Appendix H.**

Paleomagnetic demagnetization was performed with an ASC TD-48 Thermal Specimen Demagnetizer and a Schonstedt Model GSD-1 alternating field (AF) demagnetizer**.** AF demagnetization was carried out in steps between 2.5 mT and 100 mT (peak alternating field).

Thermal demagnetization was carried out in 100°C steps between 100°C and 500°C. It should be noted that one set of heating elements in the oven was disabled, thus the temperatures that the samples experienced were slightly different from the set point. At low set points, actual temperature was very close to the set point. This was tested at 149°C (actual temperature). The temperature discrepancy increased with increasing set point. At a set point of approximately 490-500°C, the actual temperature was 538°C. These temperature discrepancies do not change the interpretation of the results.

During thermal demagnetization, samples 10-T21-1 and 10-T25-1 fractured into two or more pieces at temperatures of 400-500°C, perhaps due to pressure build-up from dehydration or water release of zeolitic material. The specimens were pieced back together using potassium silicate, and measurements were continued.

Magnetization was measured on a Molspin Minispin magnetometer using the Molmac program provided by Jeff Gee. The MacPaleomag2.1 program, also provided by Gee, was used to plot data and to calculate the best-fit principal component direction and the maximum angular deviation (MAD) (Kirschvink, 1980). A declination (dec) of ~0°/360° generally represents normal polarity whereas ~180° represents reverse polarity. The angle from the horizontal plane is the inclination (inc), measured +90° for straight down to -90° for straight up (Tauxe, 1998).

Susceptibility as a function of temperature, $\chi(T)$, was measured to constrain Curie temperatures (T_C), the temperature above which a mineral loses its ferromagnetic behavior. Measurement of the Curie temperature aids in identification of predominant magnetic minerals. The two most common magnetic oxides have very well-defined T_C:

magnetite at 580°C and hematite at 680°C (Petersen and Bleil, 1982), though Ti substitution will lower the T_C (Tauxe, 2014). A small amount of sample was powdered using a shatterbox to coarse sand size and then placed into a quartz tube and placed in the furnace attachment of an AGICO MFK1-FA Multi-Function Kappabridge. The sample was heated at a constant rate (11.8°C min^{-1}) from 40°C to 600 or 700°C and back to 40°C. Measurements were taken approximately every 20 seconds.

At the point that a sample reaches and exceeds T_C, the sample loses its ferromagnetism, and as a result magnetic susceptibility will decrease abruptly. T_C may be identified by the inflection point in the $\chi(T)$ curve, and a peak in the first derivative of the $\chi(T)$ curve was thus taken to estimate the T_C of the sample (Fabian et al, 2013). Depending on the magnetic mineralogy of the sample, new magnetic minerals may begin to form or destruct at any time and these changes may also be represented as inflections in the susceptibility curve. The program CurveEval 6 was used to evaluate these curves.

4. RESULTS: EMBAGAI

4.1 Bulk geochemical composition

Most Embagai lava samples had high loss on ignition values, indicating alteration. The presence of calcite and/or zeolites in a majority of the collected samples is consistent with high LOI values and lower concentrations of Si, which is being diluted. Thus, only samples with LOIs of less than 7% are used for the bulk geochemical plots (**Tables 2.1** and **2.2**). Two samples representing the caldera floor (EM01) and western flank (EM05) plot within the foidite region of a Total Alkali-Silica diagram (**Figure 21**, after Le Bas et al., 1986). The second caldera floor sample (EM06) and eastern rim (T32) plot within the tephri-phonolite field. One northern rim sample (EM12) plots as phono-tephrite, whereas a second (EM15) is tephrite or basanite. Of all of the sampled areas, the caldera floor samples were the most geochemically consistent.

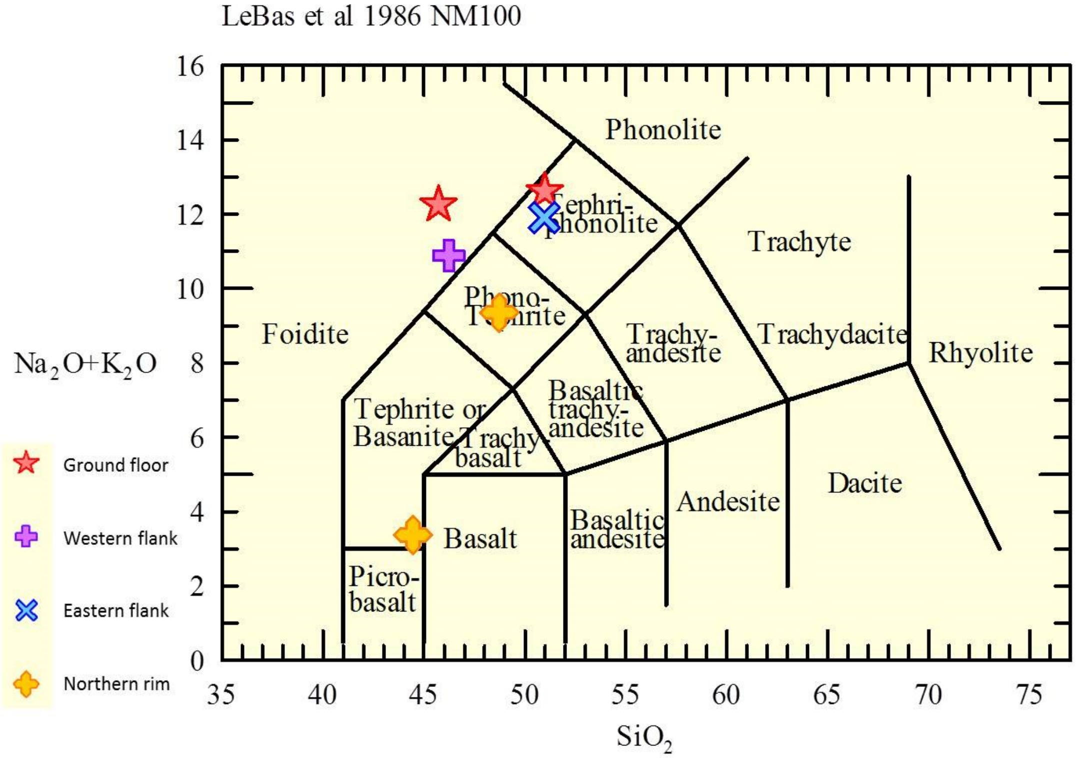

Figure 21. Total Alkali versus Silica classification after Le Bas et al. (1986) for the least altered (LOI < 7%) Embagai samples. Most samples plot in the foidite (nephelinite/melilitite) region, with some tephra-phonolite, phono-tephrite, and tephrite.

Sample	SiO2	Al2O3	Fe2O3	TiO2	MgO	MnO	CaO	K2O	Na2O	P2O5	LOI	TOTAL
12EM01	43.45	14.30	11.93	2.45	3.08	0.34	8.28	4.80	6.84	0.74	2.95	**99.62**
12EM03	38.87	9.82	13.94	2.02	1.91	0.48	13.01	5.13	2.13	0.44	11.56	**100.04**
12EM04	37.62	9.49	13.82	1.99	1.87	0.48	13.54	5.29	3.00	0.36	11.11	**99.33**
12EM05	42.62	12.82	13.03	2.12	2.34	0.43	9.44	5.49	4.54	0.64	5.18	**99.11**
12EM06	47.24	18.17	8.41	1.75	1.05	0.18	4.66	3.17	8.51	0.35	6.06	**99.99**
12EM07	33.04	7.96	9.19	1.52	1.51	0.35	21.74	4.97	0.98	0.43	18.97	**101.26**
12EM08	45.82	11.65	12.82	2.07	2.08	0.43	8.90	2.91	4.40	0.45	7.54	**100.11**
12EM09	48.61	17.51	9.35	1.63	2.09	0.27	7.48	1.40	2.68	0.99	7.62	**100.01**
12EM10	25.76	8.95	7.71	1.10	1.32	0.37	27.72	3.11	0.72	1.30	21.08	**100.97**
12EM11	42.36	16.05	9.72	2.51	2.12	0.30	11.16	1.73	5.58	0.71	7.41	**100.20**
12EM12	45.33	15.82	9.69	2.51	2.30	0.28	8.54	2.92	5.78	0.83	4.71	**99.66**
12EM13	25.77	8.88	5.78	0.70	1.12	0.27	28.46	2.97	0.57	0.94	22.68	**100.96**
12EM14	48.87	14.17	11.63	1.50	2.26	0.37	8.35	1.66	2.35	1.05	7.15	**99.63**
12EM15	40.08	16.05	17.16	3.19	3.42	0.44	7.46	2.02	1.02	1.02	6.71	**98.96**
LM13-T32	48.66	17.21	9.06	2.28	2.08	0.19	5.03	5.31	6.06	0.53	1.69	**98.51**

Table 2.1. Embagai X-Ray Fluorescence major element compositions. EM02 was removed since it was mostly calcite, and our calibration is based on silicates and thus not reliable for this kind of sample. Values are in wt. %. LOI values are included in the totals.

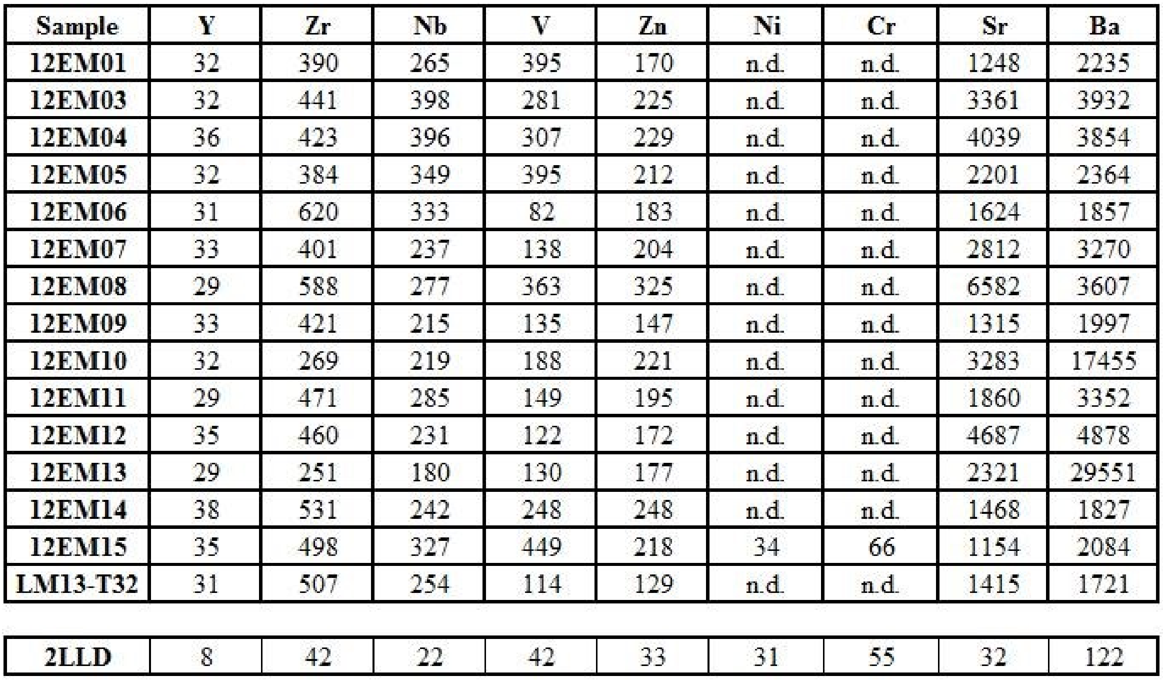

Sample	Y	Zr	Nb	V	Zn	Ni	Cr	Sr	Ba
12EM01	32	390	265	395	170	n.d.	n.d.	1248	2235
12EM03	32	441	398	281	225	n.d.	n.d.	3361	3932
12EM04	36	423	396	307	229	n.d.	n.d.	4039	3854
12EM05	32	384	349	395	212	n.d.	n.d.	2201	2364
12EM06	31	620	333	82	183	n.d.	n.d.	1624	1857
12EM07	33	401	237	138	204	n.d.	n.d.	2812	3270
12EM08	29	588	277	363	325	n.d.	n.d.	6582	3607
12EM09	33	421	215	135	147	n.d.	n.d.	1315	1997
12EM10	32	269	219	188	221	n.d.	n.d.	3283	17455
12EM11	29	471	285	149	195	n.d.	n.d.	1860	3352
12EM12	35	460	231	122	172	n.d.	n.d.	4687	4878
12EM13	29	251	180	130	177	n.d.	n.d.	2321	29551
12EM14	38	531	242	248	248	n.d.	n.d.	1468	1827
12EM15	35	498	327	449	218	34	66	1154	2084
LM13-T32	31	507	254	114	129	n.d.	n.d.	1415	1721
2LLD	8	42	22	42	33	31	55	32	122

Table 2.2. Embagai X-Ray Fluorescence minor element compositions. Values are in parts per million (PPM). Only values that met or exceeded twice the Lower Limit of Detection (LLD) are reported.

Major elements (AlO_2, Fe_2O_3, TiO_2, CaO, MgO, and NaO_2) were plotted against SiO_2 for the seven least altered Embagai samples to show large-scale trends between them (**Figure 22**). Of note is a strong negative trend when plotting SiO_2 vs. Fe_2O_3, indicating high iron concentration in samples with lower Si. Figures 19 A and F show increases in both Al and Na with respect to Si. Figures 19 C and E show decreases in Ti and Mg with an increase in Si.

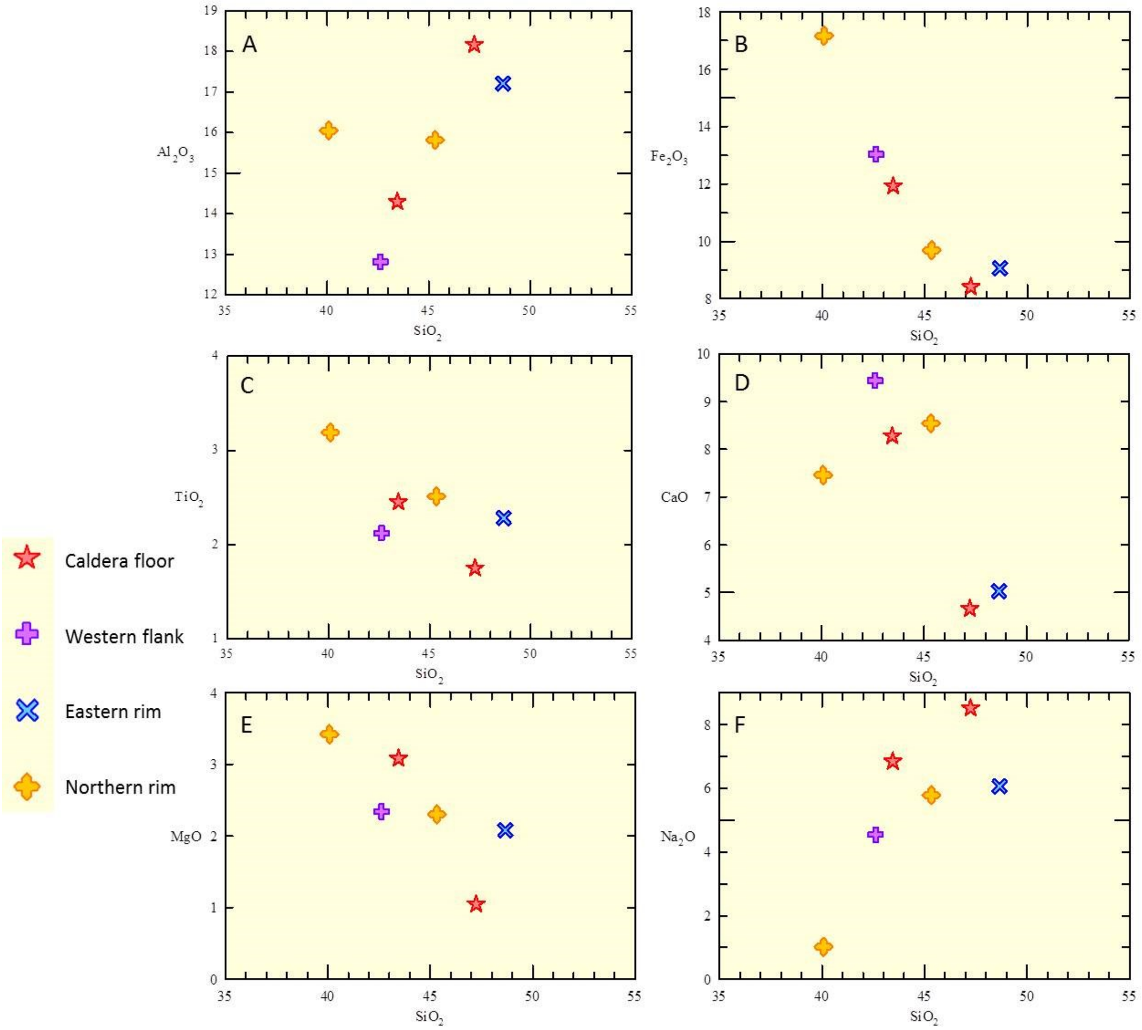

Figure 22. Plots of major elements vs. SiO_2 for the least altered Embagai samples. **(A)** SiO_2 vs. AlO_2, **(B)** SiO_2 vs. Fe_2O_3 shows a strong negative trend, indicating that iron is more concentrated in the lower-Si samples, **(C)** SiO_2 vs. TiO_2, no discernable trend, **(D)** SiO_2 vs. CaO shows a negative trend, largely due to the addition of calcite, **(E)** SiO_2 vs. MgO shows a slight negative trend similar to iron, and **(F)** SiO_2 vs. NaO_2 shows a positive trend.

4.2 Mineral assemblages

The occurrence of minerals determined using XRD and electron microprobe observations is given in **Tables 3.1** (primary) and **3.2** (secondary). XRD analysis of the sixteen samples confirms that samples with high LOI values have abundant zeolites or calcite. Samples dominated by zeolites or calcite were EM02, 03, 05, 07, 10, 11, and 13. Examples of zeolites identified include analcime ($Na_2(Al_2Si_4O_{12})\cdot 2H_2O$), phillipsite ($(Na,K,Ca_{0.5},Ba_{0.5})_{4\text{-}7}[Al_{4\text{-}7}Si_{12\text{-}9}O_{32}]\cdot 12H_2O$), and chabazite (including Na-rich chabazite: $(Na_2,K_2,Ca,Sr,Mg)_2[Al_2Si_4O_{12}]_2\cdot 12H_2O$). Samples EM04, 06, 08, 14, and 15 had abundant zeolites along with the primary minerals. Samples EM01, 09, 12, and 13-T32 were relatively unaffected by zeolitization, containing mostly primary magmatic minerals.

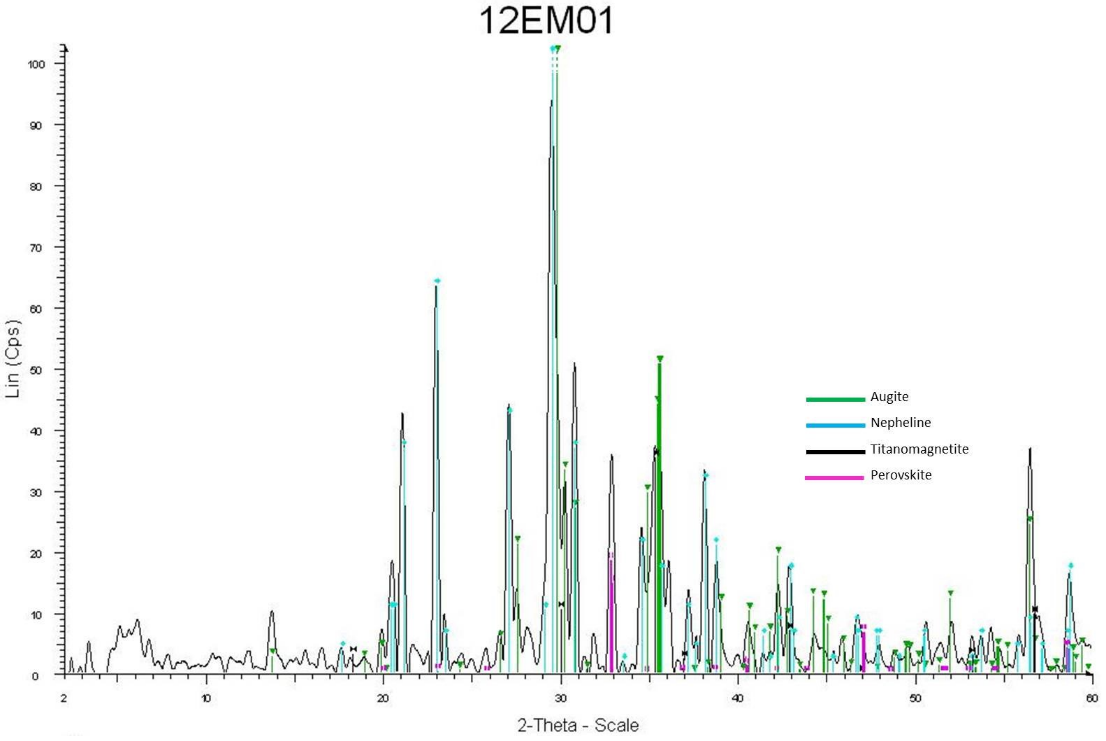

Figure 23. Example of Embagai nephelinite diffraction pattern, for sample EM01. The pattern is smoothed and background subtracted. The primary mineral assemblage includes nepheline and augite, with titanomagnetite and perovskite.

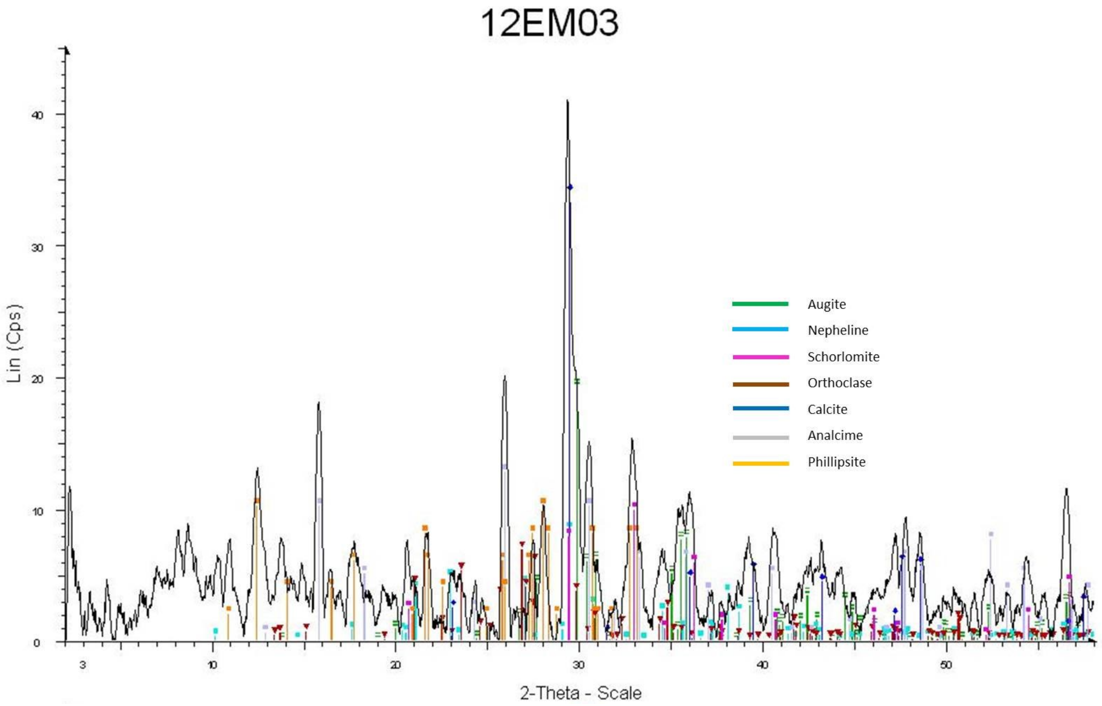

Figure 24. Example of Embagai zeolite diffraction pattern, for sample EM03. The pattern is smoothed and background subtracted. The primary mineral assemblage includes nepheline and augite, with schorlomite (andradite) garnet. The secondary mineral assemblage includes orthoclase (K-feldspar), calcite, and the zeolite minerals analcime and phillipsite.

Primary magmatic minerals that appeared throughout the samples include nepheline, K-feldspar ($KAlSi_3O_8$), anorthite, various augites, and the garnets andradite and schorlomite. Titanian andradite and schorlomite are of note as they are found exclusively in alkaline igneous rocks such as phonolites, nephelinites, and ijolites (Deer et al., 1992). There is also rare amphibole, melilite, mica (biotite or muscovite), perovskite ($CaTiO_3$), and ilmenite. Sodalite ($Na_8(Al_6Si_6O_{24})Cl_2$) was present in two samples.

Sample	Location	Nepheline	Augite	Sphene (Titanite)	Plagioclase	Titanomagnetite	Perovskite	Andradite garnet	Schorlomite garnet	Melilite (Gehlenite)	Sodalite	Biotite	Muscovite	Quartz	LOI
12EM01	Floor	xxx	xxx			xx	xx								2.95
12EM06	Floor	xxx	xx	○		○					+	○			6.06
13-T32	East	xxx	xxx	○		x									1.69
12EM08	East	xx	xxx										+		7.54
12EM09	East	xx	xxx	xx			x			+				+	7.62
12EM07	East													x	18.97
12EM05	West	xxx	xx												5.18
12EM04	West	xxx	x		x				xx						11.11
12EM03	West	○	○				○		+						11.56
12EM02	West		○			○								+	39.27
12EM12	North	xxx	xxx				xx			x					4.71
12EM15	North		xxx			○	○	x	○				+		6.71
12EM14	North		xxx	x			xxx								7.05
12EM11	North	xxx	xxx	○	x	○		○			x				7.41
12EM10	North			○			○	○	○			○			21.08
12EM13	North		x												22.67

Table 3.1. Primary mineral assemblages at Embagai sorted by sample location and LOI. Frequency symbols: xxx = abundant, xx = common, x = between rare and common, + = rare, - = absent, ○ = identified by electron microprobe but not observed by XRD.

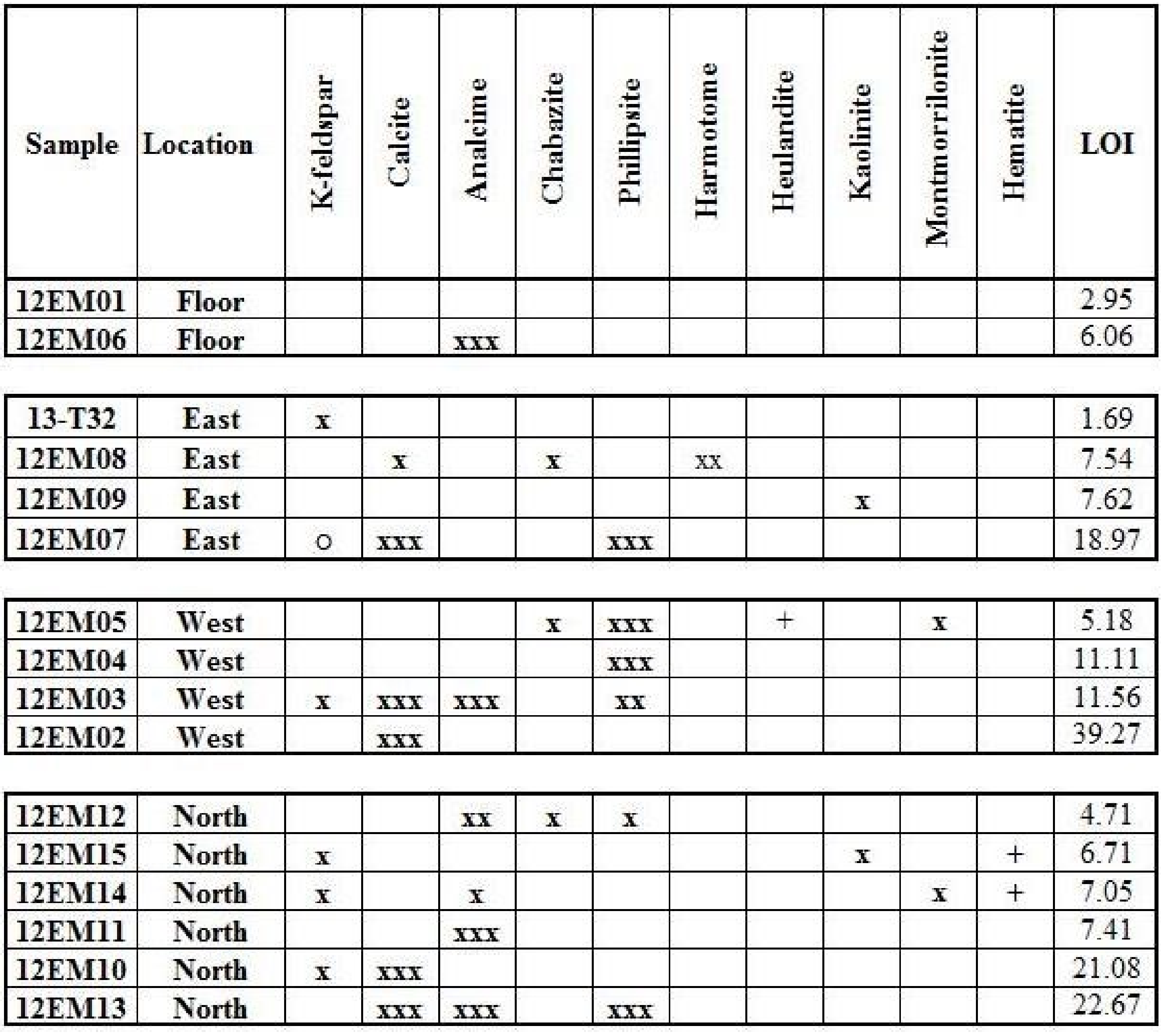

Sample	Location	K-feldspar	Calcite	Analcime	Chabazite	Phillipsite	Harmotome	Heulandite	Kaolinite	Montmorrilonite	Hematite	LOI
12EM01	Floor											2.95
12EM06	Floor			xxx								6.06
13-T32	East	x										1.69
12EM08	East		x		x		xx					7.54
12EM09	East								x			7.62
12EM07	East	○	xxx			xxx						18.97
12EM05	West				x	xxx		+		x		5.18
12EM04	West					xxx						11.11
12EM03	West	x	xxx	xxx		xx						11.56
12EM02	West		xxx									39.27
12EM12	North			xx	x	x						4.71
12EM15	North	x							x		+	6.71
12EM14	North	x		x						x	+	7.05
12EM11	North			xxx								7.41
12EM10	North	x	xxx									21.08
12EM13	North		xxx	xxx		xxx						22.67

Table 3.2. Secondary mineral assemblages at Embagai sorted by sample location and LOI. Frequency symbols: xxx = abundant, xx = common, x = between rare and common, + = rare, - = absent, ○ = identified by electron microprobe but not observed by XRD.

The mineral assemblages from the Embagai samples (**Tables 3.1** and **3.2**) were compiled to compare the degree of alteration between samples. EM02, 07, 10, and 13 had the highest LOIs (>10%). Calcite was dominant in these samples with high LOIs, as CO_2 is lost during ignition. Analcime was also a major mineral in altered samples, though it also appeared in relatively fresh samples. Phillipsite was abundant in samples from the western flank and some from the northern rim. K-feldspar was observed in most northern rim samples and two of the eastern rim samples. EM07 contained K-feldspar, as observed by microprobe. The K-feldspars in these samples is potentially authigenic, the result of phillipsite alteration (McHenry, 2009). 13-T32 is one of the least altered samples, thus its K-feldspar (as detected by XRD) is most likely magmatic. Some clay minerals were present, mostly in samples from the northern rim and the western flank.

Analysis of thin sections combined with the XRD results helps characterize the overall mineralogical abundances and assemblages. Four (EM02, 03, 06, and 11) of the polished thin sections were selected for electron probe microanalysis (EPMA).

The minerals observed in thin sections EM01 and 06 (**Figures 25 and 26**), both representing the caldera floor, are consistent with the XRD results. In thin section, both display euhedral nepheline crystals as the dominant phenocrysts. Samples EM01 and 06 also display elongated minerals with strong 2nd order birefringence (blue-red) consistent with pyroxene. EM06 contains analcime, identified in thin section and by XRD. In thin section, analcime is roughly euhedral and spheroidal. Rare amphibole occurs in eastern rim sample EM08 (**Figure 27**), displaying well developed cleavage planes and zoning. Additional second-order red-violet-blue clinopyroxenes also appear in this sample.

The minerals observed in the EM02 thin section are also consistent with the XRD data, dominated by highly birefringent calcite (**Figure 28**).

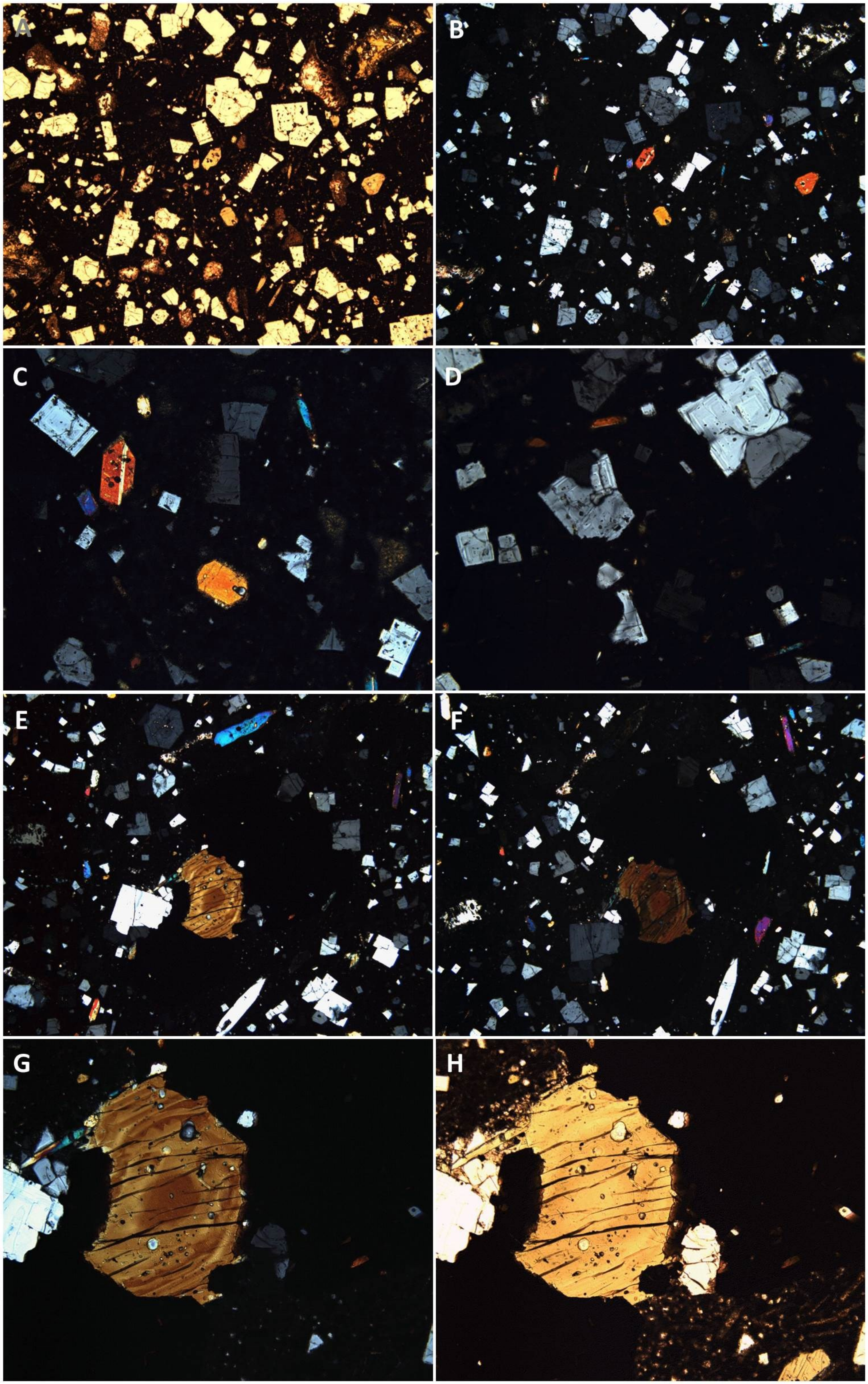
A
B
C
D
E
F
G
H

Figure 25, previous page. Thin section of caldera floor sample EM01. A 4X objective was used for images A, B, E and F. A 10X objective was used for images C, D, G, and H. Crystals average 1 mm across. **(A)** Plane polarized view (PPL) of general mineralogic texture. **(B)** Cross-polarized (XPL) version of view (A). Phenocrysts are dominated by euhedral crystals of nepheline (first order gray) with occasional first-second order red-orange clinopyroxenes. **(C)** Detail on (B) of nepheline and clinopyroxene minerals. Note the zoning within the nepheline. **(D)** XPL view of fractured nephelines that display hopper-like growth, indicating fast growth. **(E)** CPL view of possible clinopyroxene displaying undulose extinction. **(F)** Same view as (E) but rotated to show extinction. **(G)** Detail on (E) showing a bullseye pattern. **(H)** PPL view of (G). Color is light brown, consistent with clinopyroxene.

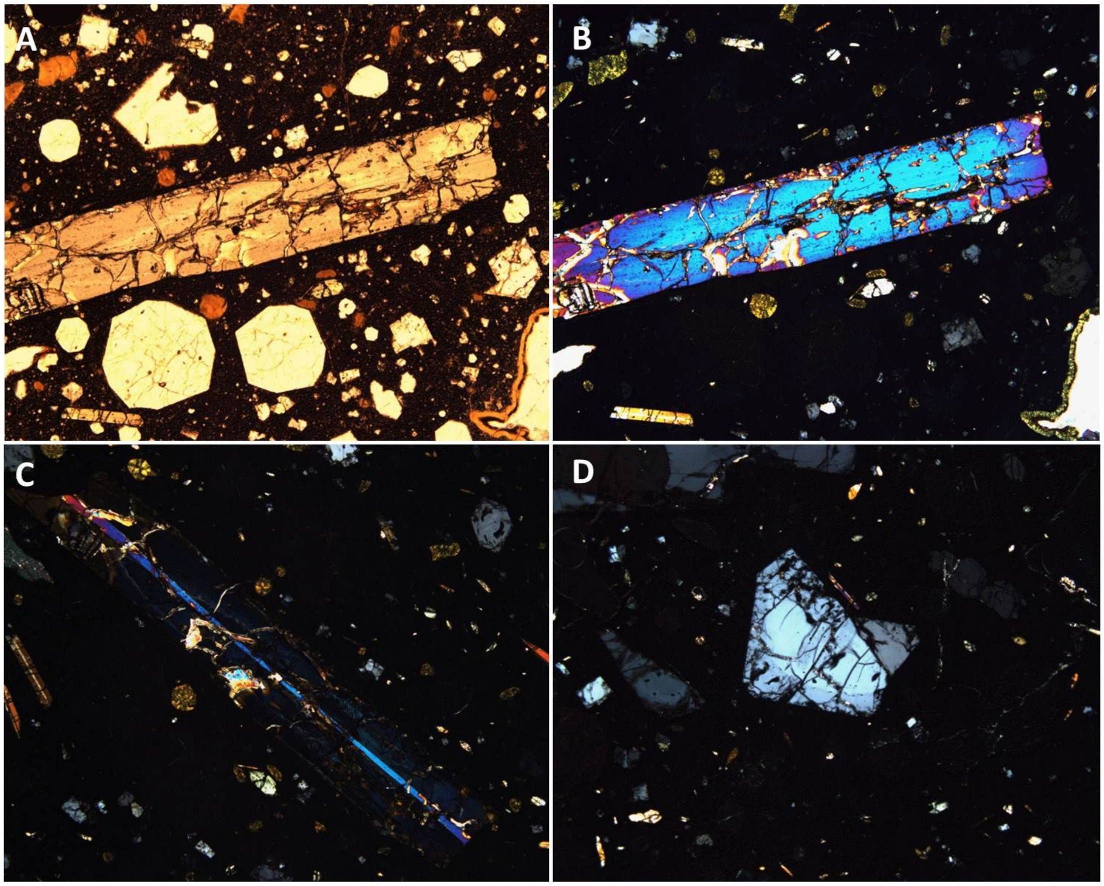

Figure 26. Thin section of caldera floor sample EM06. Large crystals average 1 mm across. A 4X objective was used for images A, B and C. A 10X objective was used for image D. **(A)** PPL view of elongated clinopyroxene surrounded by nepheline and spheroidal analcime. The largest clinopyroxene is 3.5 mm long. **(B)** Same view in XPL. The clinopyroxene phenocryst displays high order birefringence (1st order blue). **(C)** The previous clinopyroxene under extinction, as shown in XPL. **(D)** XPL view of typical nepheline in this sample.

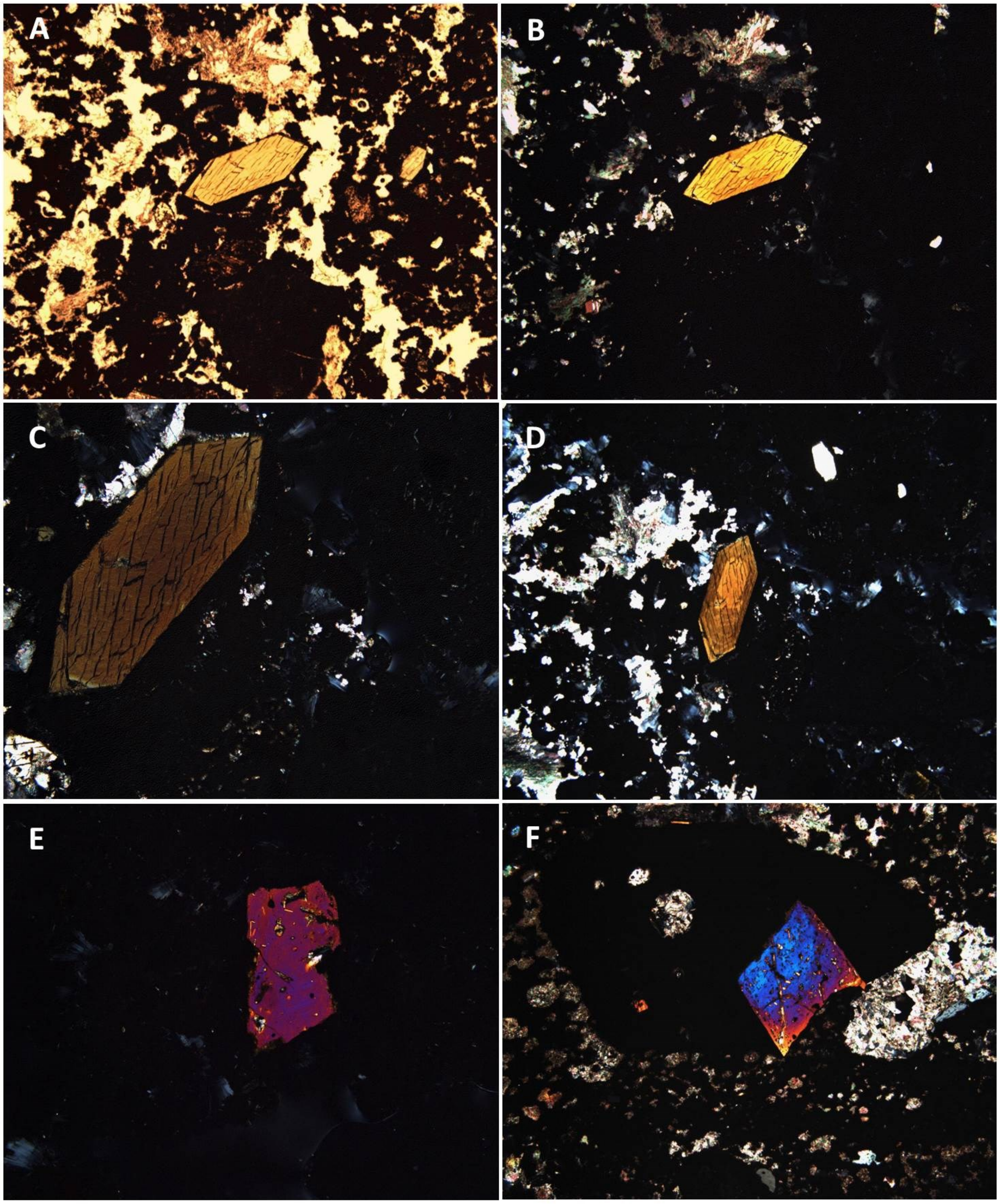

Figure 27. Thin section of eastern rim sample EM08. 4X objective used for images A, B, D, and F. A 10X objective was used for images C and E. **(A)** View in PPL of rare amphiboles. Large crystal measures 1 mm across. Note crystal zoning and diagnostic cleavage angles. The phenocryst is light brown in PPL. **(B)** Same view in XPL displaying second order yellow. **(C)** Detail of (B). The surface displays zoning and cleavage planes. **(D)** Another view of zoning texture and a second amphibole. **(E)** Likely clinopyroxene displaying second order red-violet. **(F)** Another clinopyroxene with first-second order blue to yellow.

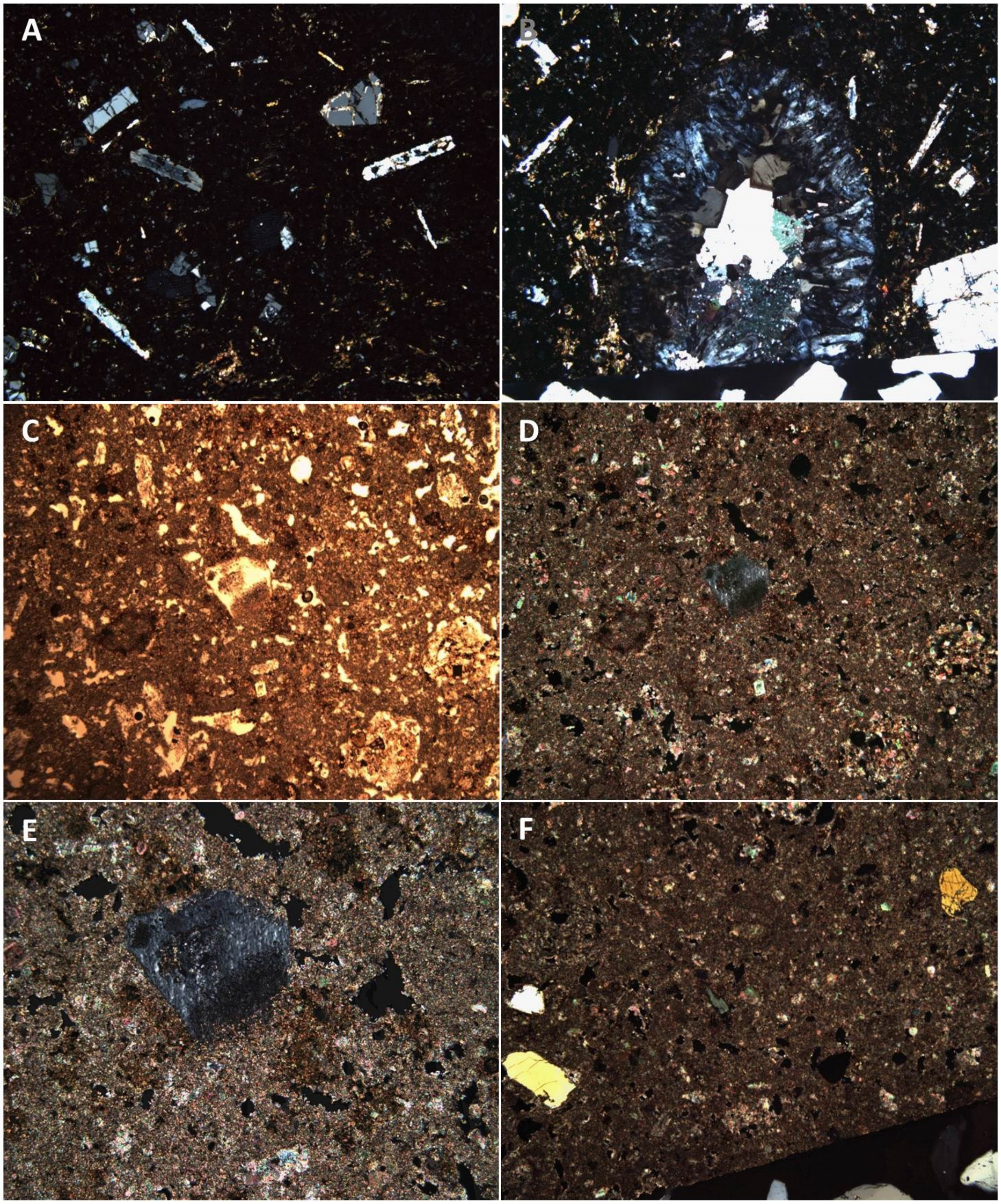

Figure 28. Thin sections of western rim samples EM05 (A-B) and EM02 (C-F). A 4X objective was used for all images except E, which uses 10x objective. **(A)** View in XPL of first order gray nephelines and first order gray elongated feldspar. **(B)** Crystal feature located on edge of sample. The core of the feature contains highly birefrigent calcite. Feature measures 2 mm across. **(C)** View in PPL of the general texture of the calcite-rich matrix. **(D)** Same view in XPL, displaying blue crystal form measuring 0.5 mm across. **(E)** Detail of (D). **(F)** Additional pyroxenes embedded in calcite-rich matrix.

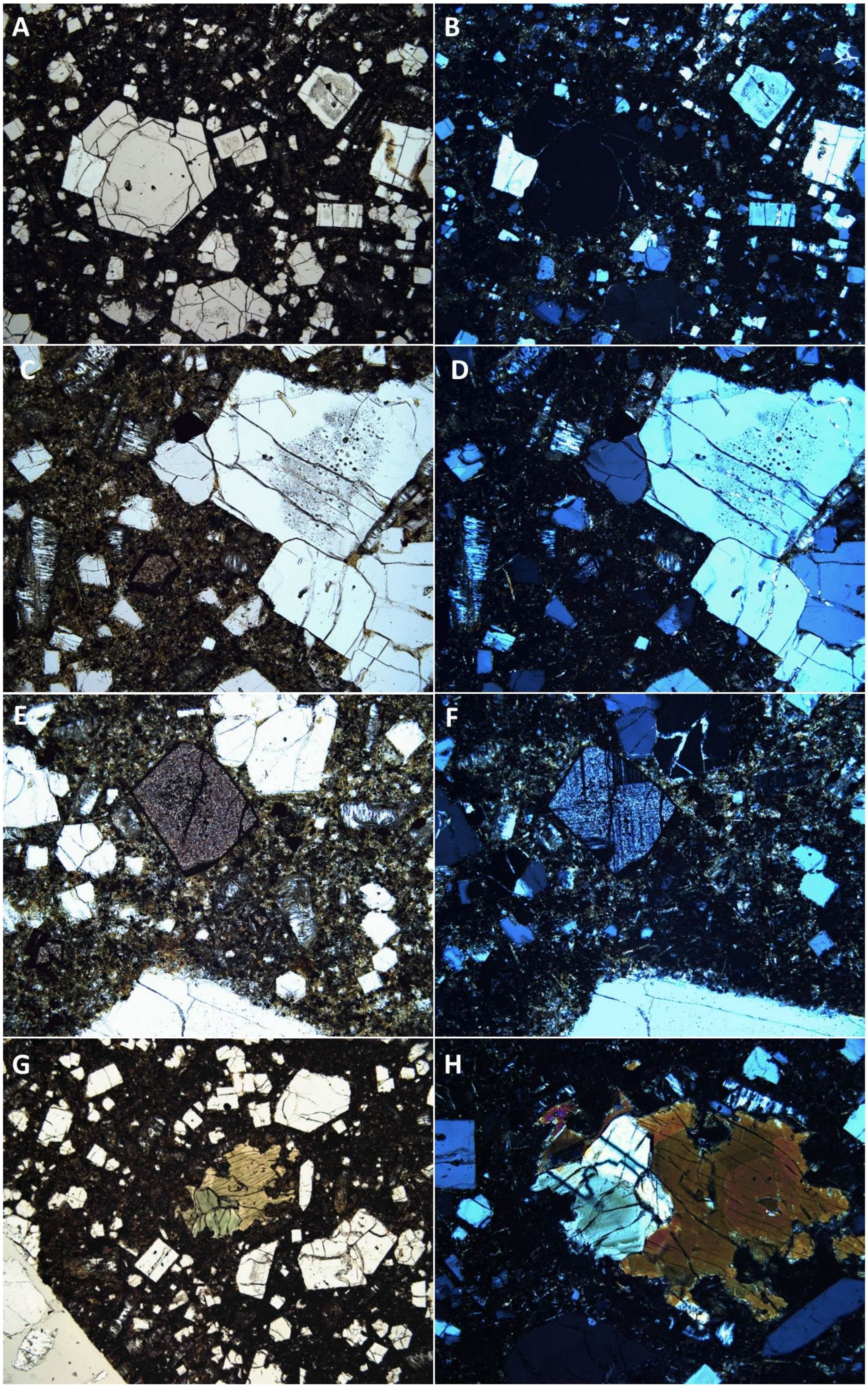
A
B
C
D
E
F
G
H

Figure 29, previous page**.** Thin sections of northern rim sample EM12. A 4X objective was used for images A, B and G. Images C-F and H used a 10x objective. **(A)** View in XPL of euhedral analcime and surrounding nephelines. **(B)** Same view as (A) in XPL. The euhedral grain is isotropic. **(C)** Nepheline crystals in PPL exhibiting porous and fibrous textures. **(D)** Same view as (C) in XPL. **(E)** High relief mineral in PPL. **(F)** Same view as (G) in XPL. **(G)** A possible anhedral amphibole is light green-brown in PPL, and **(H)** orange-brown in XPL with zoning.

Sample EM12 was dominated by nepheline and had moderate amounts of analcime. Porous and fibrous textures were noted in some of the nepheline grains. Rare amphibole was identified in the sample.

The bulk composition and mineral assemblages of the samples analyzed in this study confirm that Embagai is predominantly nephelinitic, since the fresher lavas consist predominately of nepheline and clinopyroxene (QAPF field 15c, foidite with nepheline, Le Maitre et al., 2002).

4.3 Phenocryst composition

Embagai augites (or other members of the clinopyroxene group) are highly variable in composition (**Table 4.1**). Most clinopyroxenes plot along the solid solution between iron and magnesium (FeO vs. MgO, **Figure 30a**). The majority of the Embagai augites contain between 1 and 3 wt% Na_2O, however a handful are higher than 3 wt% and are thus more omphacitic (**Figure 30b**, Deer et al., 1992). Embagai augites are not especially titanium-rich, with most between 0.5-2 wt.%, especially those from the caldera floor (Al_2O_3 vs. TiO_2, **Figure 30c**). When plotted on a FeO vs. MgO vs. CaO ternary plot (**Figure 30d**), Embagai augites from different locations continue to overlap and follow a similar FeO-MgO trend as in Figure 15a, though a few sodic augites are removed from the main trend.

Phenocryst	Location		Western flank	Western flank	Western flank	Caldera floor	Eastern rim	Eastern rim	Northern rim	Northern rim
	Sample		EM02	EM03	EM04	EM06	EM09	13-T32	EM11	EM15
Augite (pyroxene)	N		3	8	6	12	10	21	12	8
	wt% SiO_2	Average	48.68	50.71	51.66	51.48	51.27	51.13	50.56	49.05
		St Dev	2.17	1.73	0.84	0.27	1.15	1.06	0.43	2.57
	wt% Al_2O_3	Average	3.92	1.44	0.99	0.86	1.11	2.48	1.43	4.20
		St Dev	2.79	1.46	0.34	0.25	0.57	0.77	0.43	2.13
	wt% TiO_2	Average	1.68	1.46	1.36	1.28	0.66	1.65	1.33	2.08
		St Dev	0.86	0.55	0.71	0.19	0.20	0.51	0.58	0.80
	wt% FeO	Average	11.94	12.40	13.25	13.74	15.20	10.75	14.34	8.67
		St Dev	5.79	2.46	4.58	0.78	2.02	2.17	3.87	6.18
	wt% MnO	Average	0.35	0.54	0.37	0.55	0.49	0.36	0.51	0.13
		St Dev	0.29	0.28	0.07	0.06	0.07	0.10	0.14	0.11
	wt% MgO	Average	9.87	10.24	9.97	9.55	8.35	11.06	9.05	11.96
		St Dev	3.24	1.51	2.72	0.47	1.42	1.78	2.48	3.81
	wt% CaO	Average	21.92	20.98	19.92	20.69	20.03	21.25	21.64	21.96
		St Dev	2.87	1.52	4.50	0.40	1.08	1.23	1.78	6.10
	wt% NaO	Average	1.64	1.98	2.70	2.13	2.48	1.56	1.66	1.77
		St Dev	1.21	0.78	2.23	0.18	0.58	0.58	0.83	3.20
	wt% Total	Average	99.99	99.80	100.22	100.31	99.60	100.26	100.54	99.83
		St Dev	0.23	0.53	0.72	0.41	0.64	0.52	0.49	1.29

Table 4.1. Embagai augite composition averages and standard deviations, as measured by EPMA. N = number of grains analyzed.

Phenocryst	Location		Western flank	Eastern rim	Northern rim
	Sample		EM03	EM07	EM10
Feldspar	N		1	6	1
	wt% SiO_2	Average	64.47	64.22	65.36
		St Dev	-	1.71	-
	wt% Al_2O_3	Average	18.31	17.33	18.49
		St Dev	-	1.22	-
	wt% FeO	Average	0.98	1.42	0.37
		St Dev	-	1.14	-
	wt% CaO	Average	0.15	0.15	0.00
		St Dev	-	0.23	-
	wt% Na_2O	Average	1.12	0.59	0.69
		St Dev	-	0.33	-
	wt% K_2O	Average	14.19	14.41	15.04
		St Dev	-	1.13	-
	wt% BaO	Average	1.07	0.12	0.15
		St Dev	-	0.18	-
	wt% Total	Average	100.29	98.25	100.08
		St Dev	-	1.31	-

Table 4.2. Embagai feldspar averages and standard deviations, as measured by EPMA. Feldspars are K-rich. Note the higher Ba in western flank samples. Feldspars are more Fe-rich on the eastern rim.

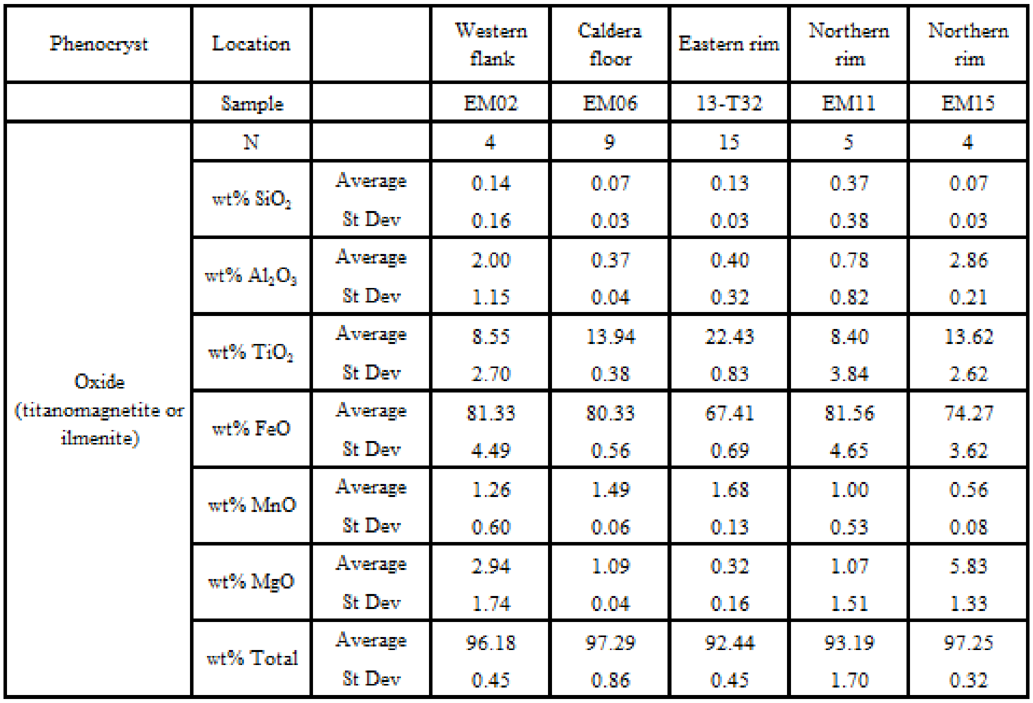

Phenocryst	Location		Western flank	Caldera floor	Eastern rim	Northern rim	Northern rim
	Sample		EM02	EM06	13-T32	EM11	EM15
Oxide (titanomagnetite or ilmenite)	N		4	9	15	5	4
	wt% SiO_2	Average	0.14	0.07	0.13	0.37	0.07
		St Dev	0.16	0.03	0.03	0.38	0.03
	wt% Al_2O_3	Average	2.00	0.37	0.40	0.78	2.86
		St Dev	1.15	0.04	0.32	0.82	0.21
	wt% TiO_2	Average	8.55	13.94	22.43	8.40	13.62
		St Dev	2.70	0.38	0.83	3.84	2.62
	wt% FeO	Average	81.33	80.33	67.41	81.56	74.27
		St Dev	4.49	0.56	0.69	4.65	3.62
	wt% MnO	Average	1.26	1.49	1.68	1.00	0.56
		St Dev	0.60	0.06	0.13	0.53	0.08
	wt% MgO	Average	2.94	1.09	0.32	1.07	5.83
		St Dev	1.74	0.04	0.16	1.51	1.33
	wt% Total	Average	96.18	97.29	92.44	93.19	97.25
		St Dev	0.45	0.86	0.45	1.70	0.32

Table 4.3. Embagai titanomagnetite/oxide averages and standard deviations, as measured by EPMA. Titanomagnetites are more titaniferous on the eastern rim.

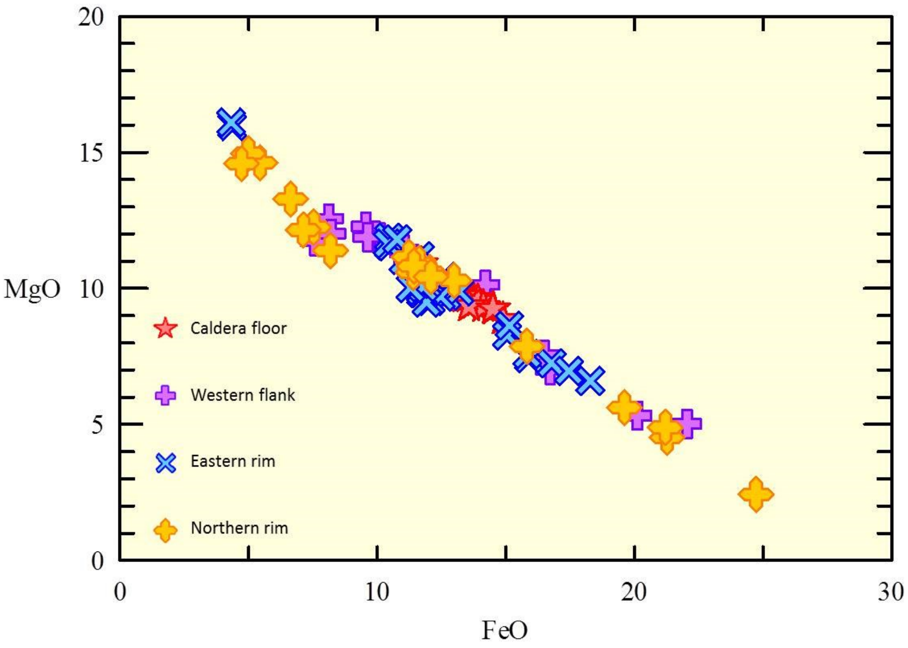

Figure 30a. Embagai augite phenocryst composition: FeO vs. MgO. Embagai augites are highly variable, plotting along the solid solution between Mg-rich and Fe-rich end members.

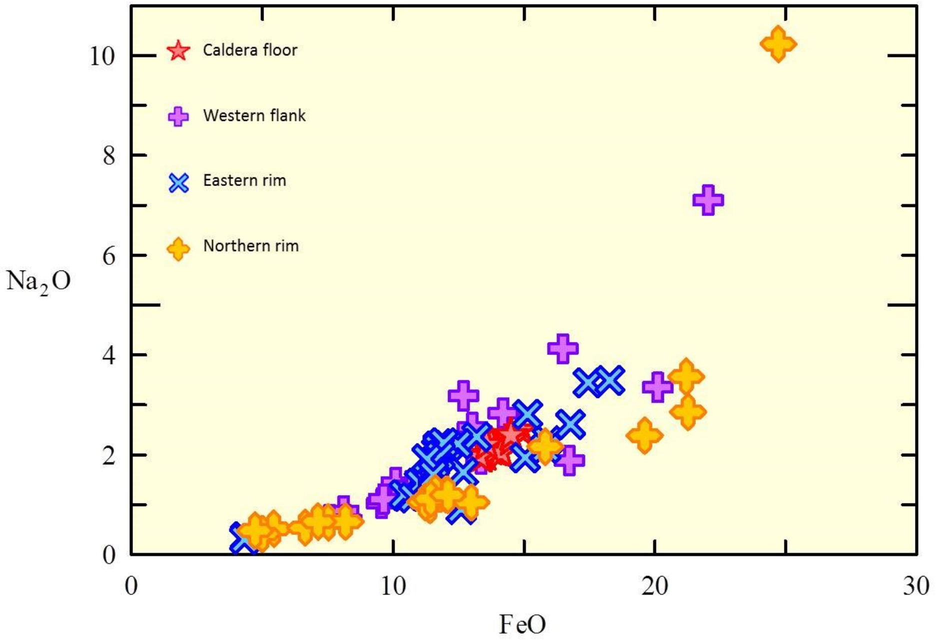

Figure 30b. Embagai augite phenocryst compositions: FeO vs. Na_2O. Most augites have sodium levels of 1-3 wt%. Those greater than 4 wt% may be omphacitic pyroxenes.

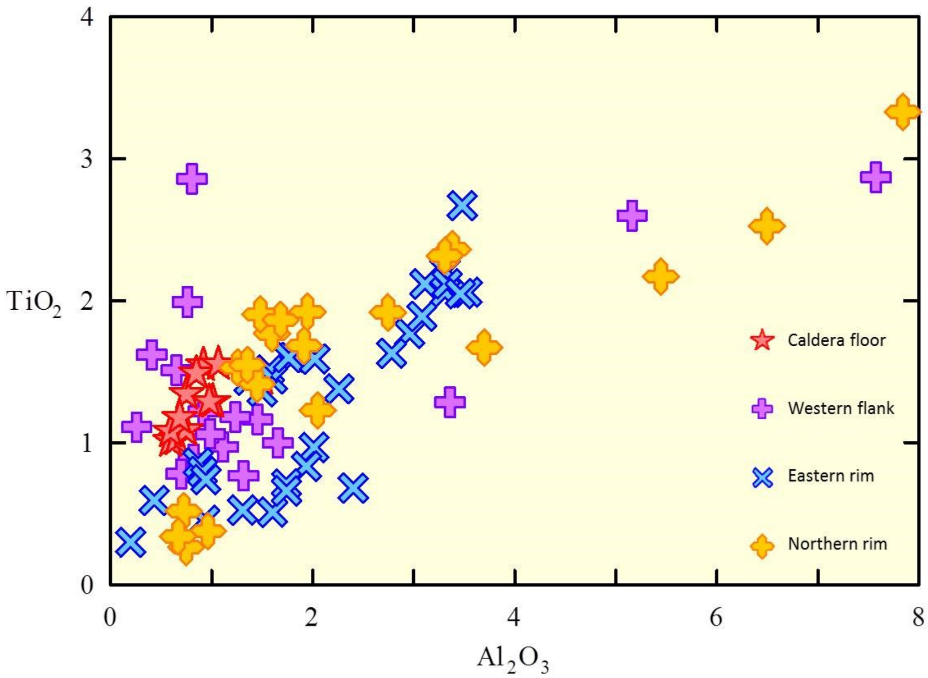

Figure 30c. Embagai augite phenocryst compositions: Al_2O_3 vs. TiO_2. All Embagai augites are below 3 wt% TiO_2, and thus not considered titanian augites. Most augites, especially those from the caldera floor, plot between 0.5-2 wt.% TiO_2.

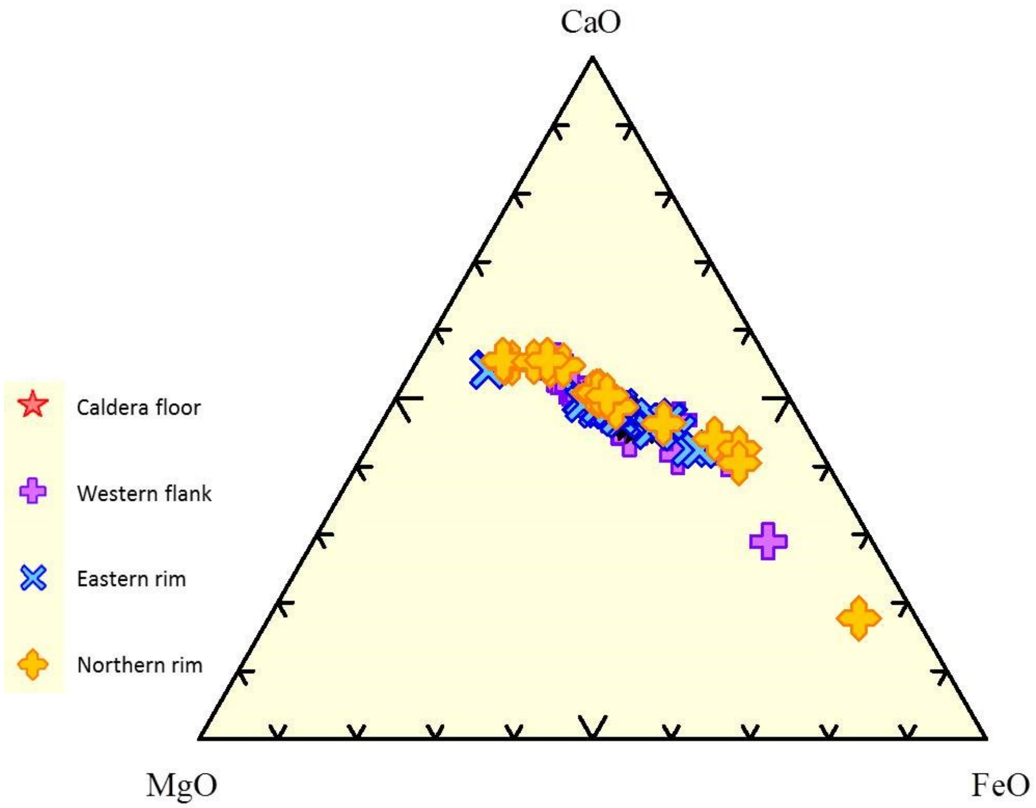

Figure 30d. Embagai augite phenocryst compositions: FeO vs. MgO vs. CaO ternary plot. All locations overlap. Augites continue to follow solid-solution series from MgO to FeO. Some of the most Fe-rich augites are sodic, explaining their offset from the main trend.

K-rich feldspars were observed in both heavily and less altered samples (**Figure 31, Table 4.2**), with LOIs ranging from 1.69 to 21.08%. K-rich feldspars were also identified by XRD in some samples. For the samples analyzed by microprobe, K-feldspar only appeared in highly altered samples (LOI 11.56%, 18.97%, and 21.08%). Based on this relationship, and the presence of the K-rich zeolite phillipsite in two of the three samples (**Table 3.2)**, it can be postulated that this K-feldspar is secondary, since authigenic K-feldspar can form from phillipsite under saline-alkaline conditions (e.g.

McHenry, 2010). The K-feldspar in the less altered sample 13-T32 is, however, likely primary.

Nepheline compositions overlap between different parts of Embagai, as observed in plots of Al_2O_3 and SiO_2 versus Na_2O (**Figure 32**), with the northern rim and caldera floor overlapping within the field of the eastern rim. The western flank was the most distinct of the Embagai samples in nepheline composition, with lower Na_2O and wider ranges of SiO_2 and Al_2O_3.

Oxides (titanomagnetite, ilmenite) within Embagai have well-defined populations depending on the collection site (**Figure 33, Table 4.3**). The caldera floor and eastern rim both have populations that cluster, whereas the western flank and northern rim have more variation in composition.

Andradite garnets have a trend of increasing TiO_2 with increasing Na_2O (**Figure 34**). Embagai garnets trend towards schorlomite (> 15 wt.% TiO_2, Deer et al., 1992) along the western flank and the northern rim.

Sphene (titanite) compositions are more variable (**Figure 35**), with some clustering of caldera floor and eastern rim sphenes. Sphenes were not identified in western flank samples.

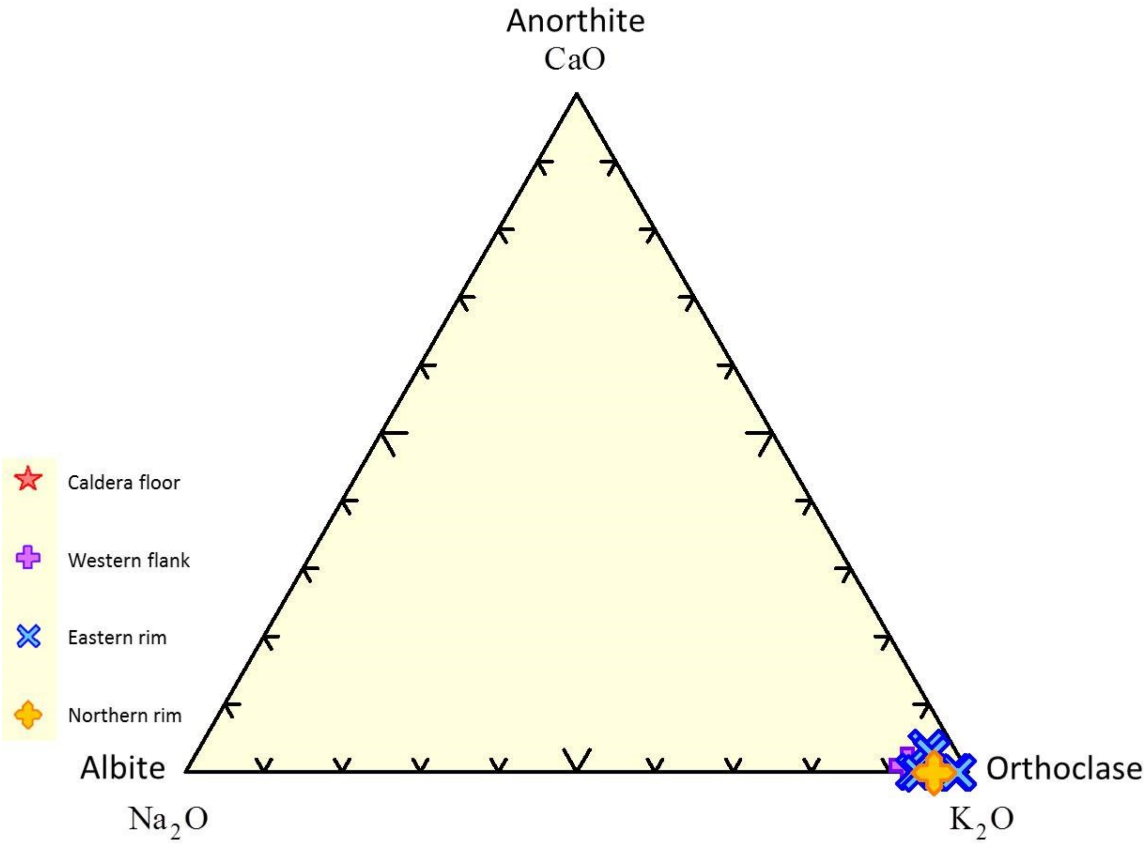

Figure 31. Ternary diagram of Embagai feldspars. Embagai feldspars are K-rich and rare, only preserved in three of the samples analyzed by microprobe (EM03, 07, 10; western flank, eastern rim, and northern rim respectively).

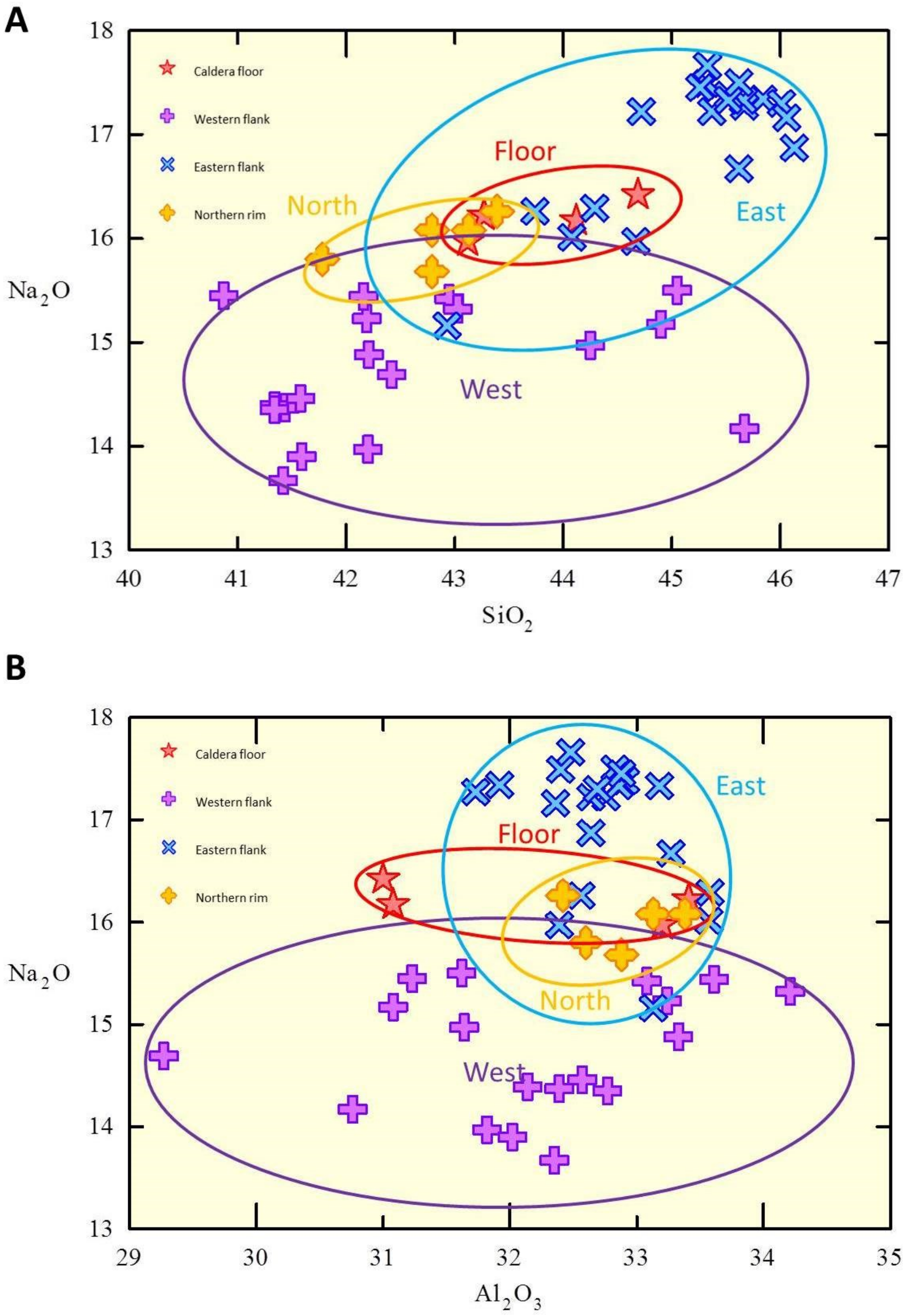

Figure 32. Embagai nepheline compositions: **(A)** SiO_2 vs. Na_2O and **(B)** Al_2O_3 vs. Na_2O. The eastern and northern rim nephelines are less variable in composition.

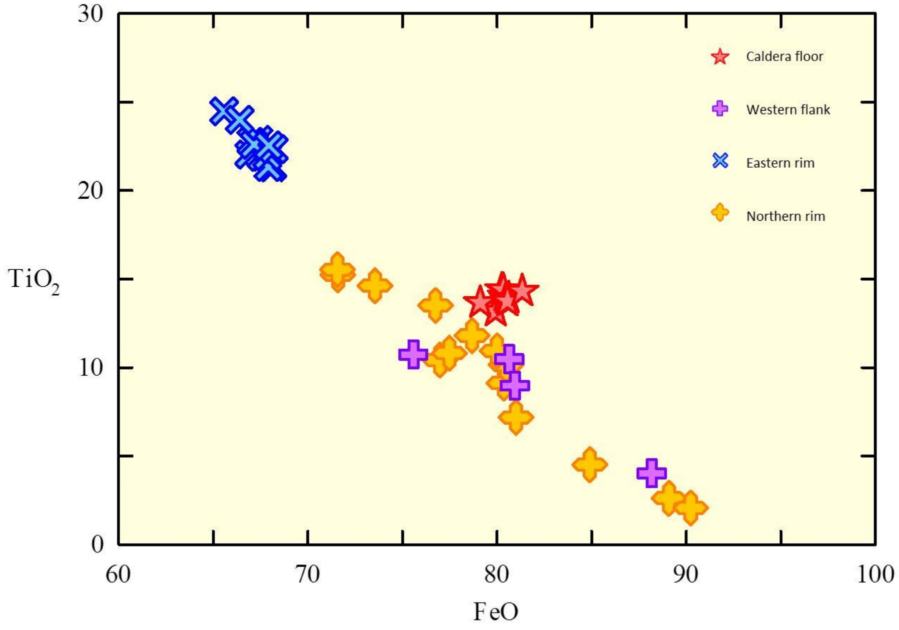

Figure 33. Oxides: TiO_2 vs FeO. Titanomagnetite compositions from Embagai's caldera floor and eastern rim are tightly clustered. The northern rim and western flanks of Embagai are more spread out.

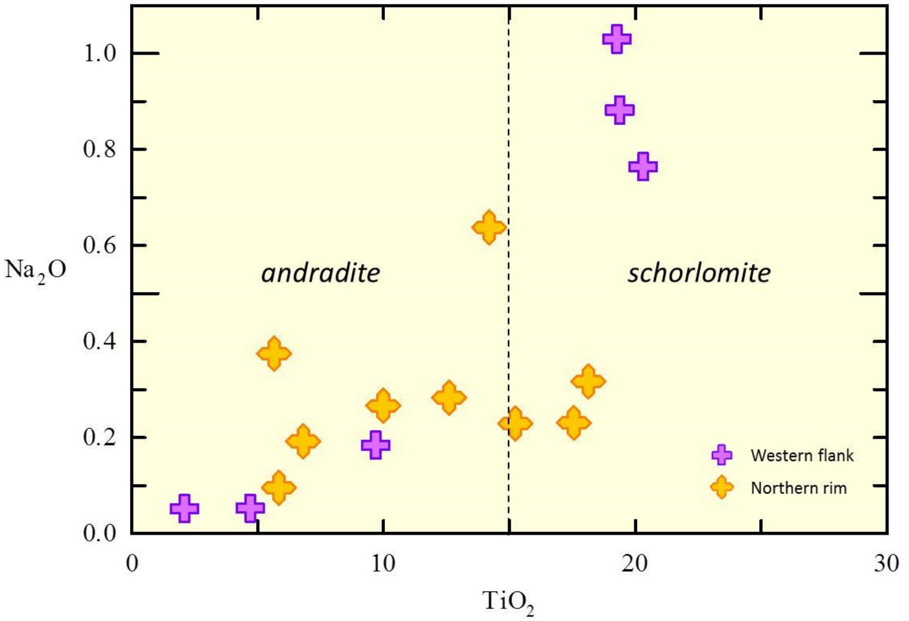

Figure 34. Embagai andradite garnets, showing a generally positive trend between TiO_2 and Na_2O. Both the western flank and northern rim of Embagai have Ti-rich schorlomite (garnets with > 15 wt. % TiO_2, Deer et al., 1992).

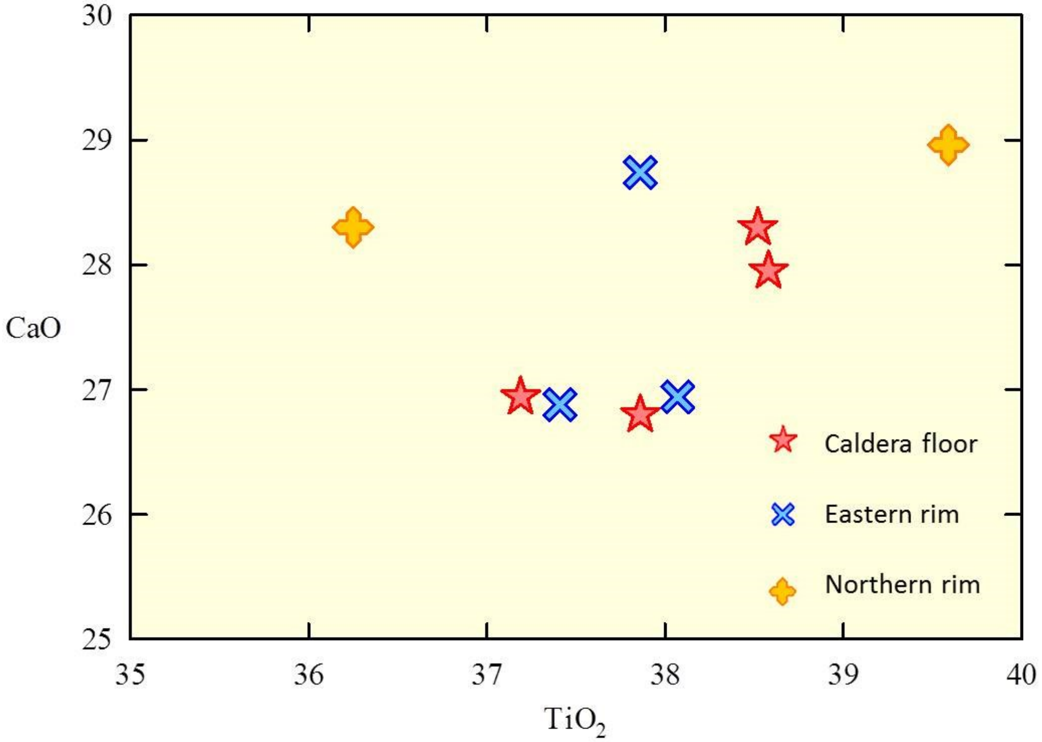

Figure 35. Embagai sphene (titanite): No consistent trend is observed between TiO_2 and CaO. No sphenes were identified in the western flank samples.

5. RESULTS: NATRON BASIN

5.1. Bulk geochemical composition

Tables 5.1 and **5.2** detail the bulk geochemical compositions of the Natron basin samples previously described in Section 3.1.2. Most samples plot as basalts on a Total Alkali-Silica (TAS) diagram (**Figure 36a and 36b**, after Le Bas et al., 1986), with some as trachybasalts. The Hajaro samples are less sodic than the Wa Mbugu basalts or the Sambu trachybasalts. The major elements of western Natron basin basalts were plotted to help establish relationships between the known samples and the questionable or unknown samples (**Figure 37**). One relationship that can be seen is between the definitive Wa Mbugu sample 10-T24 and the questionable Wa Mbugu candidate 08-P13. In the TAS diagram, 10-T24 and 08-P13 appear to possess similar bulk chemistry. This relationship is further strengthened by overlap or close proximity between the two samples indicating that 08-P13 is consistent with Wa Mbugu basalt.

Sample 07-P21, collected from a flow at the summit of the presumed source of the Wa Mbugu lava, is compositionally distinct from the established Wa Mbugu sample. Samples 12-P3 and 12-P4, collected on the slopes and base (respectively) of the same presumed source volcano, are similar in composition to 07-P21 and also compositionally distinct from the Wa Mbugu. Samples 11-T23 and 11-T24, collected from near the base and top of a thick and continuous section of the Humbu Formation, were compositionally indistinguishable, indicating that bulk major and minor elements alone are not sufficient to develop unique geochemical fingerprints for individual lava flows.

Sample	Description	SiO_2	Al_2O_3	Fe_2O_3	MnO	MgO	TiO_2	CaO	Na_2O	K_2O	P_2O5	LOI	TOTAL
07-P1	Sambu	43.76	13.55	11.02	0.14	6.47	1.72	12.09	4.02	0.90	0.29	6.54	100.68
07-P3	Hajaro	45.98	14.44	11.55	0.13	6.70	1.88	12.27	2.70	0.67	0.31	2.97	99.79
07-P21	Source?: Top	43.16	11.88	12.89	0.16	8.19	3.10	11.37	3.35	1.53	0.70	3.85	100.53
08-P13	Wa Mbugu?	45.73	14.14	12.56	0.15	6.48	2.11	11.48	3.49	0.74	0.36	2.49	99.92
10-T24	Wa Mbugu	46.06	14.32	12.54	0.15	6.36	2.13	11.25	3.64	0.79	0.36	2.02	99.79
11-T17	Hajaro	46.44	14.35	12.03	0.15	5.79	1.95	12.39	2.79	0.99	0.34	2.62	100.05
11-T23	Unknown	46.79	15.18	12.35	0.14	4.97	2.61	10.51	3.41	1.26	0.59	1.51	99.58
11-T24	Unknown	46.52	15.22	12.57	0.15	5.21	2.66	10.63	3.38	1.28	0.59	1.02	99.46
12-P3	Source?: Slope	43.64	12.13	12.89	0.16	7.70	2.85	10.65	4.23	1.80	0.57	1.72	98.62
12-P4	Source?: Base	43.96	14.92	10.82	0.12	5.75	2.12	10.41	2.37	2.62	0.44	5.07	98.84

Table 5.1. Natron basin major element bulk geochemical compositions. Values are in wt. %.

Sample	Description	Y	Zr	Nb	V	Zn	Ni	Cr	Ce	Sr	Ba
07-P1	Sambu	21	93	25	479	100	84	123	n.d.	447	279
07-P3	Hajaro	22	88	26	485	106	93	144	n.d.	460	263
07-P21	Source?: Top	21	259	123	444	126	114	313	n.d.	1201	769
08-P13	Wa Mbugu?	22	121	40	474	124	83	96	n.d.	454	352
10-T24	Wa Mbugu	23	111	32	474	118	84	104	n.d.	382	302
11-T17	Hajaro	25	101	22	505	104	79	140	n.d.	458	390
11-T23	Unknown	26	157	46	441	126	59	101	167	824	608
11-T24	Unknown	23	149	47	426	141	60	89	n.d.	485	589
12-P3	Source?: Slope	22	260	123	185	136	114	257	n.d.	894	689
12-P4	Source?: Base	25	199	90	126	140	87	209	n.d.	804	669

2LLD	Average	7	27	21	50	38	31	54	152	32	126

Table 5.2. Natron basin minor element bulk geochemical compositions. Values are in PPM. Below is the average of detection limits based on twice the Lower Limit of Detection (2LLD).

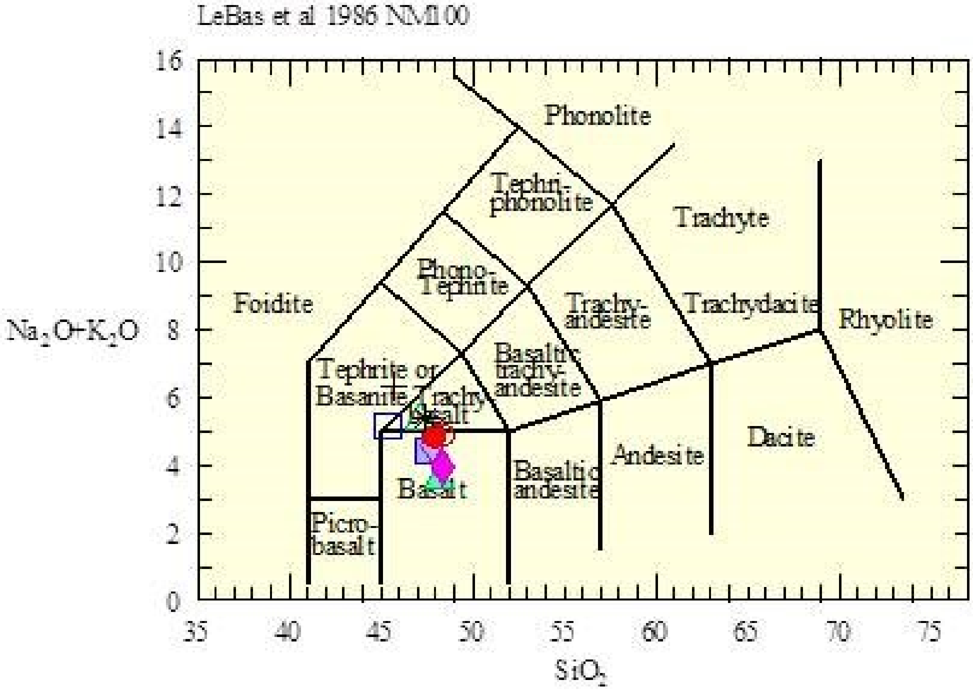

Figure 36a. Total Alkali-Silica (TAS) diagram of Natron samples (Le Bas et al., 1986). Most samples plot as basalt, with some trachybasalt. See Figure 36b for detail.

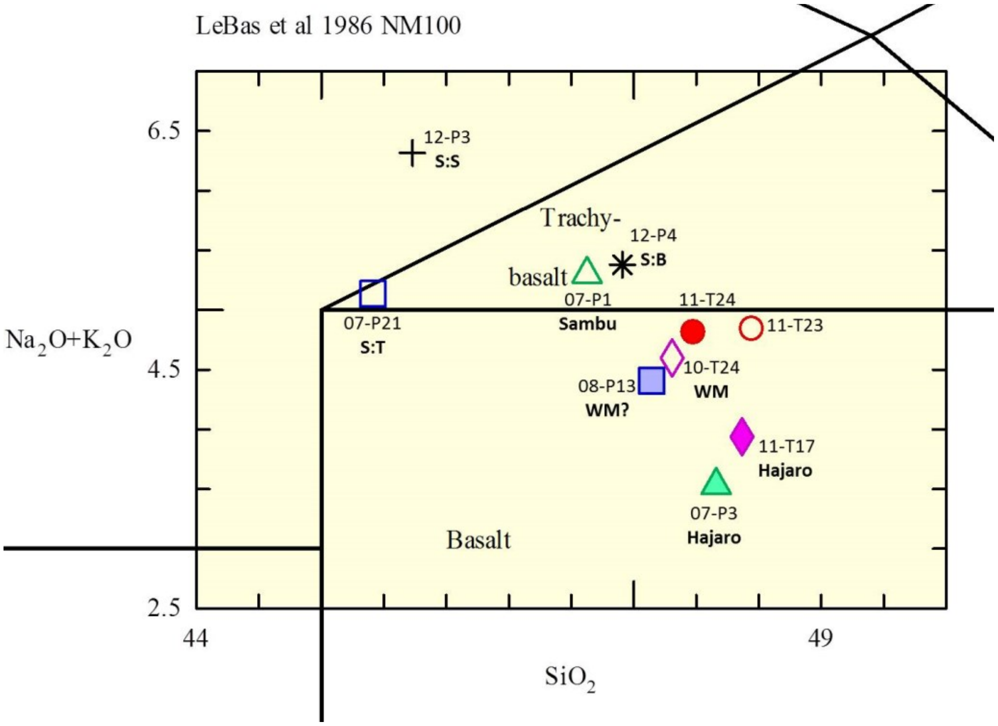

Figure 36b. Detail on TAS diagram (36a), showing similarity between samples. Samples10-T24 (Wa Mbugu) and 08-P13 overlap. 07-P21 is removed from remainder of samples. 07-P1 (Sambu) plots as a trachybasalt.

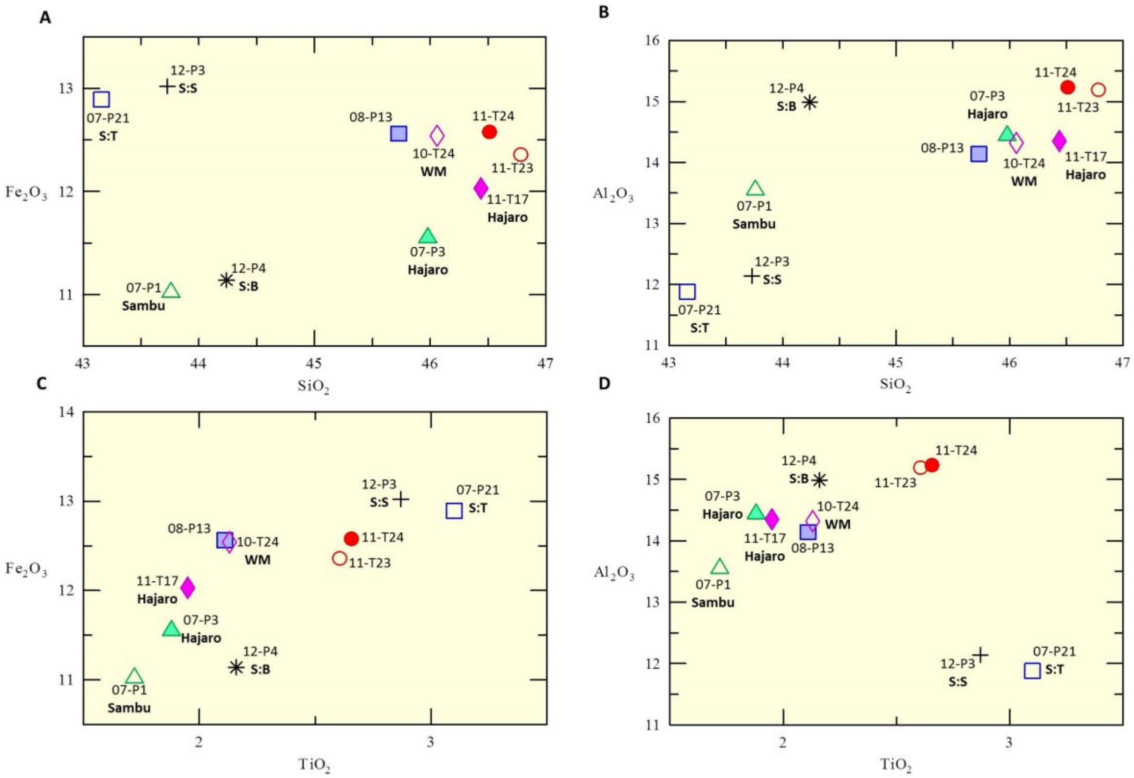

Figure 37. Plots of major element concentrations of Natron basalts. Plots of **(A)** Fe_2O_3 vs. SiO_2, **(B)** Al_2O_3 vs. SiO_2, **(C)** Fe_2O_3 vs. TiO_2, and **(D)** Al_2O_3 vs. TiO_2. Known samples Wa Mbugu (WM), Sambu, and Hajaro are identified, as are the three samples from the supposed "source volcano" (S:T = Source?: Top, S:S = Source?: Slope, S:B = Source?: Base). Definitive Wa Mbugu (WM) overlaps with 08-P13, indicating that candidate sample is compositionally consistent with the Wa Mbugu. Samples 11-T23 and 11-T24 frequently plot together, though they cannot represent the same lava flow as they were collected at the same site, separated by tens of meters of sediments and volcanics including the Main Humbu Tuff. 11-T23 (open red circle) is a geochemical split of the oriented paleomag sample 10-T21 (see Section 5.2). For most elements, 07-P21 and 12-P3 are outliers.

5.2. Paleomagnetism

Samples 10-T21 (Hajaro or Wa Mbugu basalt) and 10-T25 (definitive Wa Mbugu) were both sampled and analyzed paleomagnetically. Since 10-T21 represents the same unit as 11-T23 (composition described above in Section 5.1), this can help to better constraint the relative ages and compositions of these rocks in the Natron basin.

The Wa Mbugu candidate sample 10-T21 has a Fisher mean direction of 173.7° declination, -9.5° inclination, and an α_{95} of 11.6°, n=3. (**Figure 38**). The maximum angular deviation (MAD) in 10-T21 was relatively low (< 5.2°, **Table 6**). Sample 10-T21 had a single component of magnetization, though it was not fully demagnetized by 100mT or 500°C, short of the measured Curie temperature (T_C). The measurements of 10-T21 are consistent with reversed polarity. Of the possible units that this could represent, 10-T21 would be most consistent with the Hajaro Basalt which also has a reversed polarity (Isaac, 1967), though this sample is compositionally unlike the Hajaro (see Section 6.2.1 for discussion).

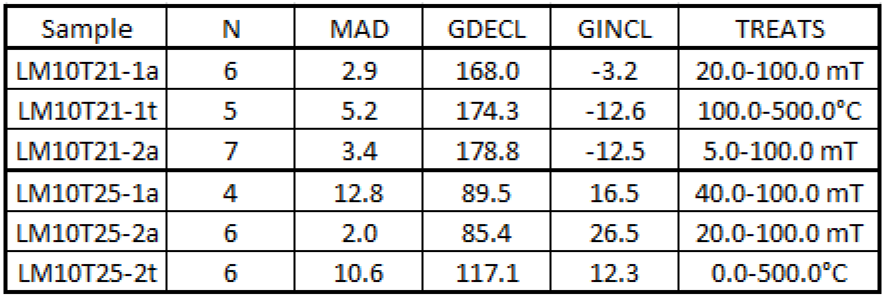

Sample	N	MAD	GDECL	GINCL	TREATS
LM10T21-1a	6	2.9	168.0	-3.2	20.0-100.0 mT
LM10T21-1t	5	5.2	174.3	-12.6	100.0-500.0°C
LM10T21-2a	7	3.4	178.8	-12.5	5.0-100.0 mT
LM10T25-1a	4	12.8	89.5	16.5	40.0-100.0 mT
LM10T25-2a	6	2.0	85.4	26.5	20.0-100.0 mT
LM10T25-2t	6	10.6	117.1	12.3	0.0-500.0°C

Table 6. Results of AF and thermal demagnetization. N is the number of data points per sample run. The maximum angular deviation (MAD) is more variable in 10-T25 than in 10-T21. Declination and inclination are given in geographic coordinates. AF demagnetization steps are in milliTesla (mT).

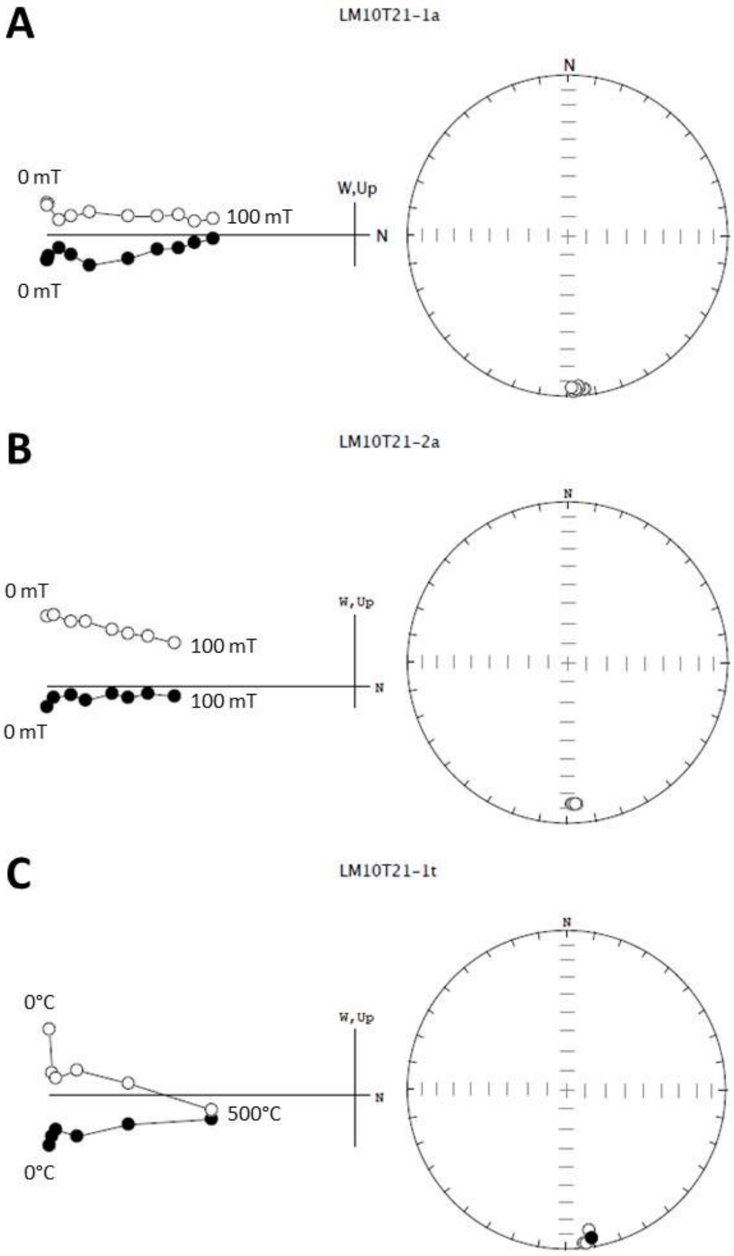

Figure 38. Paleomagnetic orthogonal diagrams (Zijderveld, 1967) of 10-T21 (Hajaro or Wa Mbugu basalt). Solid (open) symbols are horizontal (vertical) projections respectively. Solid (open) symbols are projections onto the lower (upper) hemisphere. Note single component of magnetization and low maximum angular deviation. **(A)** and **(B)** are AF demagnetization, while **(C)** is thermal demagnetization. Sample is consistent with reversed polarity.

AF demagnetization of the Wa Mbugu sample10-T25 revealed at least two components of magnetization, though thermal demagnetization behavior was less stable and only one specimen was interpreted. This direction, however, was broadly consistent with the high-coercivity AF component.

Sample 10-T25 has a Fisher mean direction of 97.6° declination and 19.0° inclination with an α_{95} of 27.9° (**Figure 39**). The MAD in 10-T25 was on average higher than in sample 10-T21 (upwards of 12.8°, **Table 6**).

The AF and thermal results for sample 10-T21 are consistent with each other (**Table 6**), and confirmed with the α_{95} confidence value of 11.6°. The AF and thermal results of 10-T25 are much more variable, as evident by the α_{95} confidence value of 27.9°.

A dominant Curie temperature of 517°C derived from the χ(T) data from the heating curve (**Figure 40A**) suggests that titanomagnetite is the primary magnetic mineral in 10-T21. It should be noted that the sample was only heated to 600°C, and the presence or absence of higher-T_C minerals such as hematite therefore cannot be determined. Hematite is likely considering the generally high degree of alteration of basalts in the region.

For sample 10-T25 (**Figure 40B**), the χ(T) data (i.e. the heating and cooling curves) are highly irreversible. The data are consistent with an inversion of titanomaghemite to magnetite and ilmenite upon heating.

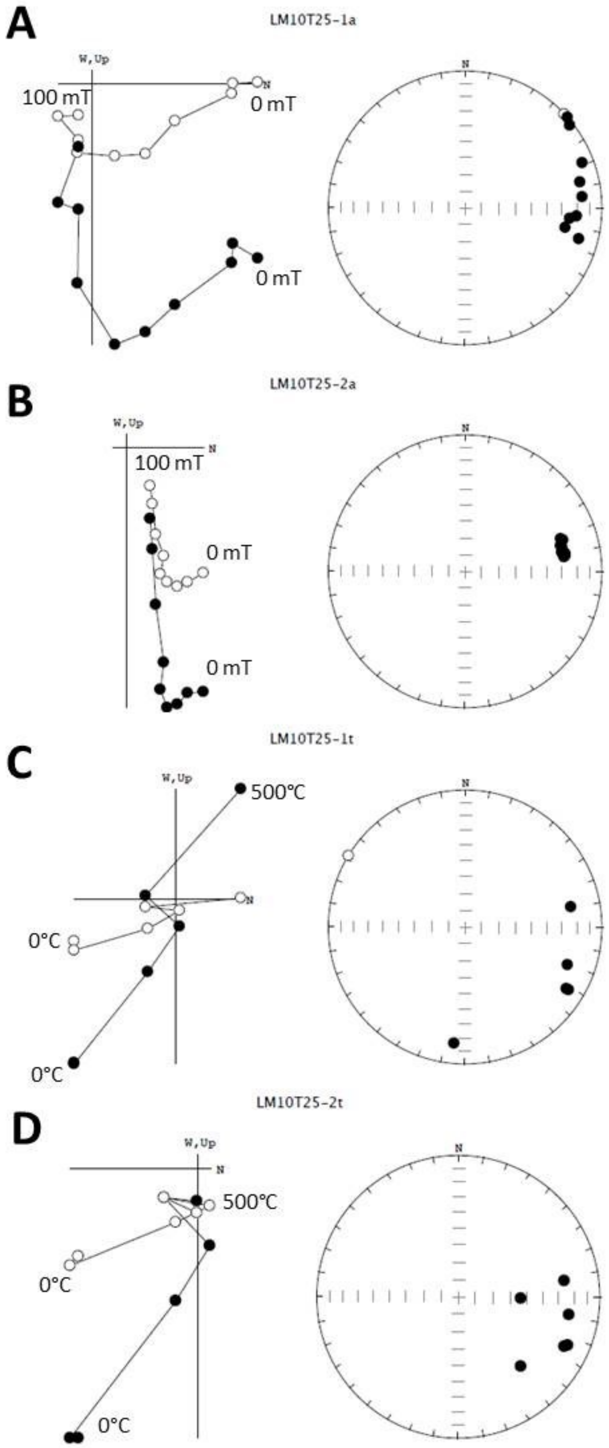

Figure 39. Paleomagnetic orthogonal diagrams (Zijderveld, 1967) of 10-T25 (Wa Mbugu basalt). Solid (open) symbols are horizontal (vertical) projections respectively. Note scatter and irregular demagnetization trends. **(A)** and **(B)** are AF demagnetization, while **(C)** and **(D)** are thermal demagnetization. Specimen C was not interpreted or included in the mean. The sample is consistent with transitional polarity.

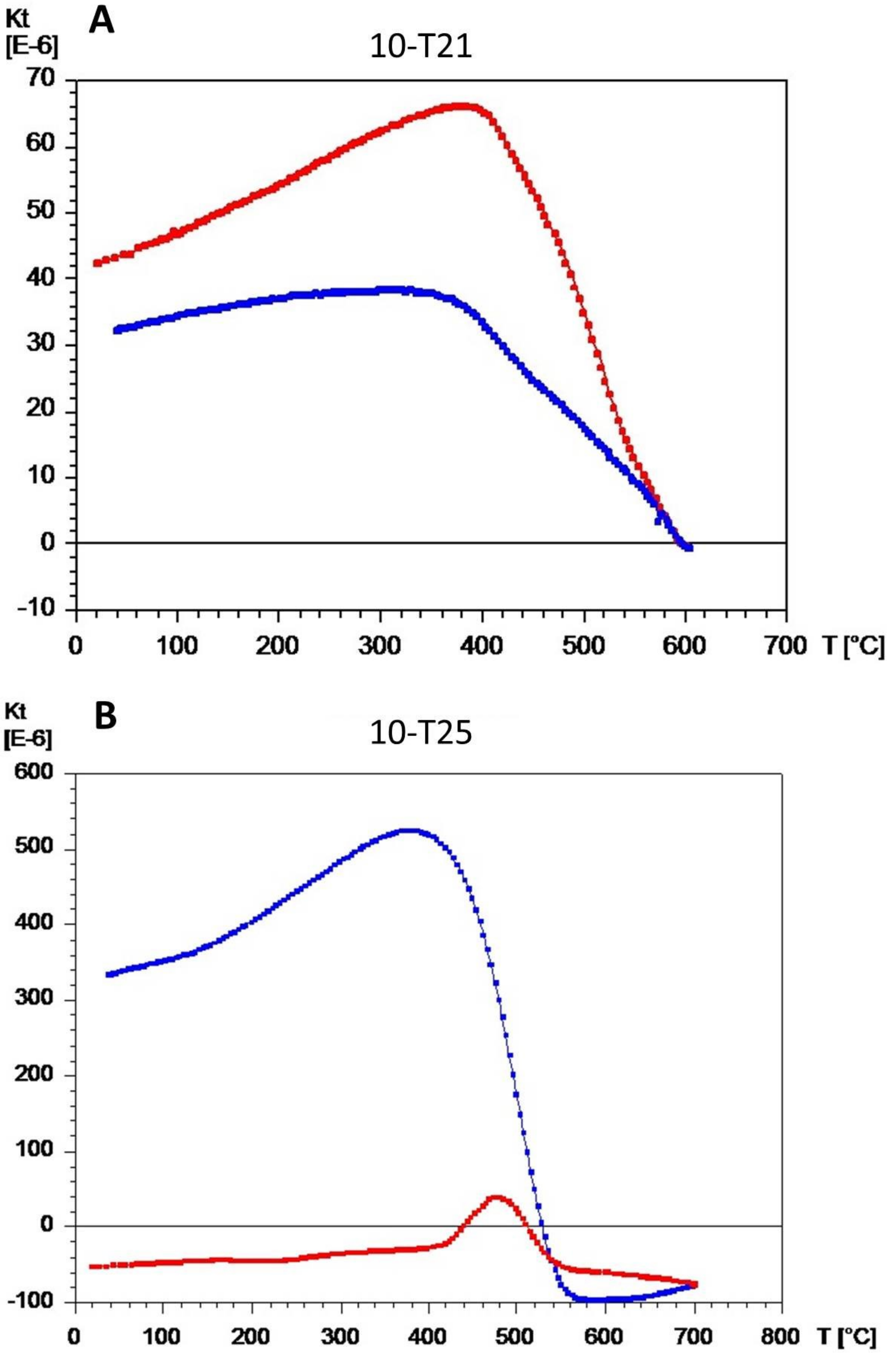

Figure 40. Susceptibility (χ) as a function of temperature (T) for Natron basalts **(A)** 10-T21 (Wa Mbugu candidate) and **(B)** 10-T25 (Wa Mbugu basalt). **(A)** The maximum temperature of heating was 600°C. The inflection point of the heating curve is 517°C. The cooling curve has lower susceptibility. The data are consistent with titanomagnetite. **(B)** The maximum temperature of heating for sample 10-T25 was 700°C. The data are consistent with titanomaghemite before heating, which converted to magnetite and ilmenite upon heating.

6. DISCUSSION

6.1 Embagai

Embagai is mostly nephelinite to phono-tephrite in composition, based on the results of this thesis and from Mollel's (2007) study. Most Embagai lava samples analyzed for this study have high LOI values, which reflects significant alteration and limit the reliability of the XRF results for the analysis of primary igneous composition. As shown in the XRD results, calcite and zeolites (such as analcime) are also abundant, as a result of post-depositional processes. The abundance of calcite in certain samples may be related to a previous saline crater lake, localized fossil fumarole activity, or the alteration of carbonatite ash derived from nearby younger volcanoes such as Ol Doinyo Lengai and Kerimasi. The absence of feldspar and the presence of nepheline in the least altered samples is consistent with the nephelinitic composition of the lavas, though in some cases where both are missing and zeolites are abundant it is possible that zeolites replaced the primary phases. The augite phenocrysts are however more resistant to alteration and allow us to compare directly with phenocrysts found in Olduvai Gorge.

6.1.1 Embagai and its relationship to Olduvai Gorge

Embagai augite compositions (**Figure 41A**, FeO vs. MgO) are similar to those observed for Olduvai Bed II and some high-Mg Upper Bed I tuffs (**Tables 7.1, 7.2,** and **7.3**, data provided by McHenry). However, Embagai is most recently dated at 0.81 ± 0.02 Ma to 1.16 ± 0.04 Ma (Mollel, 2007), with previous dates ranging from 0.5 ± 0.14 to 1.52 ± 0.03 Ma (Manega, 1993). Since Olduvai Tuff IF (the boundary between Beds I and II) is most recently dated at 1.803 ± 0.002 Ma (Deino, 2012), tuffs from Bed II and younger exposures at Olduvai are more likely candidates for correlation.

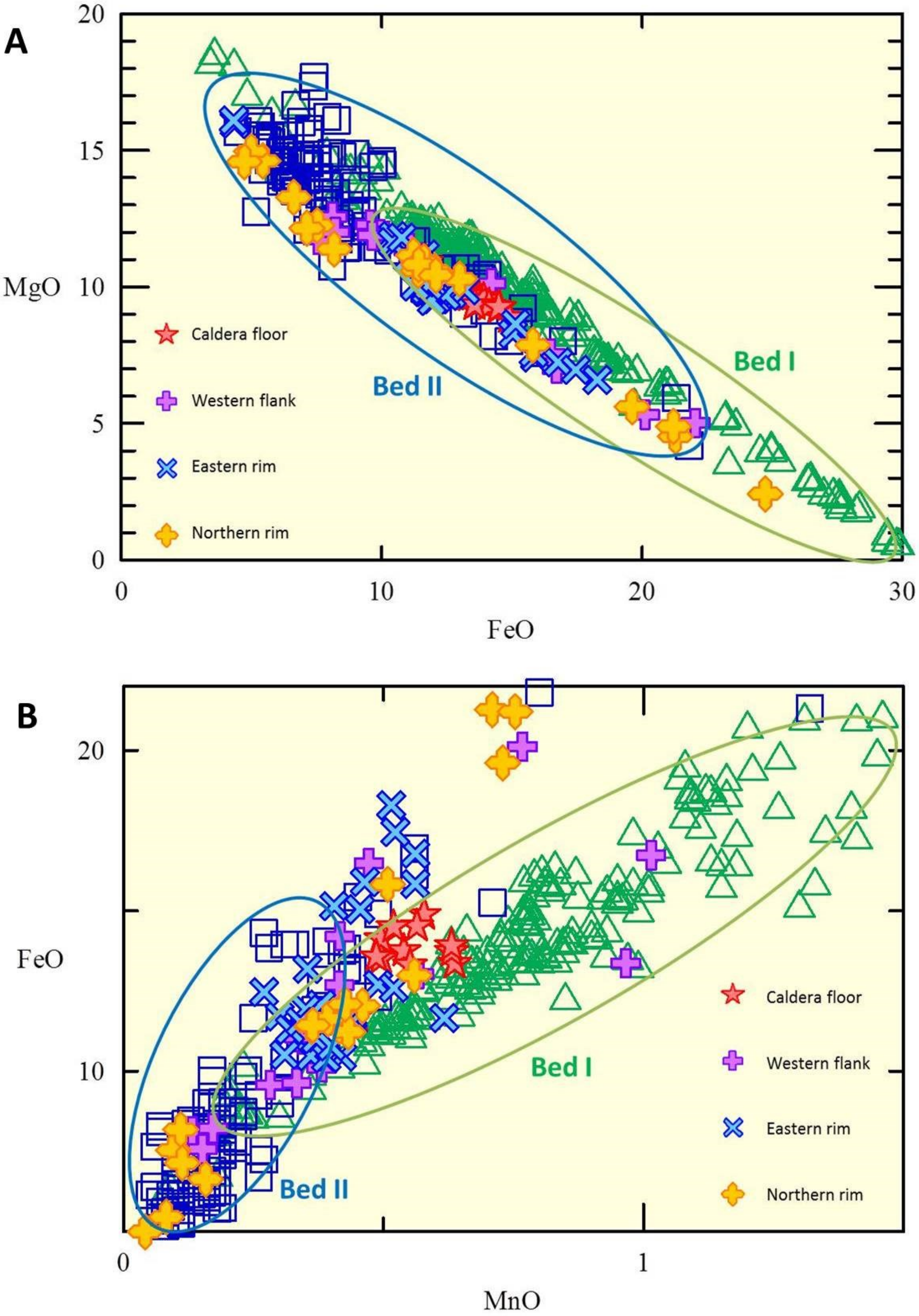

Figure 41. Augite phenocryst comparison plot of **(A)** FeO vs. MgO and **(B)** MnO vs. FeO: Embagai vs. Olduvai Bed I (open green triangles) and Bed II (open blue squares) (data provided by McHenry). **(A)** All augites follow a similar trend, with an inverse correlation between iron and magnesium (as expected for this solid solution). Caldera floor augites overlap both Beds I and II. **(B)** Embagai caldera floor augites plot close to Bed I, whereas eastern rim, northern rim, and western flank augites correspond with Bed II more closely. The ovals in both plots are drawn to reflect general grouping of Bed I and II populations and do not include outliers.

In the FeO vs. MgO plot for Embagai augite **(Figure 41A**), the western flank and northern rim are most similar to the high-Mg augites from Olduvai Bed II (10-15 wt. % MgO). Additionally, a second population of eastern rim augites overlaps with some high-Mg Bed II augites. A plot of MnO vs. FeO (**Figure 41B**) better distinguishes Olduvai Bed I and II augite compositions. Embagai western flank and eastern rim augites are more similar to Bed II, which is consistent with the most recent dates. Northern rim augites appear to overlap portions of both Bed I and Bed II.

Feldspar compositions from Embagai do not overlap with those from Olduvai Bed I or II (**Figure 42**). Feldspar is absent from most Embagai samples independent of the degree of alteration; these silica-undersaturated lavas are nepheline-rich instead. The few Embagai feldspars identified and analyzed are K-rich, which differs from the anorthoclase and plagioclase feldspars present in Olduvai Bed I and II tuffs. As K-feldspar is observed in some of the more altered samples (alongside the zeolite mineral phillipsite), it is possible that they represent a secondary alteration phase rather than a primary igneous mineral (e.g. McHenry, 2009; 2010). However, less altered sample 13-T32 likely contains primary igneous K-feldspar. It is unclear whether feldspars from Embagai represent an undiscussed bed or series of beds (e.g. Olduvai Beds III and above). It is possible that prevailing winds at the time of eruption did not encourage dispersal in the direction of Olduvai, thus limiting deposition of Embagai materials, or that Embagai did not erupt as explosively as its neighbors.

Embagai oxide compositions are generally more Fe-rich and less Ti-rich than Olduvai Beds I and II, except for eastern rim oxides which overlap with Bed I (**Figure 43**).

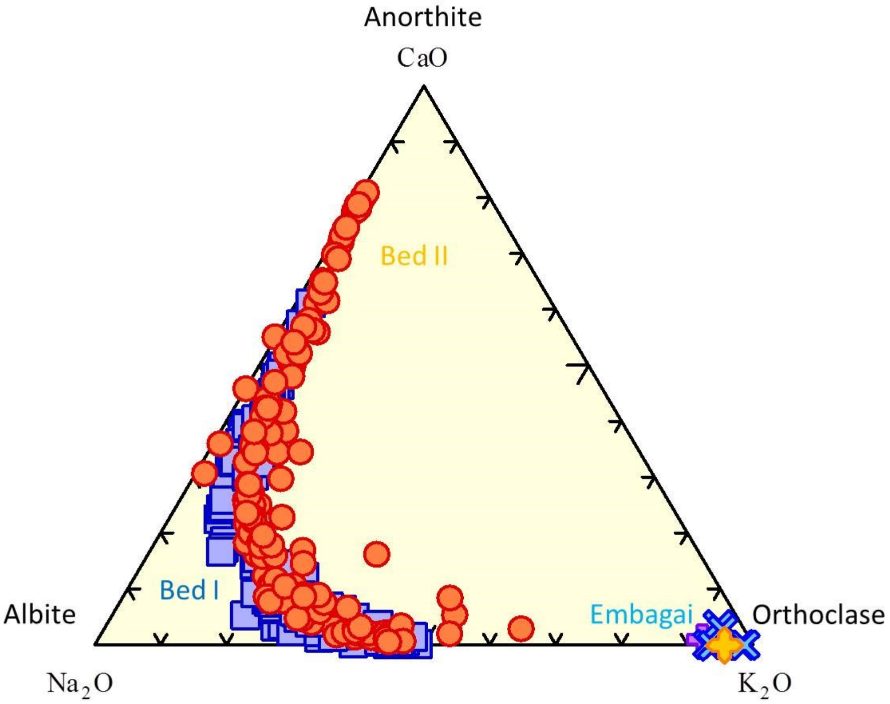

Figure 42. Feldspar phenocryst ternary plot: Embagai vs. Bed I and Bed II. Embagai feldspars are K-feldspar, where most Bed I and II feldspars range from anorthoclase to plagioclase.

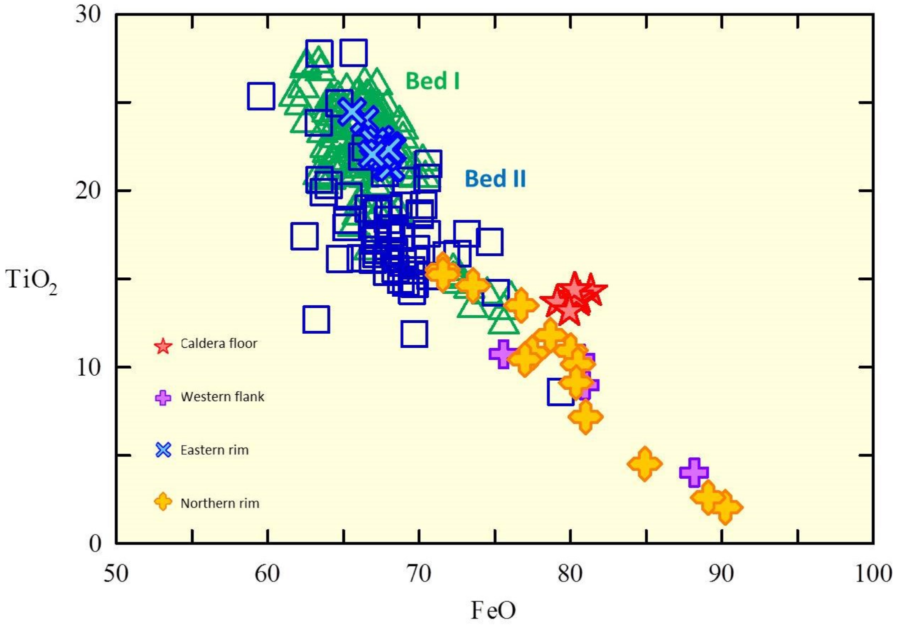

Figure 43. Oxide phenocryst comparison plot: Embagai vs. Olduvai Bed I and II. With the exception of the eastern rim, Embagai oxides are more Fe-rich than oxides from Beds I or Bed II, which are more Ti-rich.

			Bed I											Bed II							Bed III
Phenocryst	Geologic Unit		Naabi Ignimbrite	CFCT	Tuff IA	Tuff IB	Tuff IC	Tuff ID	Tuff IE	Ng'eju lower	Ng'eju upper	Tuff IF (surge)	Tuff IF (lapilli)	Tuff IIA	Tuff IIB	BPT	BTS	Tuff IIC lower	Tuff IIC upper	Tuff IID	Tuff IIIA
Augite (pyroxene)	N		6	18	6	15	26	32	13	22	33	10	21	11	10	23	16	4	8	28	14
	wt% SiO_2	Average	49.13	49.61	52.83	49.06	50.99	50.53	51.20	51.30	50.90	50.93	50.93	49.09	50.47	49.84	48.80	48.65	49.40	50.42	49.57
		St Dev	1.81	0.44	1.48	0.76	0.96	1.27	1.09	0.89	1.15	0.87	0.57	1.27	1.12	1.72	2.09	2.05	0.93	1.66	1.14
	wt% Al_2O_3	Average	0.17	0.30	1.92	0.48	1.28	1.16	1.09	1.58	2.62	1.12	1.45	4.30	2.53	3.42	3.93	3.68	2.98	2.51	2.20
		St Dev	0.05	0.09	0.62	0.08	0.94	0.45	0.57	0.50	1.46	0.32	0.38	1.45	0.98	1.29	1.92	1.17	0.50	1.76	1.44
	wt% TiO_2	Average	0.35	0.33	0.63	0.43	0.57	0.66	0.62	0.75	1.05	0.46	0.93	1.87	1.76	1.35	1.83	2.19	1.93	1.27	1.08
		St Dev	0.04	0.06	0.34	0.06	0.37	0.23	0.33	0.28	0.47	0.09	0.25	0.66	0.51	0.58	0.76	0.86	0.60	0.62	0.69
	wt% FeO	Average	27.47	26.55	5.55	18.83	14.90	14.11	13.99	12.80	10.76	16.27	13.48	8.42	9.70	7.94	8.36	6.11	6.55	11.08	13.75
		St Dev	3.03	1.32	2.10	1.72	4.39	1.53	2.99	1.32	1.34	2.97	0.44	2.26	4.36	2.19	2.64	0.74	0.40	3.97	3.98
	wt% MnO	Average	1.36	1.28	0.13	1.28	0.91	0.71	0.82	0.63	0.45	0.97	0.80	0.23	0.25	0.20	0.18	0.09	0.12	0.33	0.41
		St Dev	0.13	0.06	0.05	0.20	0.39	0.14	0.30	0.09	0.14	0.14	0.07	0.15	0.19	0.09	0.09	0.03	0.05	0.24	0.18
	wt% MgO	Average	2.15	2.83	17.04	7.61	9.99	10.55	9.99	10.97	12.33	8.29	11.20	12.89	12.85	14.68	12.67	14.35	14.32	11.31	8.70
		St Dev	2.12	0.88	1.33	1.18	3.07	1.19	1.61	0.99	0.65	2.18	0.38	1.68	3.05	1.85	2.33	1.07	0.22	2.42	2.40
	wt% CaO	Average	16.97	18.40	21.66	19.69	19.51	21.32	20.68	20.71	20.68	20.21	20.27	21.77	22.20	21.42	22.49	23.68	23.59	21.55	19.94
		St Dev	0.81	0.23	0.74	0.20	0.60	0.37	0.91	0.38	0.31	1.34	0.31	0.58	1.53	1.48	1.54	0.46	0.73	1.44	2.42
	wt% Na_2O	Average	1.34	0.67	0.41	0.82	0.67	0.41	0.59	0.46	0.45	1.42	0.82	0.98	1.02	0.72	0.99	0.61	0.53	1.23	2.28
		St Dev	0.48	0.11	0.08	0.19	0.13	0.12	0.08	0.04	0.06	0.75	0.09	0.34	0.63	0.63	0.76	0.11	0.08	0.77	1.33
	wt% Total	Average	98.95	99.98	100.20	98.22	98.85	99.48	99.01	99.25	99.29	99.76	99.93	99.58	100.79	99.58	99.29	99.34	99.40	99.74	98.03
		St Dev	1.15	0.54	0.35	0.90	0.75	1.17	1.54	0.80	0.87	0.72	0.48	1.02	0.42	1.44	0.45	0.52	0.41	0.69	0.66

Table 7.1. Averages and standard deviations of augite compositions in Olduvai Bed I (IB, IC, ID, IE, Ng'eju, and IF: McHenry, 2005; Naabi, CFCT, and IA: McHenry et al., 2008; IF: McHenry, et al., 2011; IA and Ng'eju: McHenry, 2012), II (IIA: McHenry et al., 2008, McHenry, 2012; IID and BPT: McHenry et al., 2011; IIB, IIC, and BTS: McHenry, unpublished), and III tuffs (IIIA: McHenry, unpublished) as measured by EPMA. N = Number of grains analyzed. Geologic units are in stratigraphic order from oldest to youngest.

			Bed I										Bed II							Bed III
Phenocryst	Geologic Unit		Naabi Ignimbrite	CFCT	Tuff IB	Tuff IC	Tuff ID	Tuff IE	Ng'eju lower	Ng'eju upper	Tuff IF (surge)	Tuff IF (lapilli)	Tuff IIA	Tuff IIB	BPT	BTS	Tuff IIC lower	Tuff IIC upper	Tuff IID	Tuff IIIA
Feldspar	N		14	20	13	51	21	24	14	14	13	24	23	15	9	17	15	18	41	2
	wt% SiO_2	Average	67.48	66.75	65.18	64.17	60.82	65.28	59.36	60.51	68.09	66.12	61.76	60.82	57.63	63.66	63.73	60.92	62.88	63.85
		St Dev	0.61	0.34	0.51	1.04	2.21	0.68	1.95	1.24	0.80	0.89	4.67	3.71	7.16	5.02	4.82	5.27	2.55	1.11
	wt% Al_2O_3	Average	18.22	19.60	19.31	20.76	23.25	20.88	23.95	23.02	19.29	19.22	23.08	23.56	26.53	21.69	22.06	24.72	22.26	19.95
		St Dev	0.26	0.24	0.21	0.40	1.02	0.37	0.75	1.00	0.63	0.57	3.40	2.79	5.06	3.62	3.12	3.52	1.68	0.79
	wt% FeO	Average	0.67	0.33	0.31	0.23	0.21	0.20	0.28	0.27	0.25	0.43	0.34	0.55	0.46	0.43	0.33	0.35	0.25	0.11
		St Dev	0.16	0.07	0.08	0.03	0.04	0.09	0.06	0.03	0.08	0.09	0.19	0.23	0.14	0.20	0.14	0.16	0.10	0.10
	wt% CaO	Average	0.03	0.10	0.32	1.28	3.85	1.30	5.33	7.18	0.83	0.81	4.08	4.60	8.82	2.90	3.58	6.19	3.05	0.54
		St Dev	0.05	0.07	0.13	0.32	1.07	0.25	0.90	1.02	0.41	0.25	3.82	3.19	5.97	4.21	3.81	4.34	1.97	0.54
	wt% Na_2O	Average	7.24	7.56	8.94	8.90	8.12	8.71	7.50	6.94	7.43	8.07	7.02	7.10	5.45	7.24	7.60	6.90	7.74	4.85
		St Dev	0.30	0.33	0.43	0.11	0.33	0.22	0.50	0.50	0.57	0.35	1.14	0.99	1.95	1.37	1.50	1.92	0.63	4.13
	wt% K_2O	Average	6.17	6.06	4.30	2.74	0.75	3.05	0.83	0.58	3.77	3.49	2.93	2.34	1.80	3.60	2.43	1.27	2.00	9.44
		St Dev	0.32	0.29	0.73	0.26	0.26	0.23	0.22	0.11	1.06	0.34	2.45	1.93	2.30	2.22	1.66	1.35	1.22	6.53
	wt% BaO	Average	0.08	0.09	0.27	0.40	0.28	0.44	0.21	0.12	0.31	0.95	0.35	0.34	0.25	0.25	0.28	0.20	0.38	0.33
		St Dev	0.07	0.05	0.10	0.08	0.11	0.10	0.10	0.04	0.17	0.76	0.34	0.33	0.15	0.25	0.19	0.14	0.25	0.11
	wt% Total	Average	99.95	100.54	98.71	98.55	97.34	99.96	97.56	98.71	100.05	99.28	99.57	99.31	100.84	99.73	99.99	100.53	98.56	99.12
		St Dev	0.65	0.32	0.86	1.21	2.06	0.62	1.30	0.40	0.74	0.94	0.74	0.61	0.61	0.87	0.81	0.35	0.63	0.28

Table 7.2. Averages and standard deviations of feldspar compositions in Olduvai Bed I (IB, IC, ID, IE, Ng'eju, and IF: McHenry, 2005; Naabi, CFCT, and IA: McHenry et al., 2008; IF: McHenry, et al., 2011; IA and Ng'eju: McHenry, 2012), II (IID and BPT, McHenry et al., 2011; IIA: McHenry, 2012; IIB, IIC and BTS: McHenry unpublished), and III tuffs (IIIA: McHenry unpublished) as measured by EPMA. N = Number of grains analyzed. Geologic units are in stratigraphic order from oldest to youngest.

			Bed I								Bed II						Bed III
Phenocryst	Geologic Unit		Tuff IB	Tuff IC	Tuff ID	Tuff IE	Ng'eju lower	Ng'eju upper	Tuff IF (surge)	Tuff IF (lapilli)	Tuff IIA	Tuff IIB	BTS	Tuff IIC lower	Tuff IIC upper	Tuff IID	Tuff IIIA
Oxide (titanomagnetite or ilmenite)	N		12	13	17	20	14	14	15	18	5	7	15	15	9	11	11
	wt% SiO_2	Average	0.22	0.17	0.11	0.10	0.06	0.09	0.18	0.39	0.20	0.11	0.10	0.08	0.18	0.07	0.09
		St Dev	0.11	0.08	0.05	0.04	0.02	0.02	0.14	0.43	0.11	0.05	0.03	0.03	0.23	0.05	0.03
	wt% Al_2O_3	Average	0.53	1.00	1.42	0.96	1.64	3.29	0.70	1.06	3.19	2.03	2.75	2.55	2.00	2.64	1.86
		St Dev	0.17	0.14	0.22	0.05	0.21	1.23	0.37	0.13	1.28	0.84	1.03	0.82	1.26	1.19	0.83
	wt% TiO_2	Average	22.91	20.25	25.43	23.90	24.42	21.16	16.65	21.12	17.58	18.34	17.61	17.83	17.23	19.35	13.31
		St Dev	0.63	1.16	1.09	0.90	0.44	2.24	3.62	0.39	1.72	3.72	1.72	4.04	2.92	4.24	3.99
	wt% FeO	Average	66.23	67.23	64.35	65.80	67.10	66.25	72.29	65.32	66.51	68.64	68.10	68.15	67.64	68.28	75.77
		St Dev	1.49	1.59	1.50	1.92	0.37	0.42	2.53	1.54	1.36	5.24	2.18	3.45	3.13	2.71	5.25
	wt% MnO	Average	1.77	1.74	1.40	1.62	1.22	0.84	1.62	1.62	0.46	0.93	0.73	0.64	1.07	0.93	0.77
		St Dev	0.07	0.22	0.09	0.11	0.08	0.23	0.20	0.06	0.09	0.36	0.27	0.21	0.95	0.30	0.20
	wt% MgO	Average	0.67	0.74	1.36	1.00	1.59	3.50	0.42	1.33	5.39	3.58	5.11	4.94	3.15	3.52	3.28
		St Dev	0.16	0.11	0.24	0.06	0.27	1.16	0.57	0.13	0.94	1.95	1.85	2.02	2.25	2.57	1.74
	wt% CaO	Average	0.03	0.01	0.08	0.07	0.02	0.07	0.07	0.08	0.10	0.16	0.07	0.04	0.09	0.09	0.04
		St Dev	0.05	0.01	0.09	0.17	0.01	0.05	0.09	0.04	0.04	0.20	0.04	0.02	0.12	0.10	0.03
	wt% Total	Average	93.71	92.26	94.36	93.59	97.26	96.28	92.90	92.16	94.20	93.82	94.62	94.37	92.48	95.15	95.27
		St Dev	1.68	1.41	1.60	1.77	0.34	0.61	2.23	1.31	2.03	1.91	1.03	1.90	2.63	1.15	1.23

Table 7.3. Averages and standard deviations of oxide compositions in Olduvai Bed I (IB, IC, ID, IE, Ng'eju, and IF: McHenry, 2005; Naabi, CFCT, and IA: McHenry et al., 2008; IF: McHenry, et al., 2011; IA and Ng'eju: McHenry, 2012), II (IID and BPT, McHenry et al., 2011; IIA: McHenry, 2012; IIB, IIC and BTS: McHenry unpublished), and III tuffs (IIIA: McHenry unpublished) as measured by EPMA. N = Number of grains analyzed. Geologic units are in stratigraphic order from oldest to youngest.

6.1.2 Comparison to Olduvai Bed III

Microprobe data for augite, titanomagnetite, andradite, nepheline and perovskite of sample 02-T79 (Tuff IIIA, from Olduvai Locality 27) was used for comparison to Olduvai Bed III, (unpublished data, McHenry personal communication, 2014). Augite compositions are similar, with T79 overlapping significantly with most Embagai augites (**Figure 44**). Titanomagnetite compositions are very similar **(Figure 45**), with both Embagai and Bed III oxides following the trend of the northern rim and western flank, but not quite overlapping the eastern rim or caldera floor clusters. Andradite garnet compositions are also similar (**Figure 46**), though Bed III andradites are less than 15 wt % Ti, and thus not schorlomite or titanian andradites. Based on the results given in Figures 44-46, it appears more likely that Embagai contributed ash to Olduvai Bed III.

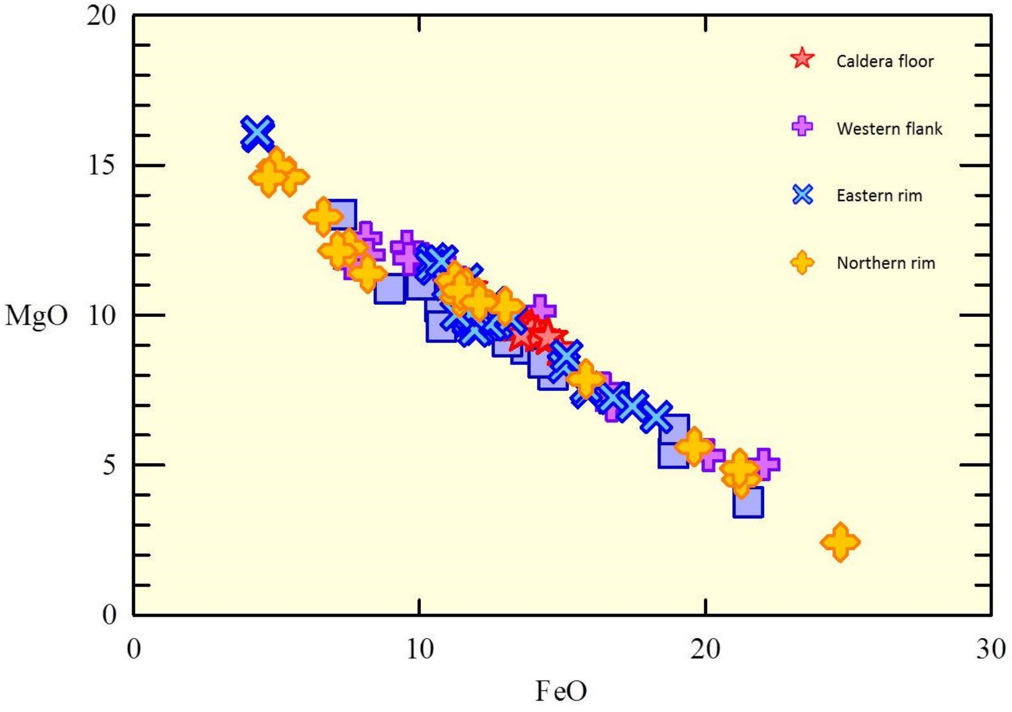

Figure 44. Augite phenocryst comparison of Embagai to Bed III (blue squares), showing significant overlap.

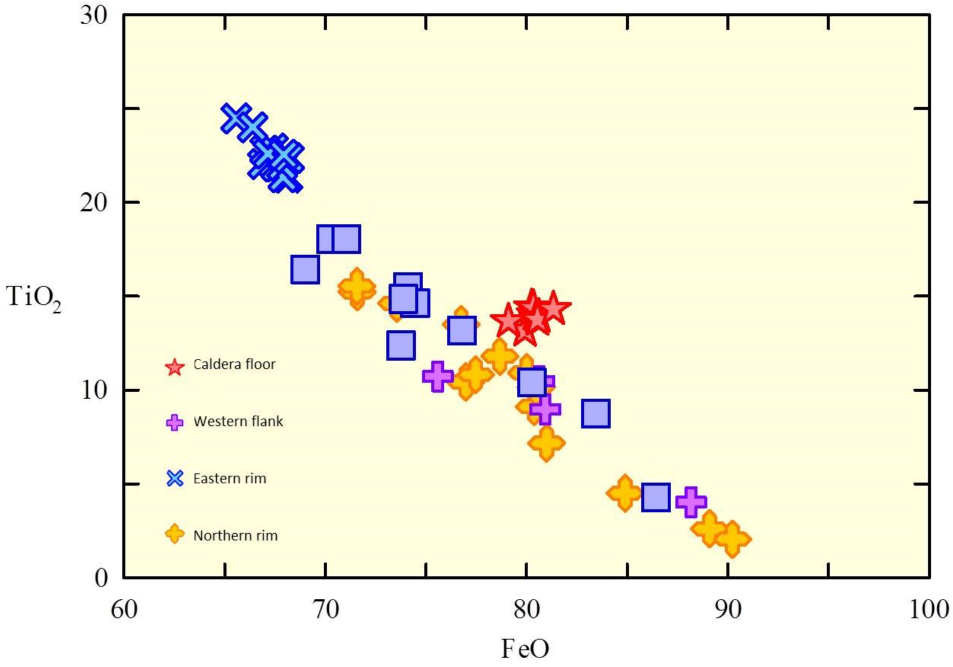

Figure 45. Titanomagnetite compositions for Embagai and Bed III (blue squares). The two show some overlap, especially for the northern rim.

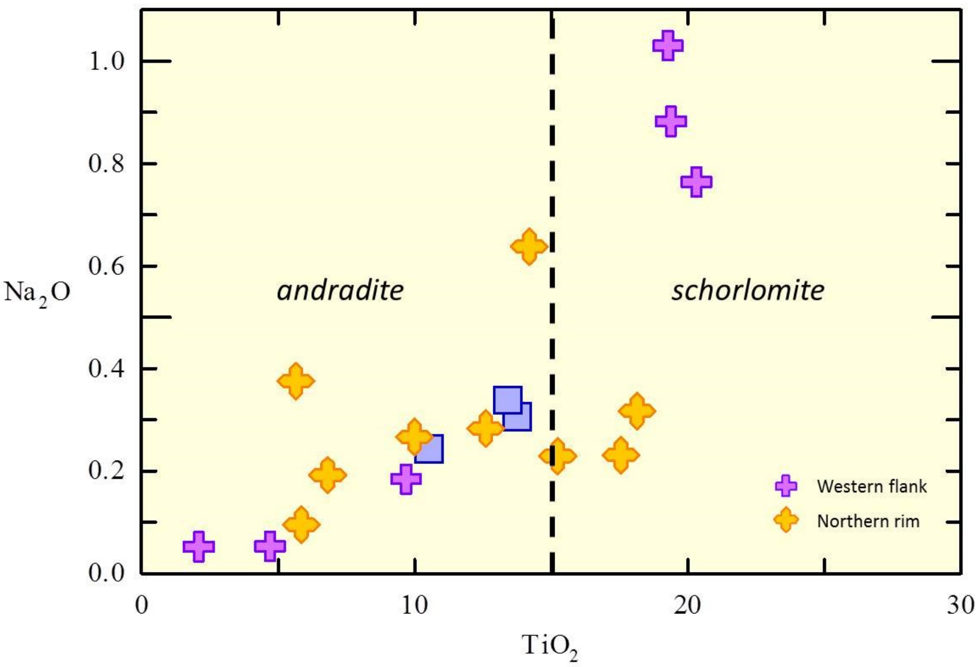

Figure 46. Andradite phenocryst comparison of Embagai to Bed III. Bed III andradites are not schormolite, but plot well with Embagai northern rim andradites.

6.1.3 Relationship to previously collected Embagai samples

Mollel's (2007) microprobe results from pyroxenes, nephelines, andradites, and oxides are compared with those of this thesis. The present study did not identify apatites, though rare feldspar, amphibole, melilite, perovskite, and sphene (titanite) was observed. It should be noted that Mollel's sampling consisted of fewer samples (n=4) versus this thesis (n=16) and did not cover some geographic areas visited in the current study.

Most Embagai samples that plot within the nephelinite/foidite region of the Total Alkali-Silica diagram are consistent with the results of Mollel (2007) (**Figure 47A**), though the addition of Na and K during zeolitic alteration could have affected the results for the most altered samples. In particular, the caldera floor and western flank samples most closely match Mollel's (2007) samples. Mollel's sample 03-EMB4 matches the caldera floor location of EM01 (**Figure 10b**). EMB-5 and EMB-6 overlap roughly with the eastern rim collection sites of this thesis EM07-09. EMB-3 overlaps with the northern rim samples EM10 and EM11.

6.1.4 Relationship to other NVH volcanoes

Previously published augite compositions from Ngorongoro, Sadiman, Lemagrut, Olmoti, and Oldeani volcanoes (Mollel et al., 2008, 2009, 2011) are plotted against Embagai to compare the volcanic centers **(Figure 48)**. Augite from the caldera floor of Embagai overlaps in part with Lemagrut. It should be noted, however, that Lemagrut is dated from 2.40 ± 0.01 to 2.22 ± 0.10 Ma (Mollel et al., 2011) much older than Embagai. Lemagrut is also comprised of olivine basalt (Pickering, 1964), a lava type not observed at Embagai. Some Sadiman augites plot close to those of Embagai's eastern rim. Oldeani, Ngorongoro, and Olmoti augites are compositionally distinct from Embagai augites.

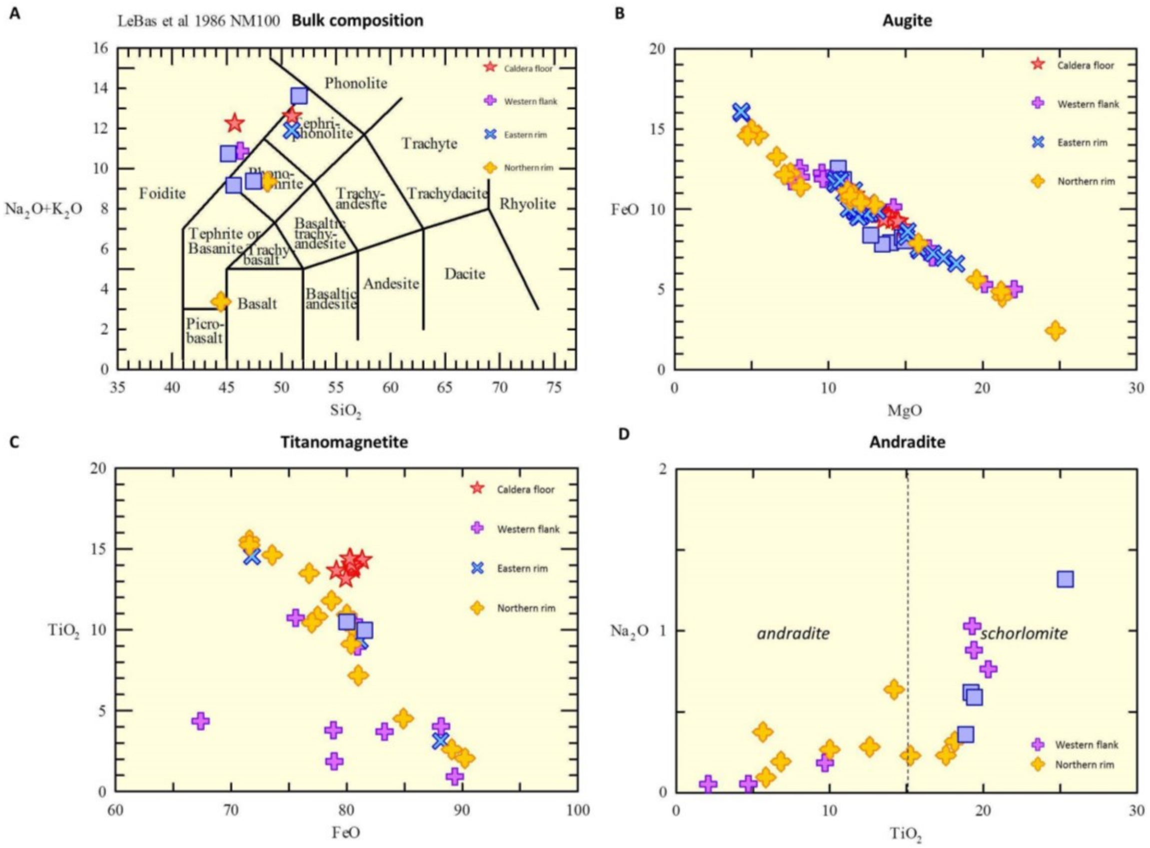

Figure 47. Comparisons to Mollel (2007) Embagai samples (blue squares). **(A)** Total alkali-silica diagram (bulk XRF geochemical data) with Mollel's (2007) samples added. The samples correspond well, with the exception of a northern rim, which plots near picro-basalt. Samples plot largely as foidite (nephelinite), phono-tephrite, and tephra-phonolite. **(B)** Comparison of Embagai augites (EPMA). Best correspondence for caldera floor samples. **(C)** Comparison of Embagai oxides (EPMA). Mollel's samples correspond with northern rim oxides. **(D)** Comparison of Embagai garnets (EPMA). Mollel's (2007) garnets correspond well with the general trend into titanian andradite.

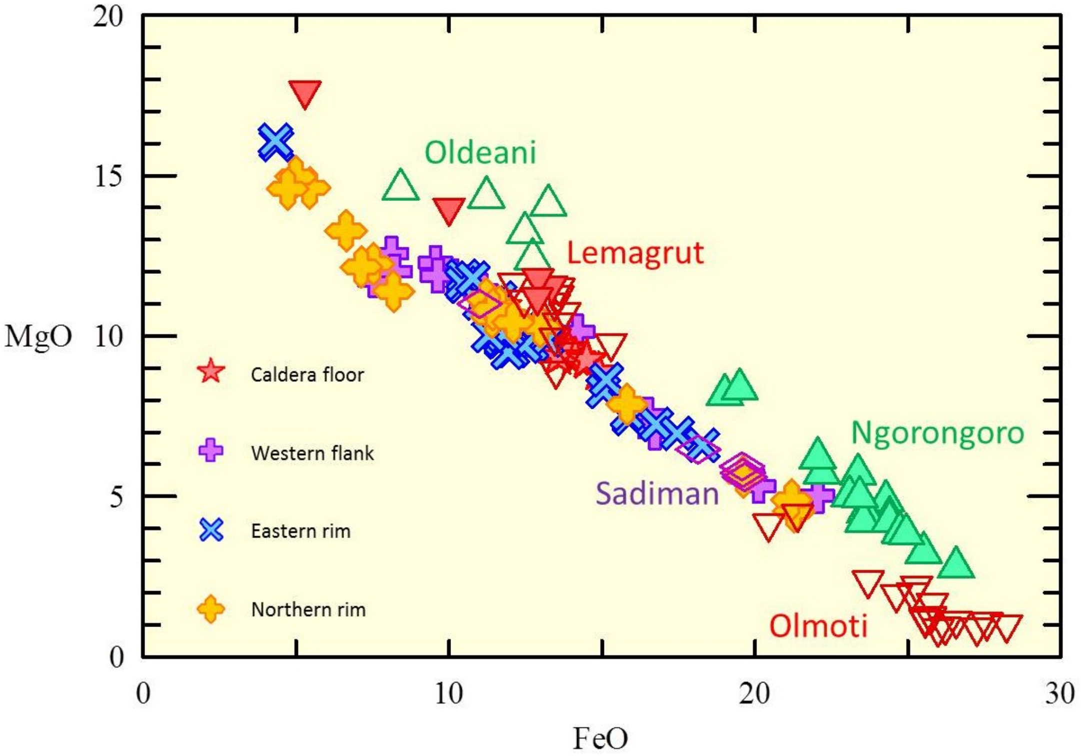

Figure 48. Embagai augite (FeO vs. MgO), compared to other NVH volcanic sources (Ngorongoro, Sadiman, Lemagrut, Olmoti, and Oldeani; data from Mollel et al., 2008, 2009, 2011) shows a decrease in Mg with an increase in Fe, as expected for this solid solution. Within the NVH, augites from the Embagai caldera floor are most compositionally similar to a second population from Olmoti and some from Lemagrut.

It would be helpful to have augite and other phenocryst compositions from the volcanic centers of Loolmalasin, Olsirwa and adjacent Loguwinywo, which have been less studied (e.g. Mollel and Swisher, 2012). They could be a better match for Olduvai Upper Bed II than is Embagai, while Embagai may be the volcanic source for the younger beds (i.e. Bed III).

6.1.5 Alteration at Embagai

Samples at Embagai represent several stages of alteration or contamination by calcite. Five samples with LOIs less than 7% represent the least altered. Four samples were moderately altered, with LOIs between 7-8%. Six samples were the most altered, with LOIs from 11-39%. The extremely high LOIs are for the calcite-rich samples, evident when plotted together with Ca (**Figure 49**).

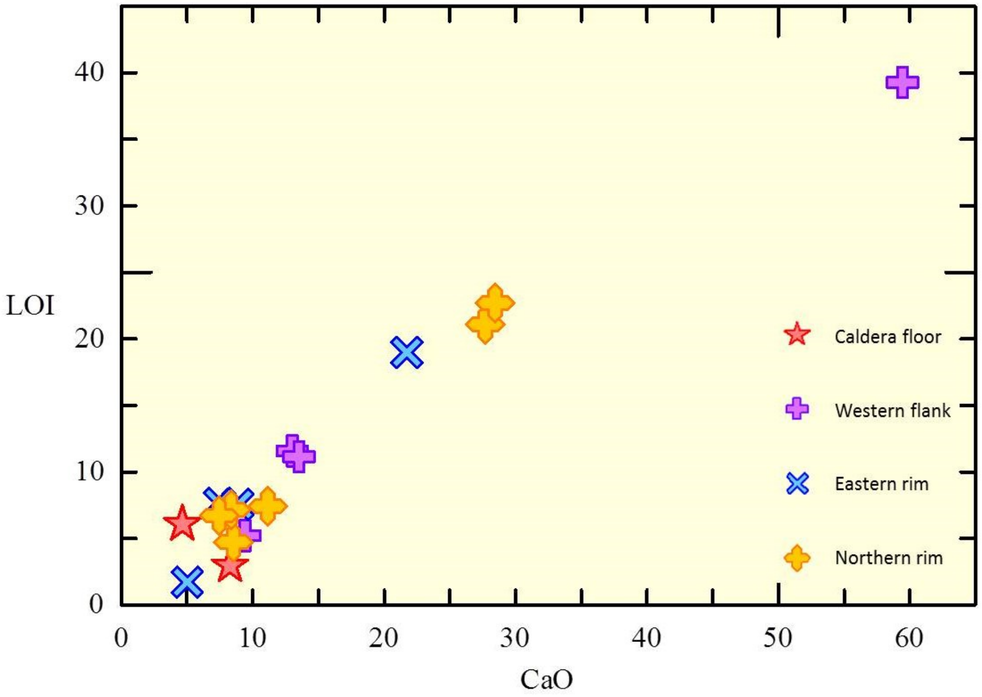

Figure 49. CaO vs. LOI for all Embagai samples, illustrating contamination by calcite. The least altered samples include those from the caldera floor.

The range, degree, and type of alteration can be illustrated by relative element mobility (**Figure 50**). For each location, the least altered sample (01 for caldera floor, 05 for western flank, 12 for northern rim, and T32 for eastern rim) was compared to the other samples from each setting. To test this, Zr was used first as the immobile element.

Note that the small amount of sample powdered in this study may affect whether the Zr concentration is representative of the bulk, since Zr is concentrated in accessory zircons and a larger sample size would thus be required to ensure a representative sample. Sample EM02 did not have any Zr, as it was mostly calcite. Other immobile elements, such as Ti and Al, do not vary as much as the more mobile alkali and alkali earth elements Ca, Na, and K. P also shows some variation away from the center line, though since P is mostly concentrated in the accessory mineral apatite, the small sample size analyzed may not have yielded P concentrations representative of the bulk. The plot indicates that Ca and Mn are enriched in most altered samples, especially in the eastern and northern rims, while Na, K, and P are typically depleted. The more altered of the two caldera floor samples appears to be depleted in all elements compared to the fresher sample; this is likely an artifact of non-representative Zr concentrations (or different initial Zr content) rather than an indication of alteration.

Immobile elements Ti and Al were then used for comparison. For Ti, the same general patterns of enrichment and depletion are observed. Ca is enriched in the most altered samples, while Mn and P are also enriched and Na and K are depleted (**Figure 51**). When Al is used as the immobile element, Ca and Mn are enriched and Na and K are depleted (**Figure 52**).

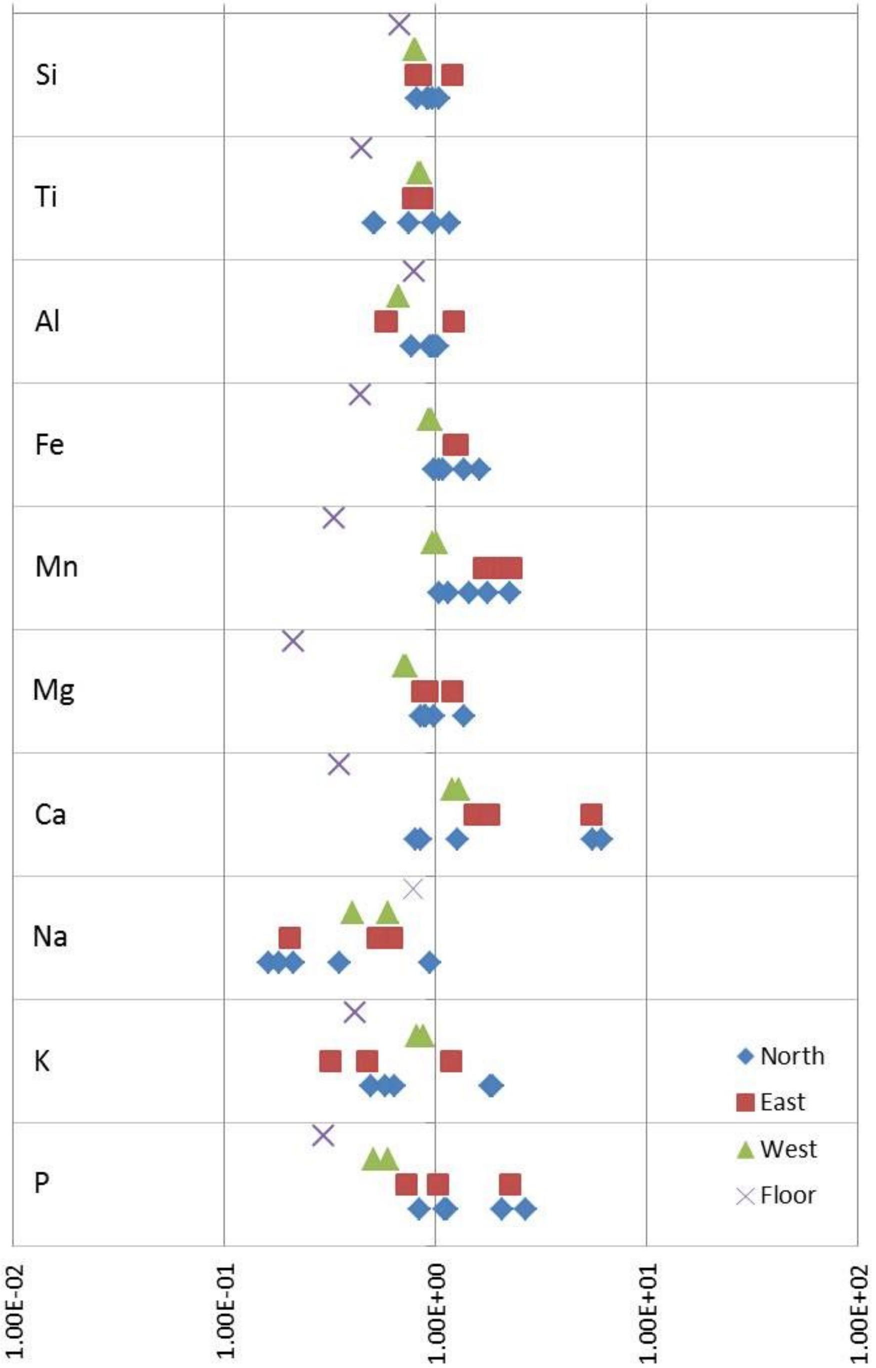

Figure 50. Relative element mobility of Embagai samples, nornalized to Zr. Each grouping represents one side of Embagai (i.e. caldera floor (X), western flank (green triangles), eastern rim (red squares), or northern rim (blue diamonds). Data is plotted against the least altered sample for each location. Scale is logarithmic. Based on this diagram, Ca is enriched in the most altered samples, whereas Na and K are depleted.

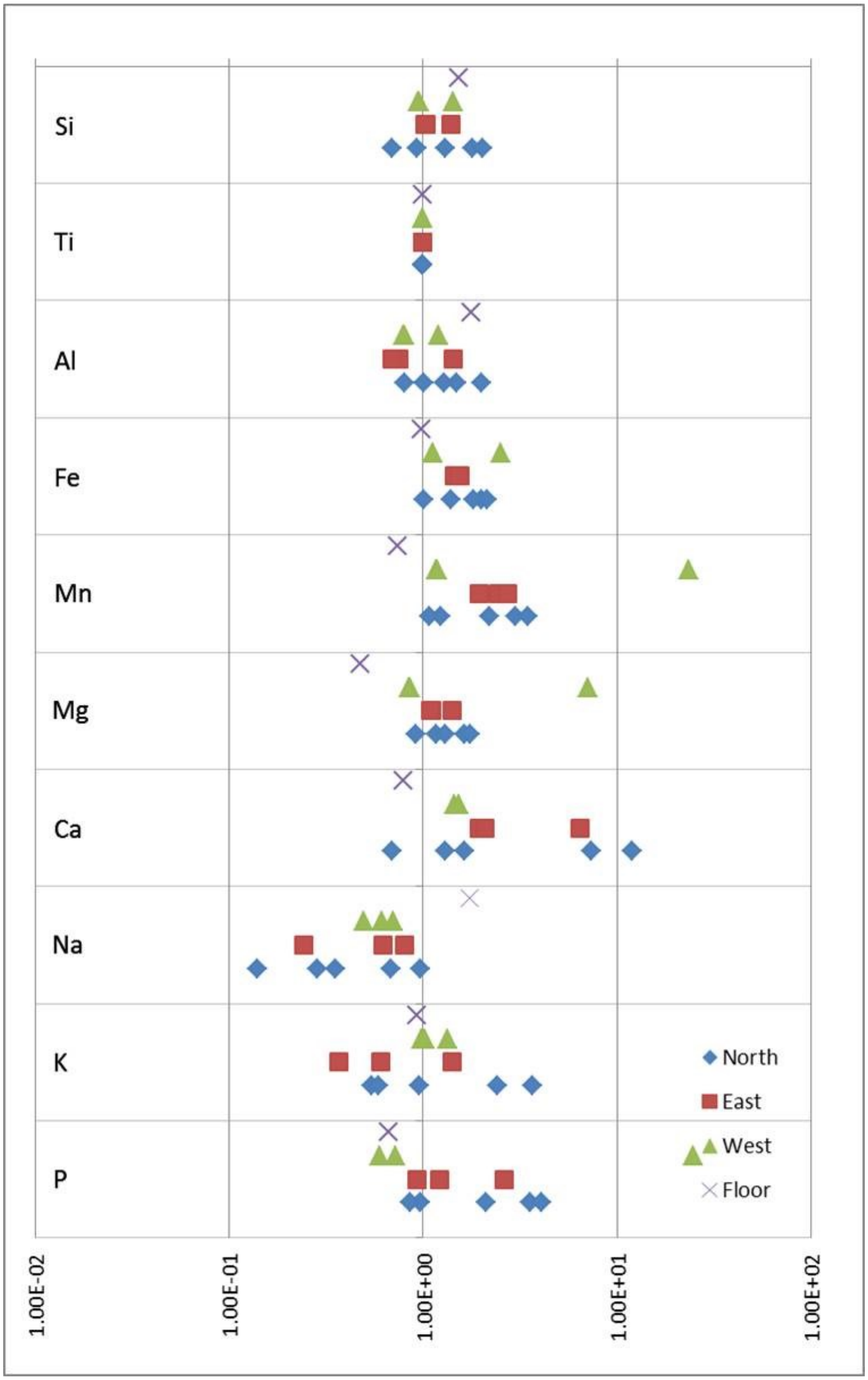

Figure 51. Relative element mobility of Embagai samples, normalized to Ti. Each grouping represents one side of Embagai (i.e. caldera floor (X), western flank (green triangles), eastern rim (red squares), and northern rim (blue diamonds). Data is plotted against the least altered sample for each location. Scale is logarithmic. Based on this diagram, Ca is enriched in the most altered samples, whereas Na and K are depleted.

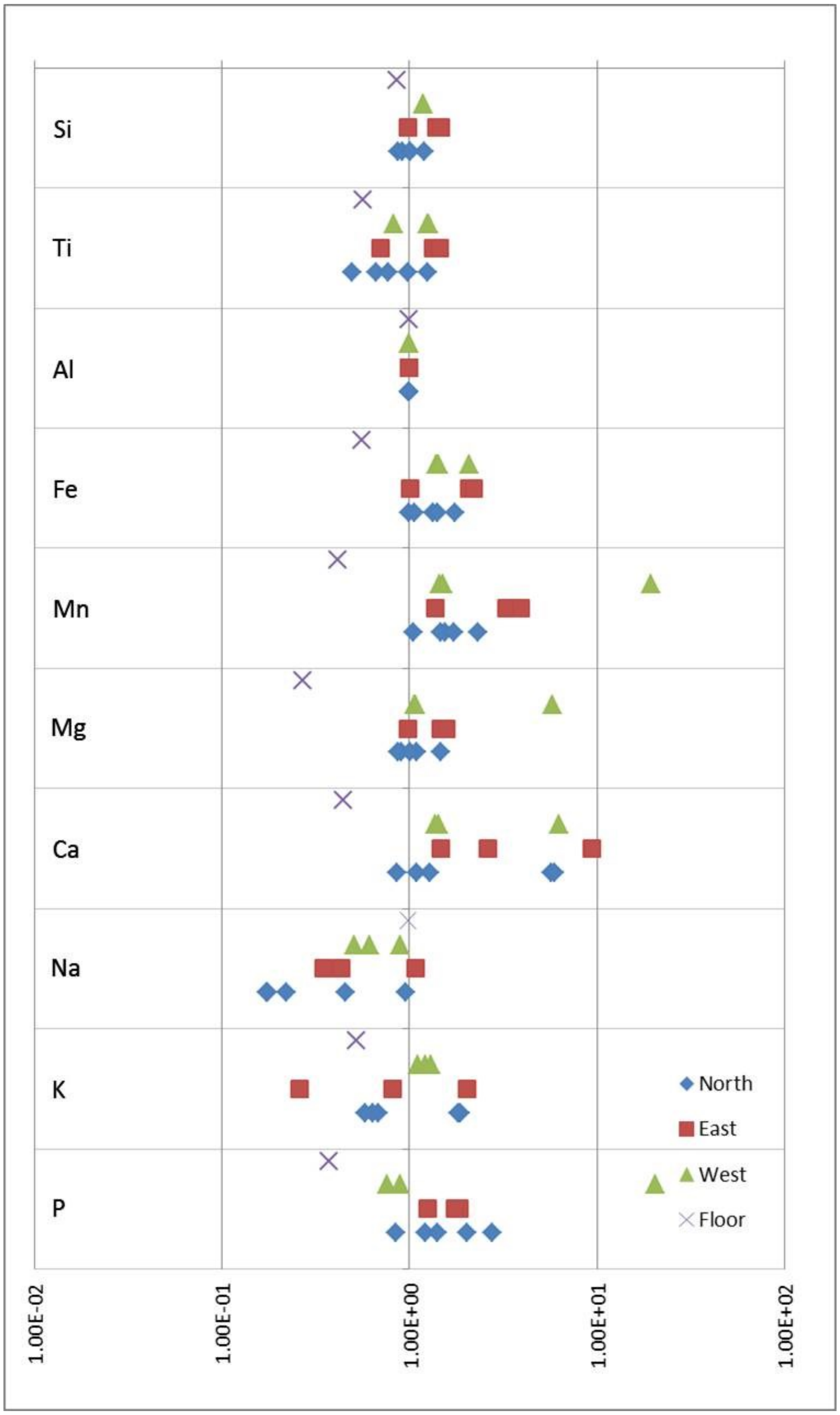

Figure 52. Relative element mobility of Embagai samples, normalized to Al. Each grouping represents one side of Embagai (i.e. caldera floor (X), western flank (green triangles), eastern rim (red squares), and northern rim (blue diamonds). Data is plotted against the least altered sample for each location. Scale is logarithmic. Based on this diagram, Ca and Mn are enriched in the most altered samples, particularly the western flank and eastern rim, whereas Na and K are depleted, with Na depleted the most on the northern rim.

6.2 Natron basin and its role in defining tephrostratigraphy in the Olduvai/NVH region

As noted earlier, the Natron basin is integral to constraining the timing of events in the greater NVH region. The proper placement of key lavas in the Peninj Group, in combination with radiometric dating, allows us to provide an improved stratigraphic and temporal framework for the hominid activities in the area.

The samples in this study show that bulk geochemistry alone cannot differentiate between units of similar composition or close proximity. Analysis of individual minerals can help distinguish between units, as shown by McHenry (2005, et al. 2008, 2009, 2012a, and 2012b). Establishing geochemical fingerprints works best with phenocrysts that are compositionally distinct between different units when fresh but do not change in composition during alteration.

It can be reasonably argued, however, that based on major and minor element compositional similarities between 10-T24 (Wa Mbugu) and 08-P13 (Wa Mbugu candidate), that 08-P13 is consistent with the Wa Mbugu. It should be noted that these correlations cannot be definitively confirmed using the major and minor element bulk composition alone, though further work involving trace element geochemistry, isotopes, paleomagnetism, and/or detailed microprobe analysis of their phenocrysts could provide the needed context.

6.2.1 Paleomagnetics of the Natron basin

Sample 10-T21's (Wa Mbugu candidate) Fisher mean direction of 173.7° declination (and well-defined demagnetization curves) strongly suggests that the sample has reversed polarity. A significant amount of Natural Remanent Magnetization (NRM) remained after 100 mT or 500°C, so it is possible that a second component exists, but there is no indication of overlapping coercivity or unblocking spectra. It is theoretically possible that the sample may have undergone self-reversal (acquisition of thermoremanent magnetization in a direction 180° from the natural field during cooling). This could be a result of two ferromagnetic minerals with different Curie temperatures growing in close proximity to each other, creating magnetostatic energy of interaction, though this process is rare and generally occurs in one percent of all samples (Cox et al., 1964). Without knowledge of the entire assemblage of magnetic minerals for the sample, it is difficult to determine whether this could create the observed reversed signal.

Since 10-T21 appears to be reversed (consistent with the Matuyama chron and the Hajaro Basalt) and not normal, as expected for the Wa Mbugu, this sample could be paleomagnetically consistent with the Hajaro lava. If so, this can allow for better correlation in the field between the Moinik Ramp and Peninj Type Section (Maritinane). However, this correlation is unlikely because sample 10-T21 was collected from the same unit as 11-T23 (**Figure 11B**), which is compositionally unlike the Hajaro from its type section (**Figure 37**), Sample 11-T23 is also not compositionally similar to any confirmed Wa Mbugu sample (10-T24 or 08-P13).

Assuming that the paleomagnetic interpretation for sample 10-T21 (reversed) is accurate, it cannot be confirmed as Wa Mbugu based on its polarity, and cannot be confirmed as Hajaro based on its geochemical composition. Thus, this sample could represent a new, previously undocumented lava flow. More field research would be required to determine its lateral extent, position within the Humbu and Moinik succession, and potential correlative units.

10-T25's (Wa Mbugu) Fisher mean direction of 97.6° declination (**Table 6, Figure 39**), indicates a transitional field. 10-T24 had a relatively low LOI (2.02%, **section 5.1**), which indicates only minor alteration. The paleomagnetic data derived from a split of this sample, 10-T25, would thus be expected to be minimally affected by alteration. Yet the behavior of sample 10-T25, with multiple components obtainable from demagnetization and highly irreversible $\chi(T)$ data, is consistent with post-emplacement alteration. Susceptibility was consistent with the presence of titanomaghemite in 10-T25 before heating (**Figure 40B**), and subsequent conversion of this titanomaghemite to magnetite and ilmenite upon heating suggests that the sample underwent low-temperature oxidation after emplacement. Partial or complete remagnetization of the sample could thus have occurred during alteration, resulting in the acquired values.

A transitional field for 10-T25 (Wa Mbugu) is in conflict with the previously established normal polarity for this unit (Isaac and Curtis, 1974). Isaac and Curtis (1974) had previously postulated that the succession of lavas could be interpreted in two chronological fashions, one where the Wa Mbugu corresponds to the Olduvai normal event (favored at the time) and a second where the Wa Mbugu corresponds to the Jaramillo normal event (1.053 ± 0.006 Ma to 0.986 ± 0.005 Ma, Singer et al., 1999).

There are several potential explanations for the apparent transitional field displayed by sample 10-T25. It should be noted that this study had a small sample size (three specimens from one sample), much smaller than a traditional paleomagnetic study, and it is impossible to accurately assess uncertainty and errors with only one sample. Structural rotation of the basalt unit in the field during cooling is possible, given the high level of rift-related faulting in the region (Luque et al., 2009). The quality of the sample collected and the method of collection are also important. Uncertainty based on orientation in the field could be up to 20°. Many lava samples from the Peninj area are zeolitized, which indicates significant post-displacement alteration, which may have affected the magnetic mineralogy (titanomagnetite altering to titanomaghemite). This is further reinforced by the samples' reaction to heat during thermal demagnetization. However, an adjacent sample from the same unit (10-T24) had a LOI of only 2.02%, which is not consistent with significant alteration.

Manega (1993) stated that the normal "events" observed by Thouveny and Taieb (1986, 1987) in the Moinik Formation located stratigraphically above the Wa Mbugu may have been the artifact of altered and oxidized sediments. Sediments that recorded normal polarity during the Brunhes normal event may have been affected by chemical remanent magnetization during diagenesis (Manega, 1993). This may be a concern for the Natron basin, as its local paleomagnetic record (Thouveny and Taieb, 1986) does not appear to match global records (Mankinen and Dalrymple, 1978; Berggren et al, 1995) and continues to yield inconsistent radiometric dates (Luque et al., 2009). Whether this is a factor in the recording of accurate paleomagnetic directions in the underlying Wa Mbugu basalt remains unclear.

Should the polarity of the Wa Mbugu (10-T25) obtained in this thesis be accurate, this could conflict with the paleomagnetic results of Isaac and Curtis (1974) and Thouveny and Taieb (1986, 1987), who found the unit to be of normal polarity. The "olivine basalt," later named Wa Mbugu basalt, was at first considered anomalous relative to the paleomagnetic chronology established at the time (K-Ar range of 1.4-1.6 Ma: Isaac, 1967). Although it was considered "stratigraphically consistent in relation to the other values," Isaac deduced that it was "higher than would be generally expected on archaeological and paleontological grounds" (i.e., based on the placement of the Acheulean stone industry and the *Australopithecus* mandible which are bracketed by the Intra-Moinik (~1.2-1.3 Ma) and the Sambu (~2.0 Ma) lavas above and below (**Figure 9**)). The latest ^{40}Ar/^{39}Ar date of 1.19 Ma (Deino, 2006) for the Wa Mbugu basalt places it within the range of two of three previous K-Ar dates: 1.0-1.5 and 0.96-1.21 Ma (Isaac and Curtis, 1974) and MacIntyre et al.'s (1974) K-Ar result of 0.91-1.21 Ma (indirect). If these dates constrain the Wa Mbugu to the short Cobb Mountain normal excursion (1.190 - 1.215 Ma, Channell et al., 2002; 1.12 ± 0.02 Ma; Mankinen et al., 1978), a true transitional polarity places it on the cusp of this brief event, but perhaps not within it. If the sample corresponds to the Jaramillo normal event, it is still possible to have a transitional polarity, since recent ^{40}Ar/^{39}Ar studies have identified transitional polarity sections and a brief reverse polarity section within the Jaramillo (Santa Rosa, Punaruu events: Singer et al., 1999; Guo et al., 2002).

Based on this sample alone, it is impossible to determine whether this transitional polarity (as opposed to the previously established normal polarity) is characteristic of the Wa Mbugu lava, and additional samples of established Wa Mbugu and potential Wa Mbugu candidates would be required for testing. Improved paleomagnetic studies, in addition to improved geochemical fingerprinting, could provide higher resolution stratigraphic and temporal constraints for units in this region.

7. CONCLUSIONS

7.1 Embagai

Embagai caldera is dominated by nephelinite at the locations sampled. Primary mineral assemblages include augite, rare amphibole, nepheline, titanomagnetite, andradite/schorlomite garnet, perovskite, and sphene. The secondary mineral assemblages include K-feldspar, calcite (a major source of contamination), and zeolites including phillipsite and chabazite.

Samples experienced a high level of alteration, as demonstrated by high LOI values. Relative element mobility indicates enrichment in Ca and depletion in Na for most altered samples. The presence of both lavas and tuffs indicates both explosive and effusive eruptions.

While phenocryst composition comparisons involving augite show some similarities between Upper Olduvai Bed II tephra and Embagai caldera, particularly for Embagai's northern rim and caldera floor, other minerals are less consistent. Feldspar is absent in most Embagai samples (which are instead dominated by nepheline), and are K-rich where present, making these lavas a poor match for the plagioclase and anorthoclase bearing tuffs of Olduvai Beds I and II.

Tuff IIIA (from Olduvai Bed III) is more mineralogically consistent with Embagai, with nepheline, Mg-rich augite, and rare feldspar. Titanomagnetites and andradites also show similar compositions for both Embagai and Tuff IIIA. With further geochemical analysis and improved dating of samples from this volcanic source, it may be possible to link Embagai to Olduvai Bed III.

7.2 Natron basin

Bulk geochemical data for the Natron basalts shows a spread of compositions. The presumed "Wa Mbugu/Humbu source" lava samples 07-P21 and 12-P3 are the most geochemically distinct of the basalts, and are thus most likely unrelated to the Wa Mbugu basalt. The source volcano is also compositionally distinct from the Hajaro lava.

This study of the Natron basin samples demonstrates that bulk major and minor elements alone are insufficient for geochemical fingerprinting of lavas. This is most evident in the case of samples 11-T23 and 11-T24, two lavas collected on the Moinik ramp. While they are geochemically similar, they are separated by tens of meters of continuous section. A detailed study of their phenocryst mineralogy, together with bulk trace element and isotopic analysis, could better differentiate their compositions.

The reversed polarity of Wa Mbugu candidate sample 10-T21 does not match the expected normal polarity of the unit. This unit is also unlikely to be the Hajaro basalt, for while this unit has reversed polarity its geochemical composition does not match the definitive Hajaro samples (07-P3 and 11-T17). This leaves the possibility that sample 10-T21 is neither Wa Mbugu nor Hajaro, and represents different lavas entirely.

The definitive Wa Mbugu sample (10-T25) appears to record a transitional direction rather than the expected normal polarity, which may be due to rotation in the unit due to rift-related faulting or post-emplacement alteration of the lava. It is also possible that there is a brief transitional period within one the normal events to which the Wa Mbugu is being attributed (e.g. the Jaramillo). If these results are accurate, it is possible that the paleomagnetic record for the Natron basin may need to be revised, based on more recent dating results by Deino (2006) and future studies.

8. REFERENCES

Ashley, G.M., Dominguez-Rodrigo, M., Bunn, H.T., Mabulla, A.Z.P., and Baquedano, E., 2010. Sedimentary geology and human origins: A fresh look at Olduvai Gorge, Tanzania. *Journal of Sedimentary Research*, v. 80: 703-709. doi: 10.2110/jsr.2010.066

Berggren, W.A., Kent, D., Swisher III, C., & Aubry, M.-P., 1995b. A Revised Cenozoic Geochronology and Chronostratigraphy. In W. Berggren, D. Kent, M.-P. Aubry, & J. Hardenbol (Eds.), *Geochronology Time Scales and global Stratigraphic Correlation* (pp. 129–212). Tulsa, Oklahoma: SEPM.

Channell, J.E.T., Mazaud, A., Sullivan, P., Turner, S., and Raymo, M. E., 2002. Geomagnetic excursions and paleointensities in the Matuyama Chron at Ocean Drilling Program Sites 983 and 984 (Iceland Basin). *Journal of Geophysical Research*, Vol. 107, No. B6, 2114. doi: 10.1029/2001JB000491

Cox. A.V., Doell, R.R., and Dalrymple, G.B., 1964. Reversals of the Earth's magnetic field. *Science* 144: 1537-1543.

Curtis, G.H., 1967. Notes on some Miocene to Pleistocene potassium/argon results. *Background to Evolution in Africa*. Edit. Bishop, W.W and J.D. Clark. University of Chicago Press, Chicago, 365-369.

Curtis, G.H. and Hay, R.L., 1972. Further geological studies and K/Ar dating at Olduvai Gorge and Ngorongoro crater: In Bishop, W.W. and Miller, J.A. (eds.) *Calibration of Hominid Evolution.* Scottish Academic Press, Edinburgh, 289-302.

Dawson, J.B., 1962. The Geology of Oldoinyo Lengai. *Bull. Volcanology* 24: 349-387.

Dawson, J.B., 1964. Carbonatitic volcanic ashes in Northern Tanganyika. *Bull. Volcanology* 27: 81-92.

Dawson, J.B., 1964b. Monduli. Tanzania Geological Survey Quarter Degree Sheet 54.

Dawson, J.B. and Powell, D.G., 1969. The Natron-Engaruka Explosion Crater area, Northern Tanzania. *Bull. Volcanology* 33: 791-817.

Dawson, J.B., 1992. Neogene tectonics and volcanicity in the North Tanzania sector of the Gregory Rift Valley: contrasts with the Kenya sector. *Tectonophysics* 204: 81-92.

Dawson, J.B., 2008. The Gregory Rift Valley and Neogene-Recent Volcanoes of Northern Tanzania. *Geological Society, London, Memoirs*, 33, pp. 102.

Deer, W.A., Howie, R.A. and Zussman, J., 1992. *An Introduction to Rock-Forming Minerals*: 2nd ed. Pearson Education Limited, Harlow, London.

Deino, A.L., Domínguez-Rodrigo, M., Luque, L., 2006. ^{40}Ar/^{39}Ar dating of the Pleistocene Peninj Group, Lake Natron, Tanzania. *Eos, Transactions,* American Geophysical Union 87 (52) (Fall Meeting Supplement, Abstract V53C-1771).

Deino, A.L., 2012. ^{40}Ar/^{39}Ar dating of Bed I, Olduvai Gorge, Tanzania, and the chronology of early Pleistocene climate change. *Journal of Human Evolution* 63: 251-273.

de la Torre, I., McHenry, L.J., Njau, J., and Pante, M., 2012. *The Origins of the Acheulean at Olduvai Gorge (Tanzania): A New Paleoanthropological Project in East Africa*. Archaeology International No. 15, 2011-2012, 89-98. doi:10.5334/ai.1505

Doell, R.R. and Dalrymple, B.G., 1966. Geomagnetic polarity epochs: a new polarity event and the age of the Brunhes-Matuyama boundary. *Science* 152: 1,060-1,061.

Evans, A.L., Fairhead, J.D. and Mitchell, J.G., 1971. Potassium-argon ages from the volcanic province of northern Tanzania. *Nature* 229: 19-20.

Fabian, K., Shcherbakov, V. P. & McEnroe, S. A., 2013. Measuring the Curie temperature. *Geochem. Geophys. Geosys*. 14: 1–15.

Foster, A., Ebinger, C., Mbede, E., Rex, D., 1997. Tectonic development of the northern sector of the East African Rift System. *Journal of the Geological Society, London* 154: 689–700.

Grommé, C.S. and Hay, R.L., 1963. Magnetization of basalt of bed 1, Olduvai Gorge, Tanganyika. *Nature* 200: 560–561.

Grommé, C.S., Reilly, T.A., Mussett, A.E. and Hay, R.L., 1970. Paleaomagnetism and potassium-argon ages of volcanic rocks of Ngorongoro caldera, Tanzania: *Geophysical Journal of the Royal Astronomical Society* 22: 101-115.

Guest, N.J., James, T.C., Pickering, R., and Dawson, J.B., 1961. *Angeta Salei*. Tanzania Geological Survey Quarter Degree Sheet 39.

Guo, B., Zhu, R., Florindo, F., Ding, Z., and Sun, S., 2002. A short, reverse polarity interval within the Jaramillo subchron: Evidence from the Jingbian section, northern Chinese Loess Plateau. *Jour. Geophys. Research* 107, no. B6, doi:10.1029/2001JB000706

Hay, R.L., 1976. *Geology of the Olduvai Gorge: A Study of Sedimentation in a Semiarid Basin*. University of California Press, Berkeley, pp.203.

Hay, R.L., 1978. Melilitite-carbonatite tuffs in the Laetolil Beds of Tanzania. *Contributions to Mineralogy and Petrology* 67: 357-367.

Hay, R.L. and Kyser, T.K., 2001. Chemical sedimentology and paleoenvironmental history of Lake Olduvai, a Pliocene lake in Northern Tanzania. *GSA Bulletin*; December 2001; v. 113; no. 12; p. 1505–1521. doi: 10.1130/0016-7606

Howell, F.C., 1972. Pliocene/Pleistocene hominidae in eastern Africa: absolute and relative ages. In: Bishop, W.W., Miller, J.A. (Eds.), *Calibration of hominoid evolution.* Scottish Academic Press, Edinburgh, pp. 331–368.

Isaac, G.L., 1965. The stratigraphy of the Peninj Beds and the provenance of the Natron Australopithecine mandible. *Quaternaria* 7: 101–130.

Isaac, G.L., 1967. The stratigraphy of the Peninj Group- early Middle Pleistocene Formations west of Lake Natron, Tanzania. In: Bishop, W.W., Clark, J.D. (Eds.), *Background to Evolution in Africa*. University of Chicago Press, Chicago, pp. 119–257.

Isaac, G.L., Curtis, G.H., 1974. Age of Early Acheulian industries from the Peninj Group, Tanzania. *Nature* 249: 624–627.

Kapitsa, A.P., 1968. Preliminary report of the Soviet East African expedition of the Academy of Sciences of the USSR in 1967. Moscow. Unpublished. 62 pp.

Keller, J., Zaitsev, A.N., Wiedenmann, D., 2006. Primary magmas at Oldoinyo Lengai: The role of olivine melilitites. *Lithos* 91: 150-172.

Keller, J., et al, 2010. Fundamental changes in the activity of the natrocarbonatite volcano Oldoinyo Lengai, Tanzania. *Bull. Volcanology* 72: 893-912.

Kirschvink, J. L., 1980. The least-squares line and plane and the analysis of palaeomagnetic data, *Geophys. J. R. Astr. Soc.*, *62*: 699-718.

Klein, R.G, 2009. *The Human Career: Human Biological and Cultural Origins*. 3rd ed. University of Chicago Press, Chicago, 157-160.

Leakey, L.S.B. and Leakey, M.D., 1964. Recent discoveries of fossil hominids in Tanganyika at Olduvai and near Lake Natron. *Nature* 209: 3-9.

Le Bas, M.J., Le Maitre, R.W., Streckeisen, A., Zanettin, B., and IUGS Subcommission on the Systematics of Igneous Rocks, 1986. A Chemical Classification of Volcanic Rocks Based on the Total Alkali-Silica Diagram. *Journal of Petrology* 27 (3): 745-750. doi: 10.1093/petrology/27.3.745

Le Maitre, R.W. (Ed.), Streckeisen, A., Zanettin, B., Le Bas, M.J., Bonin, B., Bateman, P., Bellieni, G., Dudek, A., Efremova, S., Keller, J., Lameyre, J., Sabine, P.A., Schmid, R., Sorensen, H., and Woolley, A.R., 2002. *Igneous Rocks: A Classification and Glossary of Terms. Recommendations of the International Union of Geological Sciences Subcommission on the Systematics of Igneous Rocks*. Cambridge University Press.

Luque, L. Alcalá, L., and Domínguez-Rodrigo, M., 2009. The Peninj Group: Tectonics, volcanism, and sedimentary paleoenvironments during the lower Pleistocene in the Lake Natron Basin (Tanzania). *Peninj: A Research Project on Human Origins (1995-2005).* 15-48.

MacIntyre, R.M., Mitchell, J.G., Dawson, J.B., 1974. Age of the fault movements in the Tanzanian sector of the East African rift system. *Nature* 247: 354–356.

Mana, S., Furman, T., Carr, M.J., Mollel, G.F., Mortlock, R.A., Feigenson, M.D., Turrin, B.D., and Swisher, C. III, 2012. Geochronology and geochemistry of the Essimingor volcano: Melting of metasomatized lithospheric mantle beneath the North Tanzanian Divergence zone (East African Rift). *Lithos* 155: 310-325.

Manega, P.C., 1993. Geochronology, geochemistry and isotopic study of the Plio-Pleistocene hominid sites and the Ngorongoro volcanic highland in northern Tanzania. Ph.D. Thesis, University of Colorado, Boulder, Colorado, pp. 382 + xx.

Mankinen, E. A., and Dalrymple, G. B., 1978. Revised geomagnetic polarity time scale for
the interval 0 to 5 m.y. B.P.: *Journal of Geophysical Research* 84: 615-626.

Mankinen, E. A., Donnelly, J. M., and Grommé, C. S., 1978. Geomagnetic polarity event recorded at 1.1 m.y. B.P. on Cobb Mountain, Clear Lake volcanic field, California. *Geology* 6: 653-656. doi: 10.1130/0091-7613

McHenry, H.M., Brown, C.C., and McHenry, L.J, 2007. Fossil hominin ulnae and the forelimb of *Paranthropus*. *American Journal of Physical Anthropology* 134: 209-218.

McHenry, L.J., 2005. Phenocryst composition as a tool for correlating fresh and altered tephra, Bed I, Olduvai Gorge, Tanzania. *Stratigraphy* 2, 101–115.

McHenry, L.J., Mollel, G.M., and Swisher, C.C. III, 2008. Compositional and textural correlations between Olduvai Gorge Bed I tephra and volcanic sources in the Ngorongoro Volcanic Highlands, Tanzania. *Quatern Int* 178: 306-319. doi:10.1016/j.quaint.2007.01.004

McHenry, L.J., 2009. High-resolution tephrostratigraphy of Bed II, Olduvai Gorge: Reconstructing landscapes at the Oldowan-Acheulean transition. Geo. Soc. Amer. *Abstracts with Programs*, Vol. 41, No. 7, p. 612.

McHenry, L.J., Luque, L.J., Gomez, J.A., and Diez-Martin, F., 2011. Promises and pitfalls for characterizing and correlating the zeolitically altered tephra of the Pleistocene Peninj Group, Tanzania. *Quaternary Research* 75: 708-720.

McHenry, L.J., 2011. Geochemistry and mineralogy of Laetoli area tuffs: Lower Laetolil through Naibadad Beds. In: Harrison, T. (Ed.) *Paleontology and Geology of Laetoli, Tanzania: Human Evolution in Context. Volume 1: Geology, Geochronology, Paleoecology and Paleoenvironment*. Springer series Vertebrate Paleobiology and Paleoanthropology. 121-141.

McHenry, L.J., 2012a. A revised stratigraphic framework for Olduvai Gorge Bed I based on tuff geochemistry. *Journal of Human Evolution* 63: 284-299.

McHenry, L.J., 2012b. Evolving tephra compositions over time at Olduvai Gorge: Implications for a changing volcanic source. Abstracts of the Paleoanthropology Society 2012 Meeting. *PaleoAnthropology* 2012:A1-A39.

McHenry, L.J. and Greenwood, S.M., 2012. Volcanic sources for Olduvai Gorge tuffs: Implications for geochronology and the effect of volcanism on hominin paleoenvironments. Geo. Soc. Amer. *Abstracts with Programs*, Vol. 44, No. 7, p. 194.

McHenry, L.J., Stollhofen, H., Stanistreet, I.G., 2013 in press. Use of single-grain geochemistry of cryptic tuffs and volcaniclastic sandstones improves the tephrostratigraphic framework of Olduvai Gorge, Tanzania. *Quaternary Research*.

Mollel, G.F., 2002. Petrology and geochemistry of the southeastern Ngorongoro Volcanic Highland; and Contribution to "Sourcing" of Stone Tools at Olduvai Gorge, Tanzania. M.S. Thesis, Rutgers University, New Brunswick, pp. 121 + xiii.

Mollel, G.F., 2007. Petrochemistry and geochronology of Ngorongoro Volcanic Highland Complex (NVHC) and its relationship to Laetoli and Olduvai Gorge, Tanzania. Ph.D. Dissertation, Rutgers University, New Brunswick, pp. 233 + xxi.

Mollel, G.F., Swisher, C.C. III, Feigenson, M.D., Carr, M.J., 2008. Geochemical evolution of Ngorongoro Caldera, Northern Tanzania: Implications for crust–magma interaction. *Earth Planet Sc Lett* 271: 337-347.

Mollel, G.F., Swisher, C.C. III, McHenry, L.J., Feigenson, M.D., Carr, M.J., 2009. Petrogenesis of basalt-trachyte lavas from Olmoti Crater, Tanzania. *J Afr Earth Sci* 54: 127-143. doi: 10.1016/j.jafrearsci.2009.03.008

Mollel, G.F., Swisher, C.C. III, Feigenson, M.D., Carr, M.J., 2011. Petrology, geochemistry and age of Satiman, Lemagurut and Oldeani: Sources of the volcanic deposits of the Laetoli area. In: Harrison, T. (Ed.) *Paleontology and Geology of Laetoli, Tanzania: Human Evolution in Context. Volume 1: Geology, Geochronology, Paleoecology and Paleoenvironment*. Springer series Vertebrate Paleobiology and Paleoanthropology. 99-119.

Mollel, G.F. and Swisher. C.C. III, 2012. The Ngorongoro Volcanic Highland and its relationships to volcanic deposits at Olduvai Gorge and East African Rift volcanism. *Journal of Human Evolution* 63: 274-283.

Orridge, G.R., 1965. *Mbulu*. Tanzania Mineral Resources Division Quarter Degree Sheet 69.

Paslick, C., Halliday, A., James, D., Dawson, J. B., 1995. Enrichment of the continental lithosphere by OIB melts: Isotopic evidence from the volcanic province of Northern Tanzania. *Earth and Planetary Science Letters*, 130: 109-126.

Petersen, N., and Bleil, U., 1982. Curie temperature, in Landolt-Börnstein: Numerical Data and Functional Relationships in Science and Technology edited by G. Angerheiser, Springer Materials: The Landolt-Börnstein database. doi: 10.1007/10201909_76

Pickering, R., 1964. *Endulen*. Tanzania Geological Survey Quarter Degree Sheet 52.

Reck, H., 1914a. First preliminary announcements about the discovery of a fossil human skeleton from Central Africa. *Proceedings of the Society of the Friends of Berlin*, 3: 81–95.

Singer, B. S., K. Hoffman, A. Chauvin, R. S. Coe, and M. S. Pringle, 1999. Dating transitionally magnetized lavas of the late Matuyama Chron: Toward a new 40Ar/39Ar timescale of reversals and events, *J. Geophys. Res.* 104: 679– 693.

Tauxe, L., 1998. *Paleomagnetic Principles and Practice*. Dordrecht: Kluwer Academic Publishers.

Tauxe, L., 2014. *Essentials of Paleomagnetism: Third Web Edition*. Updated May 7, 2014.

Tamrat, E., Thouveny, N., Taieb, M., and Opdyke, N.D., 1995. Revised magnetostratigraphy of the Plio-Pleistocene sequence of the Olduvai Formation (Tanzania). *Palaeogeography, Palaeoclimatology, Palaeoecology* 114: 273-283.

Thouveny, N. and Taieb, M., 1986. Preliminary magnetostratigraphic record of Pleistocene deposits, Lake Natron Basin, Tanzania. In: Frostick, L.E., et al. (Ed.), *Sedimentation in the African Rifts*, 25. Geological Society Special Publication, pp. 331–336.

Thouveny, N., Taieb, M., 1987. Etude paleomagnetique des formations du Plio-Pleistocene de la region de Peninj (Ouest du lac Natron, Tanzanie). Sciences Geologiques (Bulletin) 40: 50–62.

Walter, R.C., Manega, P.C. and Hay, R.L., 1992. Tephrochronology of Bed I, Olduvai Gorge: An application of laser-fusion Ar/Ar dating to calibrating biological and climatic change. *Quat. Int.*, 13/14: 37-46.

Wood, B.A. and Constantino, P.J., 2007. Paranthropus boisei: Fifty Years of Evidence and Analysis. *Yearbook of Physical Anthropology* 50: 106-132.

Zijderveld, J.D.A., 1967. AC demagnetization of rocks: analysis of results. In: Collinson, D.W., Creer, K.M. and Runcorn, S.K. (eds.) *Methods in Paleomagnetism*. Elsevier, Amsterdam, pp. 254-86.

APPENDIX A: EMBAGAI AUGITE MICROPROBE DATA

Sample	SiO_2	TiO_2	Al_2O_3	FeO	MnO	MgO	CaO	Na_2O	SUM
12EM02	50.58	0.88	0.82	20.12	0.77	5.32	17.86	3.35	99.70
	49.81	1.28	3.36	8.12	0.13	12.56	23.87	0.87	100.04
	45.64	2.87	7.58	7.57	0.15	11.72	24.02	0.70	100.25
12EM03	51.39	1.16	1.45	10.85	0.37	11.46	22.82	1.32	100.83
	50.09	0.77	1.31	16.73	1.02	6.99	20.81	1.89	99.71
	49.78	1.99	0.76	14.21	0.42	10.13	19.19	2.84	99.34
	51.29	1.18	1.24	13.37	0.97	9.74	20.08	1.91	100.03
	52.26	1.11	0.26	13.04	0.57	9.89	20.27	2.55	99.93
	52.00	1.62	0.41	12.68	0.42	9.88	19.15	3.18	99.33
	46.74	2.60	5.16	8.22	0.17	12.00	23.46	0.69	99.08
	52.15	1.22	0.92	10.11	0.38	11.87	22.05	1.45	100.15
12EM04	51.59	1.00	1.66	9.57	0.28	12.27	23.20	1.03	100.57
	50.26	2.86	0.81	16.49	0.47	7.55	17.09	4.12	99.65
	52.16	0.97	1.12	9.63	0.33	11.88	23.16	1.11	100.36
	52.99	0.78	0.70	10.69	0.36	11.67	22.68	1.38	101.26
	51.81	1.06	0.99	11.06	0.34	11.42	22.35	1.45	100.47
	51.15	1.51	0.65	22.05	0.44	5.02	11.04	7.10	99.00
12EM06	51.60	1.29	1.01	13.37	0.64	9.68	20.46	1.96	100.11
	51.43	1.34	0.75	14.89	0.58	8.87	20.23	2.50	100.59
	51.85	1.01	0.60	13.74	0.63	9.62	21.22	2.10	100.77
	51.84	1.02	0.65	13.51	0.50	9.69	20.89	2.00	100.09
	51.19	1.29	0.98	13.75	0.54	9.45	20.19	2.21	99.61
	51.62	1.45	1.50	11.71	0.45	10.90	21.50	1.86	101.00
	51.10	1.09	0.74	13.92	0.63	9.53	20.70	2.09	99.80
	51.82	1.08	0.60	13.31	0.55	9.71	21.04	1.97	100.08
	51.53	1.18	0.68	14.13	0.50	9.33	20.90	2.04	100.29
	51.52	1.55	0.92	13.57	0.49	9.35	20.38	2.21	100.00
	51.25	1.49	0.85	14.53	0.56	9.23	20.46	2.30	100.67
	51.07	1.55	1.07	14.50	0.52	9.25	20.33	2.39	100.68

Sample	SiO_2	TiO_2	Al_2O_3	FeO	MnO	MgO	CaO	Na_2O	SUM
12EM09	50.99	0.53	1.31	15.05	0.46	8.27	20.93	1.94	99.47
	48.74	0.97	2.01	15.90	0.46	7.43	20.34	2.28	98.14
	51.41	0.86	0.87	15.15	0.41	8.64	19.60	2.81	99.73
	50.38	0.51	1.60	16.78	0.56	7.24	19.59	2.61	99.28
	51.83	0.80	0.91	17.46	0.52	6.96	18.12	3.44	100.04
	51.45	0.45	0.93	18.29	0.52	6.60	18.30	3.49	100.02
	51.16	0.83	1.94	12.69	0.49	9.73	21.35	1.65	99.85
	51.04	0.74	0.94	15.84	0.56	7.58	20.41	2.13	99.26
	53.34	0.30	0.20	11.66	0.62	11.18	21.34	2.07	100.71
	52.33	0.59	0.43	13.20	0.35	9.88	20.35	2.35	99.48
13T32	51.68	1.60	1.80	10.47	0.36	11.57	21.99	1.19	100.65
	50.14	2.06	3.53	12.08	0.38	9.54	19.64	2.19	99.61
	50.44	2.21	3.31	12.47	0.27	9.68	19.80	2.22	100.34
	51.78	1.44	1.37	10.46	0.42	11.86	22.33	1.18	100.88
	50.23	1.77	2.96	11.52	0.40	10.12	20.48	1.85	99.39
	51.47	1.51	1.57	10.51	0.31	11.55	21.98	1.17	100.07
	50.87	1.63	2.78	11.58	0.38	10.50	20.68	1.83	100.28
	51.87	1.45	1.60	10.41	0.39	11.64	22.01	1.20	100.51
	50.38	2.12	3.11	11.77	0.42	9.83	20.12	2.10	99.87
	50.05	2.06	3.31	11.71	0.30	9.82	20.09	2.18	99.56
	51.38	1.60	1.76	11.01	0.37	11.03	21.67	1.43	100.30
	50.54	2.12	3.33	11.71	0.44	9.91	20.13	2.13	100.35
	51.83	1.36	1.50	10.78	0.40	11.80	21.79	1.14	100.56
	50.01	2.05	3.46	11.93	0.35	9.48	20.12	2.24	99.65
	50.32	1.89	3.08	11.80	0.44	10.05	20.75	1.98	100.31
	50.85	1.38	2.26	11.54	0.44	10.60	21.21	1.66	99.89
	49.89	2.67	3.48	11.30	0.32	10.02	20.28	1.92	99.90
	51.16	1.59	2.02	11.54	0.34	10.79	21.29	1.60	100.24
	51.30	0.68	2.40	12.60	0.52	10.42	21.73	0.91	100.55
	53.95	0.71	1.74	4.36	0.12	15.97	24.25	0.36	101.70
	53.56	0.66	1.74	4.32	0.10	16.10	23.98	0.31	100.92

Sample	SiO_2	TiO_2	Al_2O_3	FeO	MnO	MgO	CaO	Na_2O	SUM
12EM11	50.73	0.26	0.75	19.62	0.73	5.61	19.85	2.39	99.93
	50.26	0.38	0.96	21.27	0.71	4.53	19.18	2.86	100.14
	50.88	0.52	0.72	21.21	0.75	4.89	17.72	3.57	100.25
	49.69	1.23	2.05	15.82	0.51	7.87	20.41	2.16	99.75
	49.87	1.92	1.95	11.40	0.36	10.59	22.83	1.09	100.04
	50.61	1.77	1.60	11.41	0.42	10.93	23.20	0.99	100.93
	50.51	1.90	1.48	12.99	0.56	10.29	22.10	1.05	100.90
	50.98	1.53	1.26	12.04	0.46	10.58	22.76	1.20	100.81
	51.24	1.41	1.45	11.23	0.43	11.16	23.09	1.06	101.07
	50.48	1.68	1.92	11.63	0.39	10.91	22.80	1.24	101.04
	50.77	1.55	1.35	11.43	0.36	10.82	22.93	1.12	100.35
	50.72	1.86	1.68	12.09	0.43	10.43	22.83	1.20	101.24
12EM15	52.67	0.34	0.67	24.73	0.41	2.43	5.84	10.23	97.32
	46.31	2.53	6.50	7.53	0.10	12.25	23.93	0.65	99.81
	50.56	2.36	3.39	5.45	0.08	14.61	24.68	0.52	101.65
	51.07	1.92	2.75	5.00	0.04	14.96	24.59	0.41	100.76
	49.55	2.32	3.31	4.73	0.06	14.59	24.16	0.48	99.19
	44.55	3.33	7.84	8.18	0.11	11.39	23.72	0.66	99.78
	50.49	1.67	3.70	6.64	0.16	13.28	24.67	0.54	101.14
	47.21	2.17	5.45	7.13	0.11	12.15	24.12	0.66	98.99

APPENDIX B: EMBAGAI FELDSPAR MICROPROBE DATA

Sample	SiO_2	Al_2O_3	FeO	CaO	Na_2O	K_2O	BaO	SUM
12EM03	64.47	18.31	0.98	0.15	1.12	14.19	1.07	100.29
12EM07	64.66	18.24	0.40	n.d.	0.29	15.93	0.27	99.78
	62.54	15.91	3.30	0.55	0.55	14.61	0.15	97.60
	67.62	18.83	0.39	n.d.	0.17	12.16	n.d.	99.04
	62.54	15.49	2.65	0.40	0.50	14.30	n.d.	95.79
	63.77	17.83	0.67	0.00	1.07	14.69	0.12	98.15
	64.21	17.71	1.13	n.d.	0.97	14.78	0.39	99.15
12EM10	65.36	18.49	0.37	n.d.	0.69	15.04	0.15	100.08

APPENDIX C: EMBAGAI TITANOMAGNETITE MICROPROBE DATA

Sample	SiO_2	TiO_2	Al_2O_3	FeO	MnO	MgO	SUM
12EM02	0.06	10.73	3.52	75.58	0.93	5.53	96.34
	0.04	8.97	2.18	80.94	0.93	2.71	95.68
	0.03	10.47	2.02	80.64	0.88	2.88	96.83
	0.43	4.02	0.29	88.18	2.30	0.64	95.86
12EM06	0.08	14.31	0.38	81.34	1.49	1.04	98.69
	0.08	13.74	0.36	80.55	1.44	1.10	97.15
	0.10	13.89	0.39	80.49	1.55	1.08	97.49
	0.11	14.37	0.47	80.33	1.61	1.16	98.02
	0.02	13.91	0.33	80.61	1.40	1.07	97.36
	0.01	13.66	0.34	79.11	1.46	1.15	95.78
	0.07	14.03	0.31	80.39	1.51	1.03	97.31
	0.11	14.40	0.38	80.25	1.54	1.11	97.77
	0.07	13.17	0.39	79.93	1.44	1.09	96.02
12EM11	n.d.	10.82	2.84	77.48	0.79	3.94	95.90
	0.00	10.43	1.81	76.99	1.30	4.08	94.60
	0.54	2.05	0.22	90.24	1.02	0.15	94.20
	1.11	2.61	0.23	89.09	1.14	0.14	94.27
	0.75	7.18	0.40	81.00	1.25	0.08	90.64
	0.13	13.50	0.26	76.75	1.32	0.45	92.37
	0.79	4.51	0.33	84.91	0.06	0.24	90.84
	0.07	10.93	0.43	80.00	0.98	0.22	92.62
	0.08	11.80	0.73	78.68	1.96	1.39	94.67
	0.25	10.15	0.60	80.49	0.17	0.06	91.77
12EM15	0.08	9.12	3.23	80.38	0.63	3.56	97.03
	0.03	15.53	2.76	71.57	0.62	6.77	97.32
	0.11	15.23	2.75	71.58	0.43	6.76	96.91
	0.08	14.62	2.71	73.56	0.55	6.22	97.74
13T32	0.15	22.54	0.39	67.93	1.70	0.34	93.15
	0.13	24.00	0.08	66.39	2.05	0.13	92.87
	0.15	22.34	0.43	68.20	1.86	0.36	93.37
	0.14	22.59	0.22	67.15	1.58	0.22	91.95
	0.13	21.95	0.22	67.86	1.62	0.19	92.03
	0.16	22.87	0.13	67.39	1.73	0.18	92.46
	0.11	24.47	0.07	65.57	1.80	0.12	92.18
	0.14	21.33	0.75	67.91	1.56	0.47	92.25
	0.12	21.32	1.25	68.13	1.53	0.70	93.11
	0.14	21.91	0.74	67.57	1.57	0.45	92.41
	0.17	22.75	0.27	67.01	1.70	0.29	92.26
	0.13	21.93	0.31	67.69	1.59	0.29	92.04
	0.15	22.10	0.30	67.43	1.67	0.29	91.98
	0.05	22.33	0.12	67.99	1.60	0.15	92.38
	0.14	22.03	0.76	66.90	1.71	0.56	92.12

APPENDIX D: EMBAGAI NEPHELINE MICROPROBE DATA

Sample	SiO_2	Al_2O_3	FeO	CaO	Na_2O	K_2O	SUM
12EM03	40.87	31.23	2.45	0.19	15.45	7.35	97.66
	42.19	33.24	0.77	0.03	15.23	6.70	98.18
	45.05	31.62	1.43	0.10	15.50	5.46	99.26
	44.90	31.08	1.62	0.08	15.17	5.33	97.89
	44.25	31.64	1.41	0.10	14.97	5.81	98.21
	42.16	33.61	0.87	0.03	15.44	6.53	98.69
	42.95	33.08	0.98	0.03	15.42	6.34	98.88
	45.67	30.76	1.02	0.31	14.17	5.65	97.52
	42.21	33.33	1.14	0.02	14.88	6.28	97.94
	43.03	34.21	0.93	0.10	15.32	6.61	100.34
12EM04	41.42	32.35	2.15	0.16	13.67	8.58	98.21
	42.20	31.82	2.04	0.17	13.97	8.36	98.53
	42.42	29.27	4.58	0.08	14.69	8.26	99.49
	41.44	32.39	2.17	0.17	14.37	8.43	98.70
	41.34	32.14	2.11	0.18	14.39	8.48	98.72
	41.58	32.57	2.20	0.18	14.46	8.75	99.75
	41.59	32.02	2.60	0.16	13.90	8.57	98.84
	41.34	32.77	2.00	0.16	14.35	8.40	98.76
12EM06	44.12	31.08	2.80	0.23	16.17	5.12	99.19
	44.69	31.00	2.68	0.12	16.42	5.23	100.31
	43.12	33.20	1.31	0.16	15.97	5.90	99.83
	43.27	33.41	1.57	0.12	16.22	5.65	100.12
12EM09	42.93	33.13	1.61	0.06	15.16	4.91	97.78
	44.08	33.57	1.42	0.06	16.01	5.53	100.74
	44.29	33.58	1.16	0.29	16.29	4.78	100.35
	43.74	32.56	1.62	0.08	16.26	5.55	100.09
	44.67	32.39	1.34	-0.01	15.97	5.69	99.99
12EM11	42.79	33.13	1.85	0.21	16.08	5.92	99.88
	42.79	32.88	1.66	0.49	15.68	6.00	99.39
	43.39	32.42	1.62	0.37	16.26	5.79	99.73
	41.78	32.60	1.30	0.48	15.80	6.23	98.23
	43.13	33.38	1.53	0.37	16.08	5.81	100.36

Sample	SiO_2	Al_2O_3	FeO	CaO	Na_2O	K_2O	SUM
13T32	44.72	32.76	0.72	0.40	17.22	4.44	100.29
	45.84	31.92	0.79	0.09	17.34	4.08	100.16
	45.32	32.40	0.79	0.38	17.49	4.29	100.60
	45.37	32.64	0.73	0.04	17.22	4.25	100.58
	45.67	31.73	0.73	0.03	17.27	4.03	99.71
	45.66	33.18	0.71	0.04	17.33	4.34	101.21
	46.13	32.64	0.95	0.06	16.87	4.03	100.51
	45.52	32.91	0.86	0.05	17.38	4.17	101.06
	45.52	32.86	0.89	0.08	17.33	4.46	101.24
	45.33	32.48	0.90	0.00	17.66	4.21	100.68
	45.62	32.83	0.83	0.06	17.50	4.19	101.24
	45.26	32.88	0.84	0.18	17.45	4.26	100.75
	46.01	32.69	0.90	0.06	17.30	4.25	101.49
	45.62	33.27	0.92	0.03	16.67	4.44	100.69
	46.06	32.36	1.04	0.04	17.16	4.04	100.72

APPENDIX E: EMBAGAI ANDRADITE MICROPROBE DATA

Sample	SiO_2	TiO_2	Al_2O_3	FeO	MnO	MgO	CaO	Na_2O	SUM
12EM02	33.28	4.71	2.12	24.42	0.44	0.51	33.67	0.05	99.20
	31.92	9.69	1.58	23.83	0.44	0.62	33.02	0.18	101.27
	34.93	2.09	2.10	25.66	0.45	0.35	33.72	0.05	99.37
12EM04	28.14	19.27	0.13	18.68	0.40	0.91	31.04	1.03	99.67
	26.41	20.31	0.31	19.68	0.44	0.81	31.37	0.76	100.09
	26.72	19.38	0.18	19.13	0.42	0.81	31.14	0.88	98.71
12EM10	26.79	17.56	1.38	19.79	0.35	1.17	31.71	0.23	98.97
	33.16	5.85	1.69	25.55	0.28	0.44	32.77	0.10	99.83
	29.68	12.61	0.79	22.38	0.36	0.56	32.44	0.28	99.07
	32.68	5.65	0.52	26.54	0.68	0.22	32.03	0.38	98.70
12EM11	32.20	6.81	0.95	25.23	0.34	0.26	33.17	0.19	99.17
12EM15	30.67	10.00	0.47	24.34	0.31	0.69	32.65	0.27	99.39
	27.57	15.23	0.78	20.95	0.27	0.98	31.88	0.23	97.89
	26.48	18.14	0.73	20.95	0.32	1.13	31.91	0.32	99.98
	30.16	14.19	0.30	21.92	0.32	0.53	32.00	0.64	100.06

APPENDIX F: EMBAGAI SPHENE MICROPROBE DATA

Sample	SiO_2	TiO_2	Al_2O_3	FeO	MnO	MgO	CaO	Na_2O	SUM
12EM06	30.37	38.58	0.41	2.21	0.03	0.05	27.95	0.27	99.84
	29.76	38.52	0.63	1.40	0.06	0.07	28.30	0.15	98.88
	30.54	37.19	1.03	2.69	0.01	0.06	26.94	0.34	98.99
	30.21	37.86	0.36	2.25	0.05	0.11	26.80	0.87	98.55
12EM09	30.47	37.86	0.47	1.98	0.03	0.03	28.74	0.12	99.69
12EM10	30.38	36.25	0.23	2.34	0.05	n.d.	28.30	0.30	97.83
12EM11	30.05	39.59	0.54	1.55	0.05	0.00	28.96	0.07	100.78
13T32	30.12	37.41	1.04	1.28	0.11	0.02	26.88	0.11	96.96
	29.98	38.07	0.78	1.15	0.03	0.05	26.94	0.15	97.23

APPENDIX G: EMBAGAI PEROVSKITE MICROPROBE DATA

Sample	SiO_2	TiO_2	Al_2O_3	FeO	MnO	MgO	CaO	Na_2O	SUM
12EM03	0.01	58.12	0.25	0.99	0.01	0.00	39.01	0.54	98.94
	0.02	58.95	0.12	1.15	0.06	0.02	39.78	0.51	100.61
	0.06	58.37	0.09	1.06	0.04	n.d.	40.06	0.45	100.14
	0.01	58.26	0.18	1.13	0.07	0.04	39.42	0.39	99.51
	0.03	57.12	0.23	1.06	0.06	0.02	39.64	0.46	98.62
	0.06	57.94	0.28	1.25	0.02	0.05	39.41	0.52	99.55
12EM10	0.04	58.80	0.13	0.76	0.03	0.00	39.51	0.49	99.73
12EM15	0.06	58.57	0.14	0.78	n.d.	0.05	39.41	0.31	99.29
	0.04	58.99	0.17	0.92	n.d.	0.02	40.38	0.31	100.80

APPENDIX H: ORIENTATION MEASUREMENTS FOR PALEOMAGNETIC SAMPLES

Sample and core	Azimuth	Hade	Dip	Sun
10-T21-1	93	10	80	12
10-T21-2	49	8	82	55
10-T25-1	31	85	5	-
10-T25-2	36	86	4	-